Volume Conduction in Sensing for Physiological Measurements

Volume Conduction in Sensing for Physiological Measurements

A thesis submitted to the University of Kent at Canterbury

In the subject of Electronic Engineering

For the Degree of

Masters in Science by Research

By

Gabriele Scannicchio

September 2025

Table of Contents

Table of Contents.....III
Abstract.....V
Acknowledgements.....VI
CHAPTER 1 INTRODUCTION.....1
1.1 PROJECT STATEMENT.....1
1.2 RESEARCH QUESTIONS.....2
1.3 PROJECT AIMS AND DELIVERABLES.....3
1.4 THESIS OUTLINE.....4
CHAPTER 2 ELECTRONIC, MECHANICAL AND MEDICAL FUNDAMENTS OF SENSORS.....6
2.1 SHOULDER ANATOMY AND BIOMECHANICS.....7
2.1.1 Overview of Shoulder Arthroplasty.....8
2.1.2. Structure of a Ball and Socket Joint.....9
2.1.3. Shoulder Joint Biomechanics.....11
2.2 PRESSURE AND PROXIMITY SENSING.....14
2.2.1 Modelling Capacitive Sensors.....15
2.2.2 Capacitive Pressure Sensing.....16
2.2.3 Sensor Array Configuration.....20
SECTION 2.3 POWER AND DATA TRANSFER.....22
2.3.1 Introduction to Multiplexing.....23
2.3.2 Phase-Shifts and Link Characterisation.....26
2.3.3 Impedance Matching.....27
SECTION 2.4 CONCLUSION.....30
CHAPTER 3 METHODOLOGY.....31
3.1 3D MODELLING AND SIMULATIONS.....31
3.1.1 Array Parameters.....32
3.1.2 Tissue Properties.....35
3.1.3 Error Sources in Simulations.....36
3.1.4 Shoulder Model Preparation.....37
3.2 MANUFACTURING.....42
3.2.1 Initial Electrode Design.....42
3.2.2 Manufacturing Tests.....45

3.2.3 Testing Setup.....46
3.2.4 Test Object Manufacturing.....48
3.2.5 Testing Methodology.....54
3.3 CONCLUSION.....55
CHAPTER 4 SIMULATIONS OF THE ARRAY.....56
4.1 FLAT ARRAY SIMULATIONS.....56
4.1.1 Array Trial Run.....56
4.1.2 Complete Flat Array.....61
4.2 CURVED ARRAY SIMULATIONS.....64
4.2.1 Array Curving.....66
4.2.2 Final Curved Array Trial.....68
4.3 SEGMENTED ARRAY SIMULATIONS.....73
4.3.1 New Workflow.....73
4.3.2 Spherical Load.....74
4.3.4 Hemi-Torus Load.....78
4.4 CONCLUSION.....80
CHAPTER 5 EXPERIMENTS.....81
5.1 PROTOTYPE TESTING.....87
5.1.1 Observations on Printing.....89
5.2 FUTURE APPLICATIONS IN SYSTEMS.....90
5.3 CONCLUSION.....93
CHAPTER 6 GENERAL CONCLUSIONS.....94
6.2 FUTURE WORK.....95
REFERENCES.....97

Abstract

This project proposes an intrabody flexible capacitive pressure sensor array aimed at tracking the loosening of shoulder joint implants. To this end, the thesis develops an interdisciplinary approach, characterised in two phases: simulated tests, conducted through the CST Studio Suite software, and real-life tests, conducted through measurements of the capacitance change with an LCR meter at different pressures on specially prepared prototypes manufactured through both subtractive and additive methods.

The tests devotes special attention to the relationships, analogies and common points between the mechanical and electronic aspects of the design, aimed at understanding the phenomena underlying the sensor's transduction process and improving the sensitivity, with the eventual goal of integrating the new sensor model into existing communication systems to wirelessly receive power.

In conclusion, this thesis aims to develop the pressure-sensing array mentioned above and document the process in all its forms, including potential applications, the transduction mechanism employed, unique challenges posed by the human body environment and parameters of interest.

Acknowledgements

I would like to express my most sincere thanks to all the people who assisted me in the development of this project, beginning with my supervisors, Dr. Viktorija Makarovaite and Prof. John Batchelor for the invaluable guidance they provided throughout the course of the project in all its aspects. Further thanks go to Dr. Robert Horne for the development of the readout circuit PCB; Mr. Nathan Brabon for his supervision and guidance during the 3D printing of the sensor and circuit; Dr. Philippos Assimakopoulos for letting me attend his lectures on the implementation of logical functions and circuit manufacturing, which proved invaluable during the later stages of the project;

Other people I would like to thank are Mr. Antonio Mendoza for his assistance in the manufacturing of the earliest sensor prototypes; Mr. Alp Arslan, with whom I exchanged a great deal of technical assistance and advice that made the development of this project in its current form possible.

A heartfelt thank you goes to all the people who made my stay at the University of Kent a memorable experience since the very beginning, beginning with my friends: Kory Wingrove, Melanie-Kiera Longden, Tyler James, James Richardson, Elizabeth Foulstone, Dora Westwood-Flood, and Archer Peers. The last thanks are for my parents, Prof. Nicola Scannicchio and Dr. Angela Venezia. All these people have listened to me discuss my theories and research with them, all while continuously encouraging me during this time.

Chapter 1
Introduction

1.1 Project statement

In recent years, a large amount of research was conducted in the form of literature articles, prototypes, and experiments on the likenesses between receptors in human cells and modern sensing devices. This opened the door to the improvement of existing biomedical systems by adding the property of biomimetics: the ability to seamlessly integrate with the rest of the body, which is particularly desirable for systems meant to replace body parts (such as prosthetics). Moreover, with the recent development of micro- and nano-scale manufacturing techniques, made possible by 3D printing, the production of electronic circuits on flexible bases fabricated out of a variety of materials has become feasible. This allows for the development of small, minimally invasive sensors that, in the biomedical field, may deliver real-time health and point-of-care monitoring. These circuits have the potential to be highly biomimetic by their ability to easily apply onto the body (e.g.: on the skin), which can be further improved via studies into the material of the base and circuit tracks, the manufacturing methods and the signal processing systems.

The Internet of Things (IoT) has become an increasingly broad trend in recent years and brought about extensive literature exploring the possibility and potential techniques through which “smart” capabilities may be embedded in existing implant designs to improve upon them. This field of biomedical engineering considers the implant as a component in the traditional von Neumann architecture of Sensor-Processor-Actuator, something facilitated by the widespread understanding that the human body obeys much of the same principles.

A commonly proposed design across the literature is to embed biosensors within commonly used implants, such as the shoulder, knee, and hip. In particular, the shoulder is a compelling objective, as shoulder replacement surgery is the oldest clinical procedure in use; however, any system housed within the implant must contend with strict size, power, and mechanical requirements, which are difficult to meet with conventional solutions. A particularly appealing approach in the existing literature is to use a sensor array instead of single biosensors; these are networks of multiple small sensing units, arranged together in a pattern (a grid or an interdigitated pattern) that makes up a micro-structure. Pressure-sensing arrays such as the one currently in development are widespread within modern consumer electronics, spearheaded by the development of touch screen panels. Since then, many other applications appeared, such as underwater pressure sensing and biomimetic reception

embedded in prosthetics. In the present day, further developments introduced new technologies such as flexible circuitry and additive manufacturing, which serve to loosen constraints on the array geometry. A gap in the literature remains insofar as the use of arrays in intrabody implant communications is concerned, regarding the parameters of interest, array geometries, and testing methodologies.

One use of these sensors is to monitor the integrity of hip and shoulder implants; the latter are particularly prone to loosening, due to their lower stability as opposed to the former (which are load-bearing implants). Over time, the connection between the elements comprising the shoulder joint can come apart, causing discomfort to the patient. This process may accelerate due to conditions such as allergic reactions stemming from metal sensitivity. Therein lies the purpose of this project: to develop a flexible sensor easily embedded within existing shoulder implant models with the aim to track loosening.

1.2 Research questions

1.2.1 System development challenges

Compounding the challenges that hinder the development of implants, at both a clinical and developmental level, there is the problem of embedding electronics of any type within the human body. Because the human body is a lossy medium, conventional sensor designs may not be suitable, as are the design methodologies often followed. In such a situation, the key piece of information, the medium's electromagnetic properties, is difficult to define in the first place. Many such properties depend on external factors; chiefly the frequency of the signal transmitted across and the medium temperature.

All this takes place before accounting for properties specific to organic matter such as the human body. The rapid exchange of electrical signals that takes place between cells as part of the signalling process, or within the nervous system, creates powerful displacement currents that impair any attempts at transmitting an electrical signal across and within human tissue, including picking up a sensor's output.

What was previously said also affects the methodology. The research surrounding the electromagnetic properties of lossy media follows a mathematical model of dispersion that calculates the losses from the above-mentioned external factors. Such a model is difficult to determine for the human body, notwithstanding the many attempts made over the years. While computational electromagnetic simulations can help with some of these problems, challenges also exist there. Many lossy media are difficult to simulate, as the above-mentioned dependence on external factors necessitates a large

amount of small mesh cells clustered together. In a situation like this, not only will the result be very computationally heavy, but also prone to errors.

Considering the challenges mentioned up to this point, a quantitative analysis of the problem may only be feasible after the completion of a qualitative study that outlines the scope of the challenges and methods to follow. Such an analysis is the focus of this thesis, through a combination of simulations and real-life experiments, which will be described in the respective sections as necessary.

1.2.2 Defining the research questions

Considering the assessment in the previous section, it is necessary to set up the questions that this research will answer. The leading question to answer is to establish a method to design and test a sensor array for implantation within the human body to conduct physiological measurements, which will be carried out with both simulated and experimental tests. For the purposes of this research, the sensor ought to detect the pressure within the components of the shoulder joint. The objects of interest to this question are the mathematical quantities (e.g.: pressure, displacement, electrical capacitance) and physical factors (e.g.: array geometry, materials, equipment) that will contribute to the development of similar future sensors.

From here, further questions arise. For example, a wired connection to an intrabody implant is impossible to establish; a wireless connection is necessary to both power and acquire data from the implant. The basic components used and design principles followed when developing a wireless connection for a sensor array will be catalogued through a literature search, as well as previous examples of similar sensors. The questions lying behind the transduction process and data acquisition may be analysed through a combination of computer simulations and real-life testing to understand the factors that govern the operation of the sensors. The result of this analysis will pave the way for the development of a quantitative analysis into the performance of such sensors.

1.3 Project aims and deliverables

Several prototypes of flexible sensors have been developed over the years and documented in the literature; however, these were usually meant for larger-scale applications in soft robotics, for example in the development of upper limb prostheses. There remains a gap as far as intrabody applications are concerned, which this project aims to fill by fulfilling three objectives, as highlighted below:

1. Produce computer-generated models and simulations of a flexible capacitive pressure-sensing array.
2. Develop the simulated array in real-life by printing it on a dual-layered flexible PCB.

3. Document the design of the simulated and real-life arrays.

These also constitute the project's deliverables in the form of the simulation files, sensor array, array testing data, and the present report.

1.4 Thesis outline

The present thesis, titled "Volume Conduction in Sensing for Physiological Measurements" details the progression of the author's research surrounding the use of computer simulation software in the development of a flexible capacitive pressure-sensing array for intrabody applications within shoulder implants. The study has the aim of monitoring the implant's position and detect complications stemming from reverse total shoulder arthroplasty, which include, but are not limited to scapular notching, implant dislocations, and postoperative fractures.

The first chapter of the thesis introduces the nature of the gap in the literature that the project aims to fill and highlights the challenges from which such a gap stems, clearly outlined in the project statement. It also details the structure of the project and expected findings, embodied in the research question that the thesis aims to answer.

The second chapter presents a literature review which introduces the theoretical background underpinning all subsequent research. This chapter consists of three sections detailing the interactions between the principles of mechanics, orthopaedics and electronics involved in the project. The first section includes the mechanical modelling of the shoulder joint, calculation of the forces and torques involved in its motions, and the history of implants for arthroplasty up to the challenges faced in the present day. The second section covers the calculations of electrical capacitance and its changes in response to external factors, the transduction of the signals to be measured into electrical signals, and their processing. This section also introduces the challenges inherent to the study of the electronic properties of the human body. Lastly, the third section addresses issues such as the encoding of the signals produced by the sensors. Additionally, this section covers how to provide power to the sensors, and how to establish and maintain a data-carrying link that allows human beings to read the output.

The third chapter explains the methodology followed by the simulations, explaining the operating principles of electronic computer simulation software, and the parameters used as a reference to study the performance of the sensor array and as a source of information about its integration within the human body. It also covers the materials used during the modelling process, and their electronic properties. This chapter divides into three sections. The first tackles the workflow followed by the simulations, including existing criteria and constraints for the selection of the boundary conditions to apply and sources of errors during the same. The second section focuses on the implementation of the

simulation for real-life testing and the components employed by a proposed readout circuit; the third section describes the conditions in which the prototype was manufactured and tested, including manufacturing methods, testing iterations, the setup used to test the object, control parameters, and sources of error during calculations.

The fourth chapter describes the modelling and design of the simulations. These were conducted on multiple models of a flat, curved, and segmented sensor array. Here the procedure splits into multiple iterations, with a new iteration starting whenever the model went through significant changes. The numerical results for the parameters studied during the simulation, mathematical models created, and discussions thereof are also covered in this section.

The fifth chapter describes the testing of the real-life prototype, and its influence on subsequent simulations aimed at improving its performance. This chapter discusses the capacitive output of the sensors in air or within a printed shoulder articulation model. Two different sections describe the differences between the simulated and real-life test results, and the sources and replication of these differences, respectively.

Finally, the sixth chapter summarises the findings of this research project and provides insight into future applications of the studied technology. It also discusses any challenges that may arise or could not be overcome in conclusion of this work. This chapter also concludes with self-reflection on the current project.

Chapter 2
Electronic, Mechanical and Medical Fundaments of Sensors

When viewed in the anatomical position, using the right shoulder in the coronal plane as a reference, two components play a major role in shoulder movement biomechanics: the humeral head and the glenoid fossa. The former is lateral to the latter and inferior to the rotator cuff muscles, which stabilise the glenoid-humeral unit and allow the abduction of the shoulder. From a mechanical point of view, the humeral head and glenoid component form a ball-and-socket connection with three degrees of freedom (DoF). In this case, the humeral head is the ball component, which fits into a socket represented by the glenoid. The only reaction force is exerted by the glenoid onto the humeral head, allowing it a full range of motion in any other direction. Damage to any of these elements as a result of conditions such as cuff tear arthropathy (Shah & Gaal, 2020) (Shah & Gaal, 2021), is treated via shoulder arthroplasty.

Shoulder arthroplasty is a procedure wherein the joint is replaced, wholly or in part, with a mechanical prosthesis, with the purpose of treating conditions which compromise its integrity (e.g.: fracture, tuberculosis in the shoulder, humeral head necrosis). The prosthesis (hereafter referred to as the "implant") connects to the body via screws, which prevent it from moving (Willem, 2021). However, over time the screws can detach from within the bone, therefore leaving the implant free to move. This phenomenon, referred to as "implant loosening" (Shah & Gaal, 2020) (Shah & Gaal, 2021), is a common complication encountered in shoulder arthroplasties, and results in pain or discomfort to the patient.

Since the earliest shoulder arthroplasties, the mechanical properties of the implant were considered key to the success of the procedure. Even Jean-Emile Péan - the French surgeon responsible for the first documented shoulder arthroplasty - rejected the existing design for an ivory implant out of concern for its mechanical properties (Willem, 2021). Nowadays, studies concerning the mechanical properties of different implant designs are common in the literature.

A method of identifying the loosening is by measuring the distribution of pressure in the region between the glenoid and humeral head through a mechanical sensor. In a healthy individual, it is expected that the pressure distributes evenly between the two components; in the case of loosening, the implant's motions within the body will cause the humeral head component to lean towards one side of the glenoid.

2.1 Shoulder anatomy and biomechanics

2.1.1 Overview of shoulder arthroplasty

Shoulder arthroplasty is among the earliest common surgical procedures to be attempted, with the earliest recorded example dating back to 1893. The main innovations took place in the 1950s, starting with the Krueger implant's metal stem in 1950. Much more well-known, however, is the 'Neer I' implant, first seen the following year. The main change from the Krueger model was the use of chrome-cobalt for its material and an elongated stem that would prevent bone resorption. At this point, both sections of the implant consisted of bulk metal, and so would remain until the 1970s, when early examples of polyethylene-based glenoid components began circulating. The 'Neer II' model was based on this new finding, with the added component of modularity (Willem, 2021). Figure 2.1 shows the modular structure of modern implants, first introduced in the Neer II.

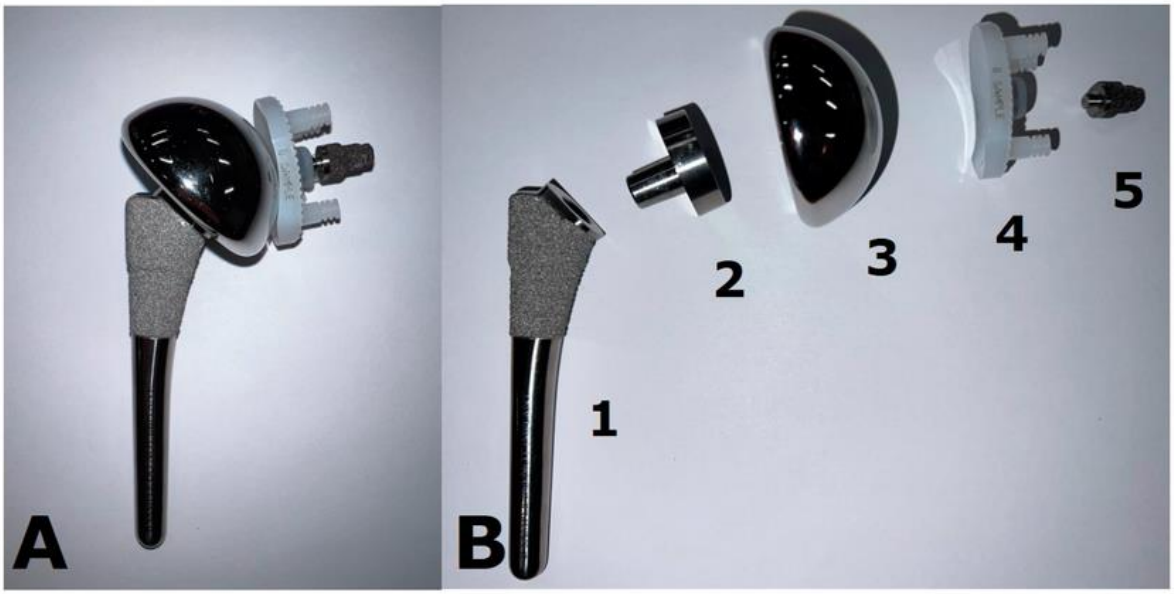


Figure 2.1. (a) Implant for anatomic total shoulder arthroplasty. (b) Components of implant for anatomic total shoulder arthroplasty. Taken from (Weaver, Omar, & Chadwick, 2023).

Around this time the concept of rTSA (Reverse Total Shoulder Arthroplasty) appeared; pre-existing surgical procedures took the name of aTSA (Anatomic Total Shoulder Arthroplasty). In aTSA (Figure 2.1) the structure of the shoulder remains the same as the joint, and the implant fits within the glenoid fossa in place of the humeral head (Sanchez-Sotelo, 2011). By contrast, rTSA sees the roles of the glenoid cup and humeral head in the joint as the socket and ball respectively reverse. A glenosphere fits within the glenoid cup and secured with screws forming a pin connection, while the humeral component ends in a hollow socket containing the glenosphere ball (Frank, Siegert, & Plachel, 2022) (Ponce, Oladeji, Rogers, & Menendez, 2015). Figure 2.2 shows the revised structure of a rTSA implant.

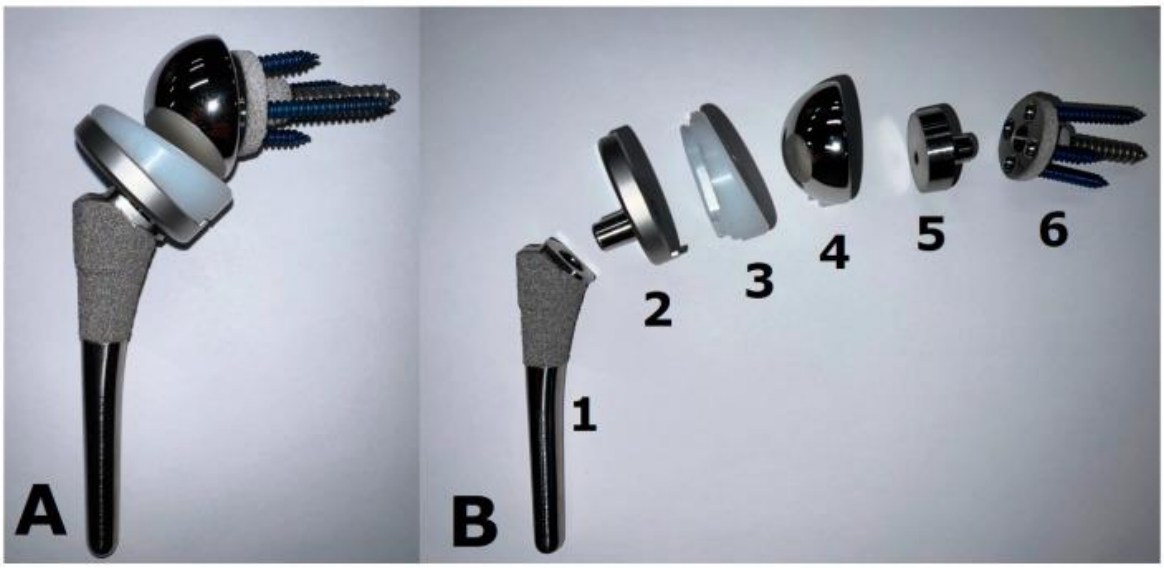


Figure 2.2. (a) Implant for reverse total shoulder arthroplasty. (b) Components of implant for reverse total shoulder arthroplasty. Taken from (Weaver, Omar, & Chadwick, 2023).

In 1985, Paul Grammont developed the first of the Delta series of implants, which introduced the two-thirds of a sphere combination used by most modern implants. This method introduced a median centre of rotation, lengthening the vector radius between the force of the deltoid muscles and the joint pivot on the glenosphere surface. A few years later, in 1991, the Grammont Delta III appeared on the market, and is still commonly studied within the literature to the present day. Its primary advantage is the large freedom of movement thanks to its Medial Glenoid / Medial Humerus configuration, which further lengthens the moment arm. Consequently, the total torque exerted by the deltoid increases while maintaining the force constant.

In the present day, computer simulation examines the mechanics of all different implant configurations through finite element analysis. This method was used to compare the Grammont design to other types of implants employing a Lateral Glenoid and Lateral Humerus configuration, arriving at the conclusion that a lateralised humerus has comparable performance with a slightly larger reaction force, implying a larger stability (Liou, Yang, & Sabesan, 2016).

The insertion of the humeral head within the glenoid only covers about 30% of the total surface of the humeral head; this is expected, as unlike the hip, the shoulder is not a load-bearing joint, and as such it does not need the stability to sustain the weight of the body. Over time, structural changes in the glenohumeral group can give way to a variety of conditions, stemming from either excessive contact between the two components (arthritis) or separation of the same (loosening). The current research focuses on the latter condition.

Loosening is usually the result of pre-existing condition; one such condition is scapular notching (Shah & Gaal, 2020) (Shah & Gaal, 2021). Scapular notching is a condition where the glenoid cup pin connectors cause damage to the bone via friction, resulting in an improperly secured implant (Barco & Savvidou, 2017). This damage creates a "hole" within the bone, leaving the implant capable of moving freely. Roche *et al.* utilised computer simulations to verify the causes and progression of scapular notching (Roche & Flurin, 2009) in search of methods to improve the range of motion without sacrificing the mechanical stability of the implant.

During the development of shoulder implants and preoperative examinations to determine the type of implant, a trade-off takes place between the range of motion and the stability, already mentioned in the introduction to Chapter 2. The desired result is achieved by controlling the distance and angle between the glenosphere pivot point and the humeral stem as the body exerting the force. Such a decision is particularly important in rTSA, where the roles of the humerus and glenoid are reversed. During this operation, the angle is of particular interest, especially in situations such as cuff tear arthropathy where a large component of the force is exerted by the deltoid muscles.

2.1.2 Structure of rTSA implants

Implants for rTSA can be further categorised according to their mobility, which is achieved by way of increasing the moment arm length within the joint (see Section 2.1.2). This can be accomplished with different types of implants in which the glenosphere is positioned in such a way to offset the line of action that the pivot, or Centre of Rotation (CoR) lies on and the line of action of the force responsible for the rotation, which coincides with the mid-section of the humerus (Roche C. P., 2022). Based on this parameter, the different configurations are as follows (Hamilton, Wright, Roche, & Flurin, 2015):

- Medial Glenoid / Lateral Humerus: The distance between the two lines of action is <2mm. The angle offset between the CoR and the humerus midsection is 132.5°.
- Medial Glenoid / Medial Humerus: The distance between the two lines of action is between 5.6 and 7.5mm. The angular offset is 155°.
- Lateral Glenoid / Medial Humerus: The distance between the two lines of action is between 8 and 10mm. The angular offset is 135°.

Because the line of action of the force exerted by the deltoid is not perpendicular to the force itself, the torque must account for the angle between the two. Using Equation (4), it becomes clear how a medialised CoR on the glenoid (i.e.: The Lateral Glenoid-based configurations) would result in a larger torque, which employs more potential energy as opposed to a medialised configuration. This larger torque is associated with an extended range of motion, but also a larger stress exerted on exerted on

the glenosphere itself, thereby compromising stability for freedom of movement. In a lateralised configuration, the opposite would be true, with a lower likelihood of loosening compared to a reduced range of motion.

The Grammont Delta III implant, which is a common implant used in surgical procedures, makes use of the Medial Glenoid / Medial Humerus configuration. To lateralise the humeral socket relative to the glenosphere and attain the Medial Glenoid / Lateral Humerus configuration, it is possible to change the thickness of the cup through an on-lay alignment ring. The alternative, if the glenoid must be medialised, is to install the alignment ring directly inside the glenosphere (in-lay) (Roche C. P., 2022).

2.1.3 Shoulder joint biomechanics

The entire shoulder joint can be viewed as a simple machine, specifically a lever where the rotator cuff muscles act as the fulcrum (the point of application of a reaction force that prevents motions), against which the deltoid applies an equal and opposite force (Pandya & Low, 2017). When the intensity of the deltoid force exceeds the reaction force exerted by the rotator cuff, the abduction of the shoulder takes place. Because the deltoid is distal to the rotator cuff, this configuration can be categorised as a third-order lever, where the distance of the fulcrum to the point of rotation is larger than the distance from the point of rotation to the force. Such an arrangement allows for a wider range of motions compared to other types of levers but expends more mechanical energy to produce smaller displacements (Figure 2.3).

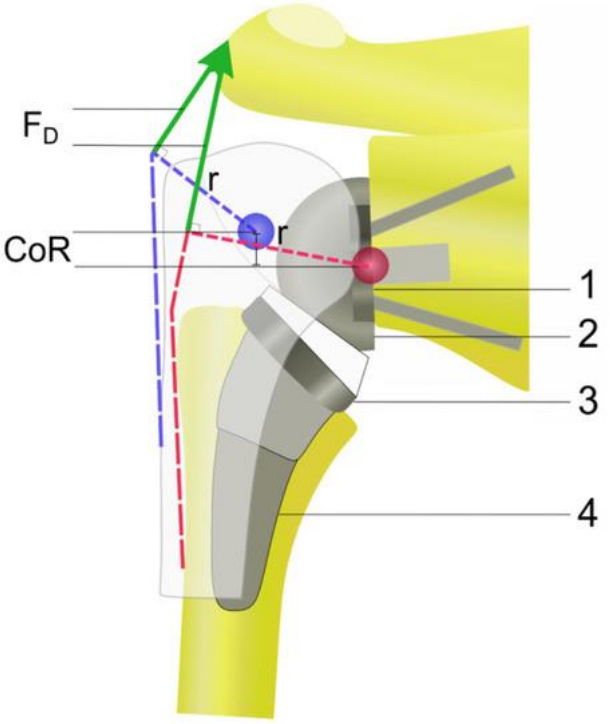


Figure 2.3. Forces involved in shoulder abduction with an rTSA implant. Taken from (Frank, Siegert, & Plachel, 2022)

An important measurement in this regard is the mechanical advantage (G) of the lever: the ratio of the mechanical energy released by the system to execute a movement and the energy introduced into it at a given point in time. It is known that the mechanical energy introduced into a system depends on the force acting on the same and the amplitude of the motion to be executed. The and-multiplication rule can be used to yield the following result:

$$E = \vec{F} \cdot \vec{x} \qquad (2\text{-}1)$$

where $\vec{F}$ is the force and $\vec{x}$ is the amplitude of the motion. The nature of $\vec{x}$ depends on the type of motion to be executed (e.g.: linear, rotational, etc.).It is also known that an infinitesimal variation of energy introduced into a system will produce an infinitesimal variation of the energy released by the same, which describes an infinitesimal gain. This can be formalised through the formula:

$$G = \frac{E_{out}}{E_{\text{in}}} \quad \therefore G = \frac{\overrightarrow{F_{out}} \cdot \vec{x}}{\overrightarrow{F_{\text{in}}} \cdot \vec{x}} \therefore G = \frac{\overrightarrow{F_{out}}}{\overrightarrow{F_{\text{in}}}} \qquad (2\text{-}2)$$

where G is the energy gain, E_{out} is the output energy, E_{in} is the input energy, $\overrightarrow{F_{out}}$ is the force that must be overcome and $\overrightarrow{F_{\text{in}}}$ is the external force applied. For a third-order lever, the following logical expression is true: $0 \leq G < 1$.

A consequence of equations (2-1) and (2-2) is that when the shoulder components are displaced, the deltoid muscle must provide a larger force to compensate. Therefore, the range of motion (RoM) of the upper arm (specifically during the abduction process) significantly decreases. A significant part of the implant design revolves around maximising the torque exerted by the deltoid while maintaining the reaction forces exerted by the humerus and glenoid constant (Liou, Yang, & Sabesan, 2016) (Moebs & Ling, Torque, 2016). Data usable as a reference originate from a variety of sources including literature articles, in vivo patient studies, and computer simulations. Consequently, to outline the scope of possible complications during SA responsible for implant loosening (which will inform the selection of sensing method and simulation methodology), it is important to analyse the procedure and principles through which the forces and torques involved in the motion are calculated.

The joint's CoR is located between the glenoid and humeral head and is used as a reference to calculate the torque produced by the deltoid when exerting a force (Roche C. P., 2022). The force's point of application can be set close to the humeral head, and the distance between the two becomes the moment arm. This setup can also simulate the internal displacement of an object secured to a frame via a connection of varying nature (Boileau & Watkinson, 2005). Roche et al. performed computer simulations in search of methods to extend the range of motion provided by implants for reverse shoulder arthroplasty without sacrificing implant integrity at the attachment point on the glenoid.

These simulations changed the angle between the humeral head and glenoid and calculated the resulting difference in amplitude and range of motions, producing a graph detailing a logarithmic relationship between the jump distance and humeral/glenoid angle. Under these principles, a longer distance between the glenoid cup and implant stem increases the torque exerted by the muscle, and by extension offers a wider range of movement.

This knowledge makes it possible to reframe the problem of implant loosening in mathematical terms. Many of the main conditions affecting the shoulder joint are a natural consequence of its biomechanics. A consequence of the relationship between the force exerted by the rotator cuff muscle and the displacement of the joint is that large forces are necessary to ensure a wide range of motions. As a result, the shoulder joint is unstable. The forces exerted on the glenoid cup and humeral head describe a mechanical stress, which can cause damage to the bone (especially in the case of prolonged exertion) or even joint dislocations. The area of the glenohumeral group at largest risk is the anterior glenoid, which is the part furthest from the CoR and thus most exposed to axial and torsional loads, which can be calculated through Equation (2-1) and Equation (2-3).

This is especially relevant when an implant is present, particularly in the case of rTSA implants: the screws used to hold the glenoid cup in place can “grind” the bone, progressively damaging it and displacing the implant – i.e.: scapular notching. Due to the new amount of free space, the implant will no longer be fixed in place, potentially causing pain in the patient. Knowledge of the position of the implant would provide an initial understanding of the extent of the notching or dislocation and inform subsequent clinical decisions.

As loosening tends to dislocate the stem with respect to the cup (by way of the angle between the two changing or the two separating from each other), the pressure distribution within the cup will change, which will be reflected in a different sensor reading. Where, in a stable implant, the pressure will be evenly distributed, a loosening implant will tilt towards either side, resulting in a series of areas acted on by a larger pressure compared to the rest of the region. For a dislocation of the stem, the overall pressure will decrease due to failure of the attachment.

2.2 Pressure and proximity sensing

To detect the progress and nature of the loosening, pressure and proximity sensors will be installed within the body, on the implant. The preferable locations are the top of the humeral stem, where the socket lays and the surface of the glenoid cup. While initial simulations employed the former configuration, it was later chosen to switch to the latter after seeing and comparing the results.

In addition to the size, another constraint to consider is the output of the sensor. Over the years, several literature articles have been published, conclusively establishing the human body as an attenuating medium where signals in the VLF range (Bevelacqua, 2021) are attenuated exponentially, in line with other forms of radiation (Lindsey, McKee, Hull, & Howell, 1998). This implies that any signal communicated across the body will suffer interference caused by the numerous electrochemical reactions occurring within; furthermore, that the skin is capacitive which will also affect the reading. Therefore, the sensor output will be highly prone to noise, which must be accounted for when designing a readout circuit.

As far as the sensor selection is concerned, different sensing modalities have been explored over the years for applications within the human body, such as piezoelectric, triboelectric, capacitive, and resistive. In particular, the piezoelectric and capacitive configurations have been experimented for applications in soft, flexible skin-like arrays, such as (Fares, Seminara, & Pinna, 2018) and (Wang, Zhong, Sun, & Li, 2014). Applications such as touch screen panels in smartphones after many years still use capacitive sensors; flexible applications of these are also seen outside the biomedical field, such as in underwater exploration vehicles (Hosseini & Chakraborty, 2022). Their well-known advantages

include robustness against environmental factors (e.g.: temperature, humidity), simple geometry which makes them easy to manufacture, and low power consumption. The main drawback is their lower sensitivity when compared to other sensor configurations, such as piezoelectric (Zhao & Ran, 2020). Furthermore, because their simple geometry is easier to model, using capacitive sensors is further advantageous during the simulation process. These advantages led to the choice of capacitive methods as the signal source when developing the sensor array. Low sensitivity is the primary challenge to overcome, and as such this would become the main object of research during simulations.

2.2.1 Modelling capacitive sensors

A capacitor is a medium capable of holding charge on its surface. This is most often accomplished by way of two conductive plates (electrodes) separated by an insulator (dielectric). The capacitive sensor array currently in development follows this structure, showed in Figure 2.4; the pressure and displacement range are also made explicit.

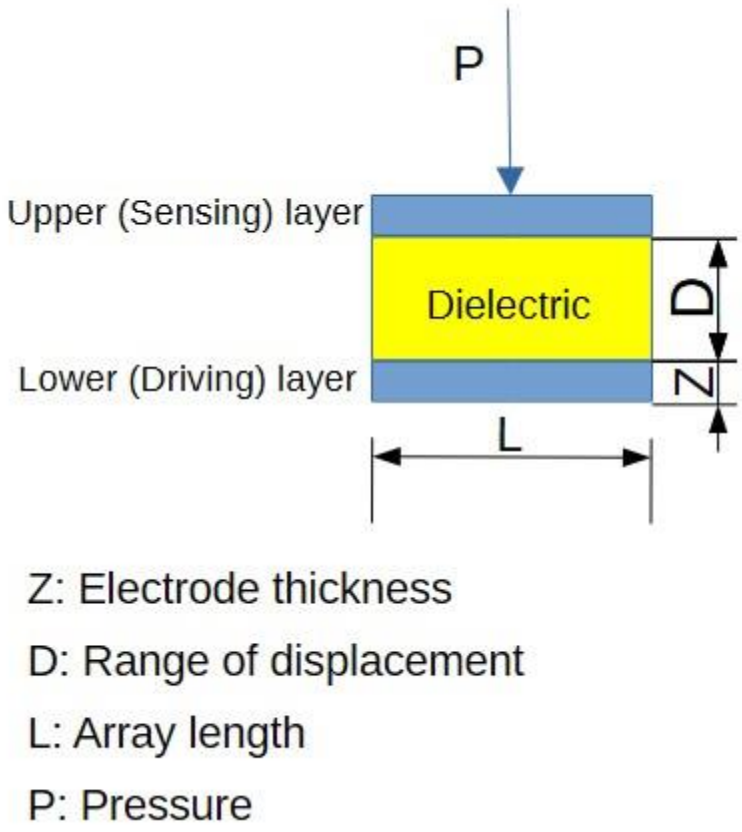


Figure 2.4. Side view of sensing unit, showing all relevant dimensions.

It is well-known that the leading influence on the capacitance at a constant point in time is the geometry of the plates, which affects the density of the electrical charge that moves across the capacitor. For the sensor design to be considered feasible, it must store the maximum possible

charge for the minimum possible plate and dielectric size. A major object of study in this research (through both simulated and experimental data) will be the capacitance of the sensors in relation to their size.

It is possible to establish a relationship between the capacitance and the geometry of the electrode through the following formula, which assumes the capacitance is constant over time:

$$C = \frac{\varepsilon_0 * \varepsilon_r * A}{d} \qquad (2\text{-}3)$$

where *C* is the capacitance, ε_0 is the permittivity (also known as the dielectric constant) of free space, ε_r is the relative permittivity of the medium, *A* is the surface of the plates and d is the thickness of the dielectric (Ling, Moebs, & Sanny, 2016).

Shifts in the property which is currently being measured (e.g.: temperature, molarity, spatial position) produce a change in the numerical value for one or more of the variables involved in equation (2-3), affecting the capacitance accordingly. This change in capacitance takes place over time and reflects a change in the electrical current transmitted across the capacitor.

The response that a capacitive sensor is expected to produce in reaction to a change in the measurand, is characterised in two sections: a rising segment where the capacitance increases logarithmically with the measurand (charge) and a decaying segment where the capacitance decreases exponentially (discharge). Further relations may apply, depending on the quantity to measure. It must be noted, however, that equation (2-10) is an approximation, as ε_r, one of the key parameters in the development of most capacitive sensors (Zhao & Ran, 2020) is not constant. Instead, it is dependent on the frequency of the voltage that moves the charge across the capacitor. For media such as the human body, where charge is constantly exchanged, a numerical value for permittivity must be determined experimentally, as many studies have done (Crile, Hosmer, & Rowland, 1921). Such studies must also account for environmental, genetic, and chemical factors, all of which may affect the electronic properties of different body parts, including the skin, and will pose a challenge to the integration of any sensor within the body (Bocan, Mickle, & Sejdić, 2017).

2.2.2 Capacitive pressure sensing

Touch screen panels are a good starting point for the design of a pressure array, as they are widespread, with extensive literature surrounding their design and performance (Nam, Seol, Lee, Cho, & Jung, 2021) (Park, Lim, & Jeong, 2014). Touch screen panels manufacturing processes engrave conductive wires into layers, perpendicularly to each other. The wires are separated by layers of dielectric material,

and the points where they cross over become standard parallel-plate capacitors. Figure 2.5 shows a top-down view of the structure.

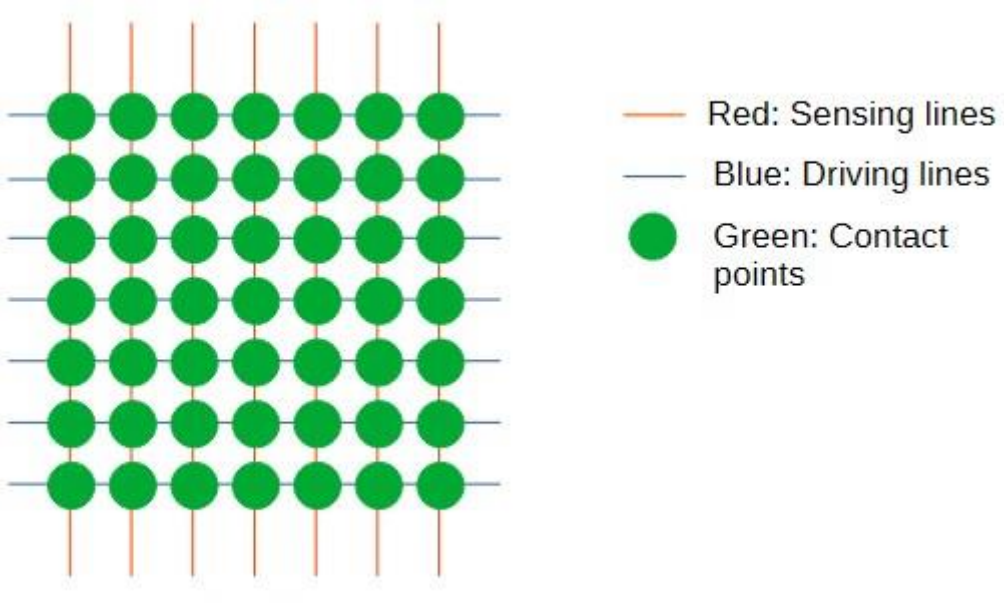


Figure 2.5. Top-down view of the sensor array.

When the single sensing units are acted on by a pressure, they will bend and rotate, producing a bending torque. As they bend, they will be subject to an infinitesimal elongation along the x- and y-axes, which have their origin in the centre of mass of the sensing unit. If the cross-section of the sensing unit approximates to a rectangle, the centre of mass will be within the dielectric's bulk. From this point on, the theory of pure bending may be applied to determine that the pressure required to produce a given deformation will be proportional to the rigidity, *E*, of the body currently bending, the elongation, *x*, and the bending radius, *R* (Syed & Elfadel, 2024).

$$\sigma = \frac{Ex}{R} \qquad (2\text{-}4)$$

In this case, the elongation, *x*, is proportional to the dielectric thickness *d*, which in turn connects to the capacitance change in the sensor by way of equation (2-3). The deformation is a function of space, specifically, of the x- and y-coordinates of the point acted on by the pressure. This means that the capacitance change in response to pressure depends on the space in which the force is exerted. For this reason, one must observe its behaviour localised to a section of infinitesimally small surface areas where it is reasonable to assume that the change is constant. To obtain the total surface area, the changes in each infinitesimally small surface add together via integration. If the above-described infinitesimally small area on the sensor surface is labelled as dA, then it is possible to construct an integral that calculates the bending within the sensor and calculates its capacitance output via

equation (2-3) (Wang, Zhong, Sun, & Li, A flexible capacitive tactile sensing array for pressure measurement, 2014).

$$C = \int_{A_1}^{A_2} \frac{\varepsilon_0 \varepsilon_r}{d\text{-}w}\, dA \therefore \iint_{x_1, y_1}^{x_2, y_2} \frac{\varepsilon_0 \varepsilon_r}{d\text{-}w} dxdy \qquad (2\text{-}5)$$

In this equation *d* is the initial distance between the plates; *w* is the deformation of the same; x_1 and x_2 are the extremes of the length of the plate along the x-axis; y_1 and y_2 are the extremes of the length of the plate along the y-axis; *dx* and *dy* represent the length of an infinitesimally small surface of area *dA*; ε_0 and ε_r maintain the same meaning as they do in equation (2-3).

For the purposes of this thesis, the pressure is going to be applied by loads whose mass is controlled externally, as opposed to similar studies where cyclical loading tests were performed through specialised equipment. This choice, however, creates the need to prove the existence of a relationship between pressure and mass. It is well-known that the pressure P can be written as follows:

$$P = \frac{\vec{F}}{S} \qquad (2\text{-}6)$$

where $\vec{F}$ is the force acting on the sensor, and *S* is the surface the force distributes across. The result of equation (2-6) is functionally equivalent to the stress term σ presented in equation (2-5). The force can be calculated through the gravitational expression of Newton's 2nd Law:

$$\vec{F} = m\vec{g} \qquad (2\text{-}7)$$

where *m* is the mass of the object; $\vec{g}$ is the gravitational constant always equal to 9.81 m/s^2.

The stress produces a deformation calculated through equations (2-11) and (2-12). Even when the body does not visibly bend, the same theory may be used to prove a connection between the deformation, the pressure applied and the elasticity of the body. The pressure necessary to produce a given deformation σ depends on the elasticity and the desired deformation; the 'and-multiplication' rule returns the following equation:

$$\sigma = Ex \qquad (2\text{-}8)$$

this is Hooke's Law, a generalised form of equation (2-4) usable for bodies that do not bend or where the bending is negligible. The elongation term, *x*, can be isolated, and if an equation system is created from equations (2-4), (2-7) and (2-8), then the formula simplifies down to:

$$x = \frac{mg}{ES} \qquad (2\text{-}9)$$

However, a numerical deformation alone does not give much information on the mechanical changes within the body acted on by a stress. For this reason, the numerical value of deformation is best expressed as a function of the change in length compared against the initial length. This is the strain constant ε:

$$\varepsilon = \frac{\Delta x}{L} \qquad (2\text{-}10)$$

where *L* is the initial dimension of the body; Δx is the change in length and can be used instead of the *x* term used in equation (2-9). After applying this reasoning, the deformation becomes a dimensionless constant that can be used in Hooke's Law as expressed in equation (2-8), to yield:

$$\sigma = E\varepsilon \qquad (2\text{-}11)$$

thereby recreating the equation system that produces equation (2-9):

$$\Delta x = \frac{mgL}{ES} \qquad (2\text{-}12)$$

which proves the existence of a relationship between mass, stress, and strain, as represented by a linear function with gradient equal to the elasticity of the object currently deforming. The numerator is given by the product of mass, gravity, and distance, equal to the mechanical work employed by the object exerting pressure (Moebs & Ling, Torque, 2016). Equation (2-12) therefore demonstrates that it is possible to measure the change in capacitance induced in a mechanical sensor through knowledge of the force.

This mechanical work is what pushes the plates of the dielectric together, thereby increasing the electrical capacitance of the sensor. It is, therefore, the quantity transduced into electrical signals readable by a processor (Peng, Xianmin, & Yulong, 2021) (Moebs, Ling, & Sanny, 12.6: Elasticity and Plasticity, 2016). When the plates are close to each other, the maximum mechanical work is employed and the capacitor charges; when the plates separate, the opposite happens and the capacitor discharges.

When comparing the capacitance against the pressure, it is expected that the two exist in a logarithmic relationship. This implies that the sensor is absorbing mechanical energy as its input and releasing electrical energy as its output. By contrast, if the pressure is measured in relation to the corresponding

plate displacement, then the latter's relationship with the capacitance will change exponentially (Sara Rachel Arussy Ruth, 2020).

2.2.3 Sensor array configuration

When multiple sensors connect to each other in series or in parallel, these define a sensor array. The operating principles of the individual sensors (sensing units) remain the same as the ones described in section 2.2.2. The main challenge in the design of an array is to reduce the size of the sensing units while preserving their accuracy.

An array is divided in rows and columns of wires on multiple layers, with sensors lying at the points where the rows and columns overlap with each other (Street & Sustich, 2014) – the same design shown in Figure 2.5.

The wires can be made of different materials, which have an influence on their properties such as permittivity, resistivity, or permeability. In capacitive sensors, indium-tin oxide (ITO) is the material of choice, with recent studies investigating the use of carbon nanotubes (CNT) (Cohen, Mitra, Peterson, & Maharbiz, 2012); these are printed on the flexible substrate, which is made of elastic polymers (elastomers) such as the polyamide (PA)-based Mylar or the PBAT-based EcoFlex (Naira, Shakhtivel, & Dahiya, 2023) (Chen, et al., 2018). The contact points between wires become akin to the plates, while the substrate acts as the dielectric. This structure can be manufactured through either additive or subtractive methods.

Through this method, it is possible to obtain information about both the space- and time-dependent properties of a physical phenomenon. Moreover, it is also possible to choose whether to process each output separately, group multiple array elements together, or process the output of all elements at once. Each of these processing methods has different implications for the overall accuracy of the sensor, and the choice between them depends on the desired accuracy limit and the time allocated for processing (Dahiya & Soni, Soft eSkin: distributed touch sensing with harmonized energy and computing, 2019).

The array configuration sees wide use for medical applications. It is highly biomimetic, as the receptors embedded within human skin work in much the same way as the sensing units within an array. Furthermore, by changing the length of the wires to produce new sensors at the intersections, or alternatively by stacking multiple layers of conducting wires on top of each other, it is very easy to scale the design up and down to fit the required application. Several articles even demonstrate the possibility of integrating sensors for multiple quantities (most frequently temperature and pressure) in electronic skin (eSkin) (Dahiya, Ozioko, & Kumaresan, Multifunctional Electronic Skin With a Stack

of Temperature and Pressure Sensor Arrays, 2021) (Fares, Seminara, & Pinna, 2018). Further applications are also an object of study, such as strain sensing in the detection of human presence or body weight monitoring.

Beyond the biomedical field, one of the most notable applications of array technology is in the touch screen panels of smartphones, which has served as a launch point for the current research. It is possible to compare the structure of a touch screen panel, such as the one designed by Hwang, Cui *et al.* in (Hwang, Cui, Yang, & Kwon, 2010) (Figure 2.6) to the structure of a medical-grade pressure array designed by Wang, Zhong *et al.* in (Wang, Zhong, Sun, & Li, A flexible capacitive tactile sensing array for pressure measurement, 2014) (Figure 2.7).

A medical-grade sensor (Figure 2.7) uses multiplexers across the driving and sensing layers to distinguish between the inputs and outputs across different rows or columns. The driving multiplexer maintains excited the respective electrodes, providing a reference voltage from which the capacitance at rest can be calculated. In mobile touch screen panels, a separate unit mounted within the device (the phone battery) provides power; by contrast, medical devices must make use of alternative solutions such as wireless power transfer (WPT), owing to the necessity to operate within tissue, where wires struggle to travel and may pose risks to the patient.

As in all sensors, interference (noise) affecting the readings is still a concern. A source of noise that is unique to the array configuration is sensor crosstalk, which occurs when changes in the properties of a single sensing unit affect other sensors in its proximity due to their existence in the electrical field that the other creates. However, a strong crosstalk also implies that the capacitance exchanged between sensing units is greater than it would be if each were isolated, necessitating a second trade-off between signal strength and spatial accuracy. This question is known as the density of the array – the concentration of sensing units within a constant space.

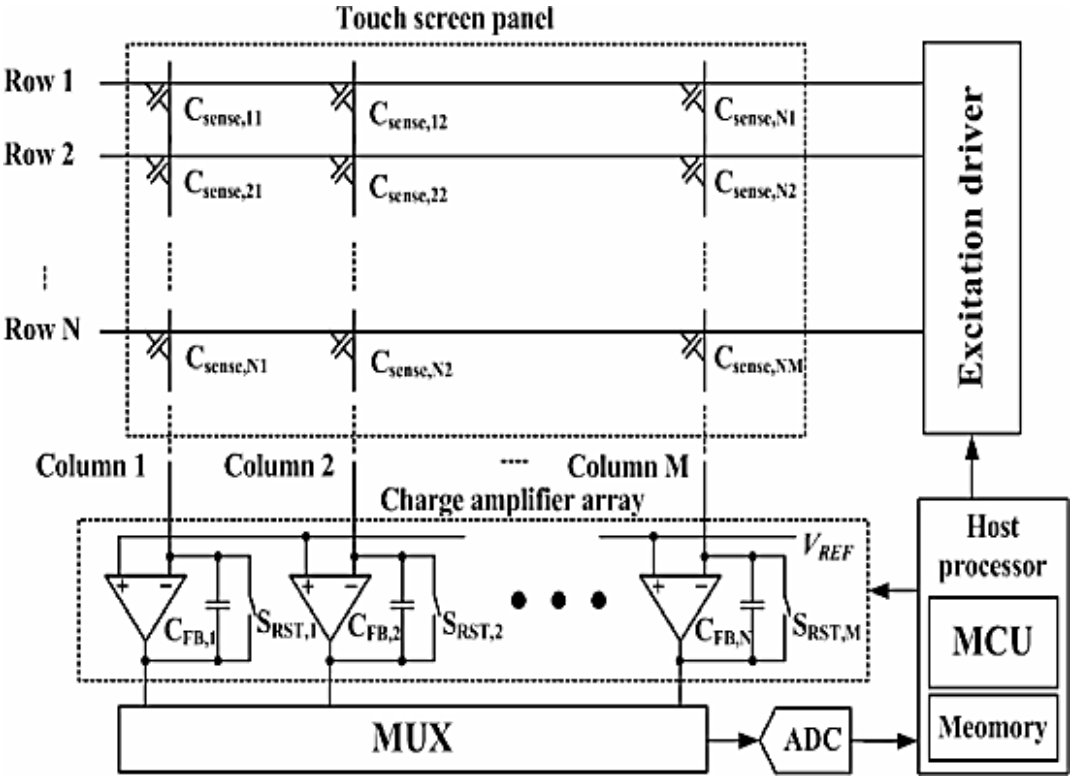


Figure 2.6. Block diagram for the touch screen panel of a smartphone. Retrieved from (Hwang, Cui, Yang, & Kwon, 2010).

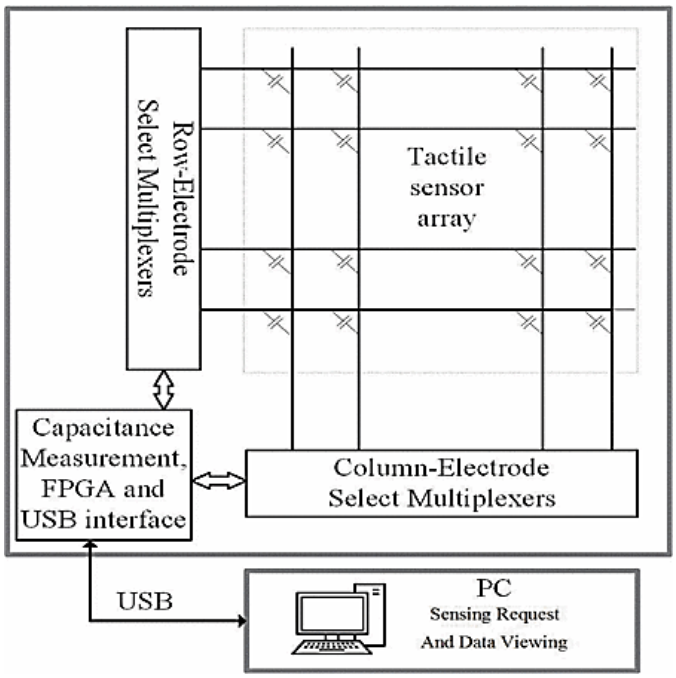


Figure 2.7. Block diagram for a flexible medical-grade array. Retrieved from (Wang, Zhong, Sun, & Li, A flexible capacitive tactile sensing array for pressure measurement, 2014).

2.3 Power and data transfer

Due to the implant being mounted beneath the skin for a shoulder application, a WPT-based link must be established, as a wired connection is widely considered unsuitable for intrabody applications

(Sadeque, Pavuluri, Cummins, & Desmulliez, 2020). Some devices, such as cardiac pacemakers, use built-in power sources. However, these carry the risks of leakage currents from the source and limit the implant's lifetime. Key to establishing a successful WPT link is the understanding that the human body is a highly attenuating medium, and significant electronic interference will be present. It is known that skin and muscles have a capacitive nature, and the possibility of using these as a method to transmit a signal has been the object of study (Jegadeesan, Agarwal, Guo, Yen, & Thakor, 2016).

As stated in section 2.2.1., the tissue permittivity cannot be calculated and must be obtained experimentally. This is a major challenge to the development of intrabody implant communications, and over the years, many models were proposed, shown in (Bocan, Mickle, & Sejdić, 2017). Recent literature dealing with the topic often uses the Cole-Cole model, which was introduced by Gabriel *et al.* in (Gabriel, Gabriel, & Corthout, 1996) (Gabriel, Gabriel, & Lau, 1996) (Gabriel, Gabriel, & Lau, 1996). Such a model serves as a base statistical model to which empirical data obtained from measurements can be fit. This model is used by several online tools that calculate permittivity in relation to frequency, such as the one used by this report as a source of relevant data (Bryn, n.d.).

One avenue, proposed by several articles, is the use of RFID technology as the means to establish the WPT link. The development of commercial implants employing the principles of intrabody implant communications produced the allocation of several radio frequencies, such as the MedRadio band. In (Merli, 2011), the principles that govern antennas for intrabody implant communications and the corresponding parameters of interest are studied.

A recent trend is the use of passive RFID techniques, directly powered by a signal provided by the interrogator, removing the necessity of much of the supporting circuitry that their active counterparts need. Applications in the development of orthotics and biomimetic prostheses studied extensively such developments to enable real-time monitoring of the patient. Many of the studies conducted in this regard use NFC technology in the HF band (13.56 MHz), as reviewed in (Shadid & Noghanian, 2018). In contrast, other studies propose the UHF band in the 860-960 MHz range, such as (Lodato & Marrocco, 2015). The trade-off to make concerns range and response time against specific absorption rate (SAR): higher frequencies are easier for the skin to absorb, with the potential of damage to the tissue. In this context, the HF band carries less risk to the patient, at the cost of limiting the readout range and response time. UHF devices carry a greater risk to the patient, but have a much longer range, with the potential to enable real-time monitoring even outside a clinical setting.

To achieve the functionalities outlined in section 2.2.3, medical-grade arrays require separate multiplexers with varying amounts of channel to encode the signal into a format readable by a control unit, such as a microcontroller (Dahiya, Ozioko, & Kumaresan, 2021).

2.4 Conclusion

The geometry of the sensor itself heavily influences the effectiveness of capacitive sensors. To account for the size constraints introduced by intrabody implant communication, it is possible to connect multiple such sensors together in an array structure, which can be used to produce information regarding both the location of the applied pressure and the time-dependent characteristics of the same. Array structures have become a topic of particular interest during the past decade, thanks to advances in both additive and subtractive manufacturing technologies capable of producing micro-scale structures.

The small size of these structures means that the key element in the capacitance-focused transduction process shifts from the size of the components (electrodes, dielectric) to their material, which affects the sensitivity and resolution of the array. Accomplishing this goal requires an understanding of the nature of the transduction process and the interactions between the electrical and mechanical phenomena underlying such a process. The study of these phenomena proved pivotal during testing to understand potential sources of errors to account for during experimentation, which would be considered negligible for larger-scale systems.

Due to their ease of use and well-understood principles, capacitive sensors received widespread diffusion in systems meant for intrabody applications such as shoulder joint pressure measurement. The literature published in these fields provided a useful basis to establish the methodology followed during development by way of mathematical models, parameters of interest and procedures needed during the readout of the sensor output.

Chapter 3
Methodology

To detect the progress and nature of the loosening, pressure and proximity sensors will be installed within the body, on the implant. The preferable locations are the top of the humeral stem, where the socket is, and the surface of the glenoid cup. The logistical complications of the in-vivo testing needed in these systems led to the use of simulations as a stand-in, later complemented by real-life experiments on a 3D printed shoulder joint. This allows the project to be divided into two phases, one encompassing the simulations and the other the empirical tests. This section describes the method followed in both the simulations and empirical tests and any changes it was subjected to during development.

3.1 Modelling and simulations

The simulation software CST Studio Suite was utilized during initial testing. The tests employed the Low-Frequency Sensing library pre-installed into the software with the Capacitive Sensors result template. This software also allows for the encoding and compression of 3D models used in simulations into Gerber (.GBR) files, which most PCB printing software and corresponding equipment accept. The design guide in (Corey, 2023) served as a reference for the control parameters.

As explained in section 2.2.2, simulating the effects of cyclical loading on a body required the change in capacitance to be measured with respect to the internal displacements of the sensing units, with a graphical proof through the diagram shown in Figure 2.6. This was accomplished by declaring the z-axis coordinates of each sensing unit's faces as control variables. During initial testing, the z-axis coordinate of each face was stored in memory as a separate variable. The software's 'Parameter Sweep' tool was employed to alter these coordinates, simulating a displacement that had a step width of 0.1mm. The initial value of the dielectric thickness δ was 0.5mm; from this point on, the range of displacements for the sensing unit will be referred to as $D_S \in [0.1\,;0.5]$ mm. The actual dielectric thickness after accounting for the displacement is equal to the difference between δ and D_S.

The number of computations to be performed, referred to as *N*, can be obtained through the 'and-multiplication' rule, and it is equal to:

$$N = \prod_{n=1}^{n} N_n^2 \qquad (3\text{-}1)$$

where N is the n-th variable involved in the parameter sweep, equal to the n-th element of the set D_S described above. For the first few runs, N was equal to 25. During later simulation runs, the variables

for the z-axis coordinates of each face were constrained together, thereby making N equal to 5. Because the Low Frequency and Statics CST suite allows the application of arbitrary voltages (as opposed to the RF Microwave suite), a standard 5V reference voltage was employed, characterised as a +2.5V input and a -2.5V output. Testing was performed with other voltage values, such as $\pm 0.5V$, $\pm\ 1V$ and $\pm 1.5V$; however, the 5V reference voltage showed the highest change in capacitance.

Testing started by displacing a single unit on the sensing layer and polarising it along with the units located along the same sensing line. The corresponding unit on the driving line underwent a similar operation. Other simulations changed this method, first by only polarising the sensing units currently being displaced and later by polarising the entire array and keeping the sensing units' displacement as the only control parameter.

The change in capacitance is the primary object of the measurements; it is expected for it to decrease exponentially as the dielectric thickness increased (in line with the fundamental principles of capacitors). This would represent the inverse to the function governing the relationship between the amount of mechanical energy employed in the applied pressure and the corresponding change in capacitance, described in section 2.2.2 (Dahiya, Ozioko, & Kumaresan, 2021). A flexible circuit is used as the base for the sensor, designed and simulated as a flat dielectric. Subsequent tests performed on a curved dielectric measure the effects of the curvature on the capacitance. The final batch of tests uses a flat dielectric once again, this time divided into multiple sections.

3.1.1 Array parameters

The sensor array was characterised as a matrix of 7x7 rows and columns, shown in Figure 3.1; the columns represent the sensing lines on the top layer, and the rows represent the driving lines on the bottom layer, in line with the standard principles of a conventional touch-screen panel. The final version of the array added one more row and column to improve the accuracy, turning it into an 8x8 matrix shown in Figure 3.2, totalling 64 sensing units.

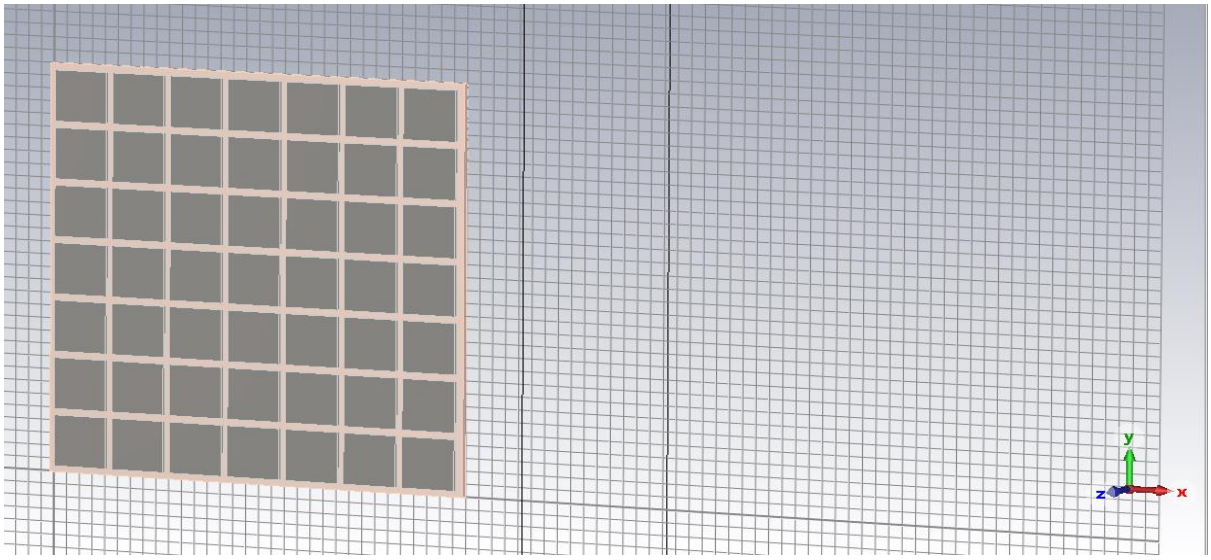


Figure 3.1. 3D model of the initial 7x7 array.

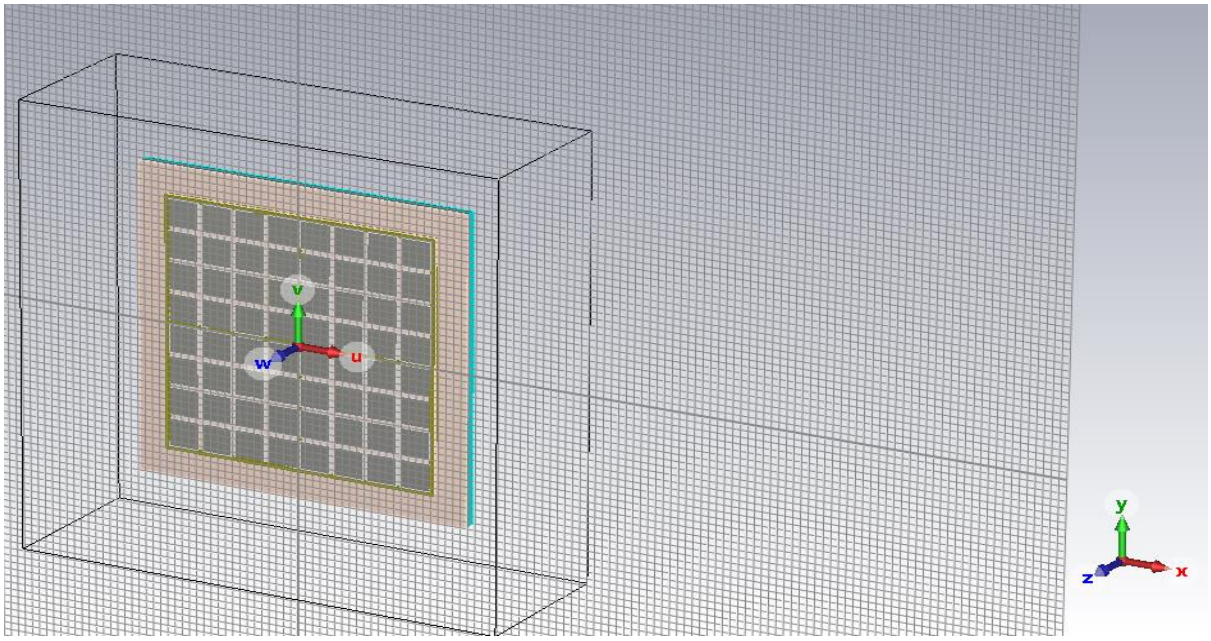


Figure 3.2. 3D model of the final 8x8 array.

Each individual sensing unit was considered as a perfect electrical conductor (PEC) with a size of 5x5x0.5mm, later reduced to 4x4x0.2mm. These made use of standard rectangular plates, as opposed to the wire configuration common in the literature; a visual comparison is in Figure 3.3. This choice simplifies the simulations, as it allows each individual sensing unit to be treated independently when setting the control variables. An advantage of this choice is that the initial capacitance is greater than it would be for a wire-based configuration, as the surface area of the plates influences the capacitance as per equation (2-11).

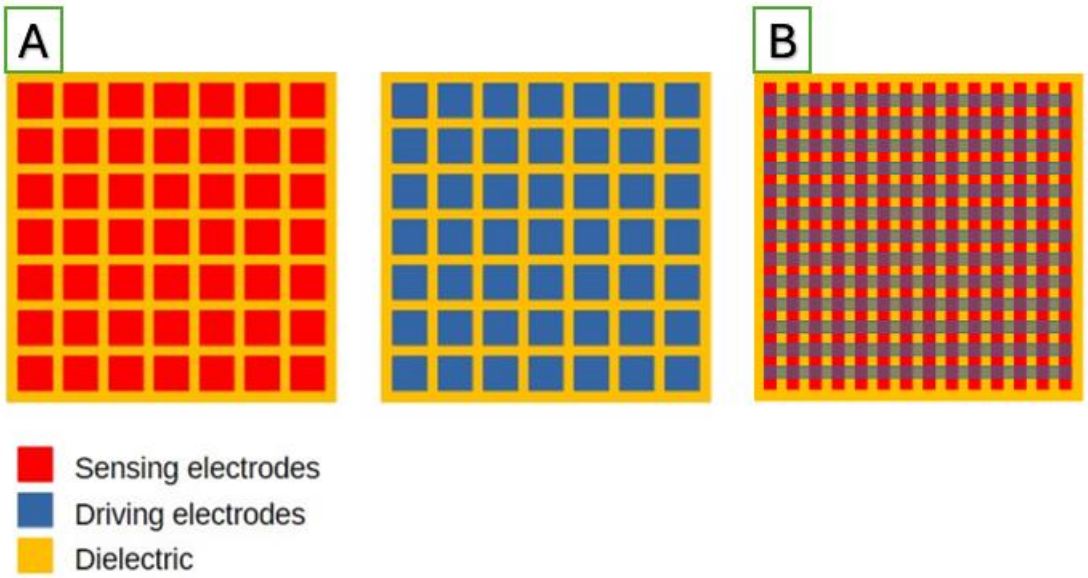


Figure 3.3. (A) Sensing unit shape for the array in development. The sensing and driving layers are shown separately to highlight the difference. (B) Shape of the sensing units in the configuration commonly used in the literature. The driving lines are made transparent to show the different layers.

For the purposes of the simulation, the sensing units are labelled by row and column in a standard rectangular coordinate system; the bottom-left sensing unit is set to have coordinates (0; 0), with all subsequent units following this convention. Within this system, the top face of the electrodes on the sensing lines were named as zElectrodeXY (where XY stands for the coordinates of the electrode along the respective axis); the bottom face appears as zLoadXY. The two variables are treated independently or in function of each other as the simulation requires.

In the final design, the array divides into four quadrants, each containing 4 rows and 4 columns, totalling 16 sensing units each. A 0.5mm-thick separator made of epoxy resin isolates the quadrants from each other; inside the single quadrants, however, the space between the sensing units remains free. At the centre of the separator, a second coordinate system is set as a reference, with each quadrant occupying the corresponding position on a rectangular plane. This was accomplished using CST's Local Working Coordinate System function, which allows to create multiple coordinate systems offset of each other in different points. The entire structure rests on a 50x50x0.5mm silicon base, mounted on top of a body phantom of dimensions 50x50x5mm.

The capacitance change acts as the reference to calculate the sensitivity of this configuration. A standard normalisation formula (Naira, Shakhtivel, & Dahiya, 2023), is used:

$$S=\frac{\Delta C}{C_0 * \Delta z} \qquad (3\text{-}2)$$

where ΔC is the capacitance variation in response to a change in the measurand, C_0 is the initial capacitance under stable conditions (no pressure applied), and Δz is the change in the displacement along the z-axis that produces ΔC. In this case, because the measurand is the displacement simulated through a parameter sweep, it is equal to the difference between the sensing unit's starting position on the z-axis and its location when displaced by an external force.

Three sets of arrays are considered:

- A uniform flat array without segmentation,
- A curved variant of the same as above,
- A flat array divided into segmented areas.

The flat array is the base for manufacturing, after integrating all features progressively implemented across multiple iterations of testing. All tests use a sample frequency of 0.5 Hz (Naira, Shakhtivel, & Dahiya, 2023), which covers the results described in this thesis. Further tests were conducted at different frequencies, with any changes highlighted as they appear. The registered parameters are the capacitance at each step of the displacement D_S, and the change in capacitance with each step measured as a function of the initial capacitance value: the sensitivity S. Later simulations also encompass the sensitivity expressed as a percentage of the capacitance to provide a comparison with values found in the literature.

3.1.2 Tissue properties

Replicating of the electrical behaviour of tissue is of particular interest during tests. It is known from prior experience that cells can be modelled a capacitive structure, with conductive fluids (extracellular fluid ECF and intracellular fluid ICF) separated by the cell membrane, which is an insulator. Consequently, the key to successfully modelling the electrical properties of the human body is to obtain an accurate value of its permittivity.

Following the Cole-Cole model, the permittivity value is calculated as a function of frequency (Gabriel, Gabriel, & Lau, 1996). One of these tools (Bryn, n.d.), was the reference to prepare the simulations. The database used during research, however, does not contain any value for the chosen frequency range. As such, during the experiments, the value was scaled down accordingly by using the change in permittivity between 10 and 20 Hz as a reference. After considering the permittivity values for skin and muscle, an arithmetic mean was calculated from these values and used as an average to produce the final model.

3.1.3 Shoulder model preparation

To ensure that the sensor would be functional, it was tested within a shoulder model. However, the development of a 3D printed shoulder joint phantom using exported .STL files based on images of the body - whose region of interest included the shoulder (produced through the medical imaging software 3D Slicer, (3D Slicer, n.d.)) - was retained and researched.

The sample data within 3D Slicer include a CT scan of the heart, wherein the Region of Interest (RoI) contains both arms and the shoulder (Figure 3.5). The RoI shows the anterior view of the thorax and both arms from the point of view of an external observer lying on the coronal plane. The right arm is the base for the model.

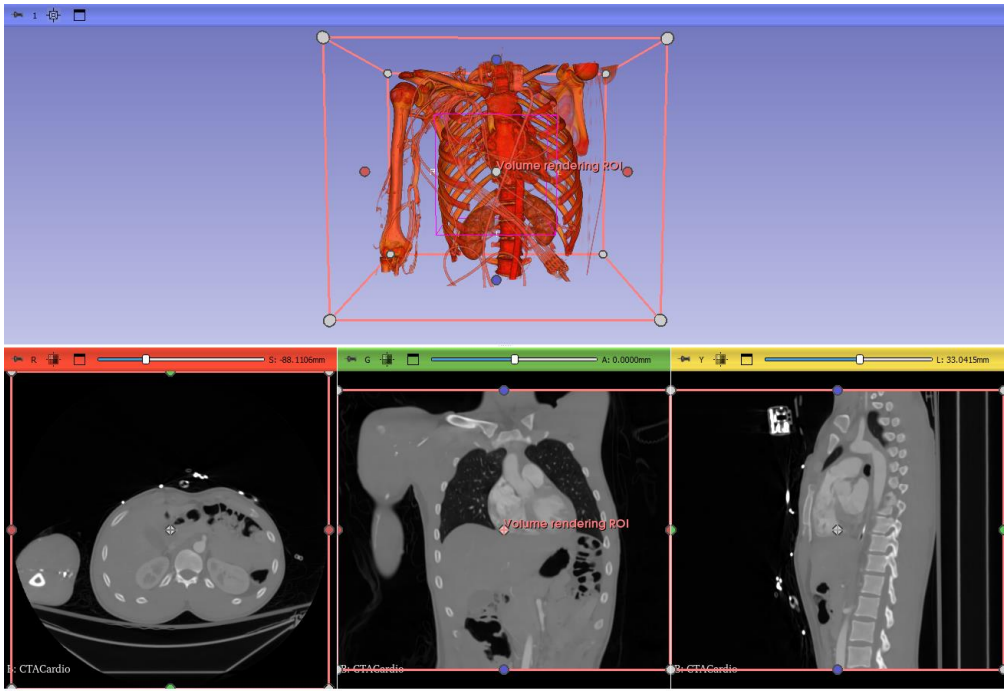


Figure 3.5. Region of interest containing the shoulder in 3D Slicer viewed by an external observer lying in the coronal plane.

The initial image in Figure 3.5 was cleared of all components not part of the shoulder joint; Figure 3.6 shows the result of the segmentation. The result appears in its original size (Figure 3.7A), in the form of CT scan outputs in the coronal, sagittal and transversal plane (Figure 3.7B), and from an up-close view (Figure 3.7C). After that, further cleaning up of the model was carried out by manually removing all unwanted points. This is easiest to accomplish with the 'Segmentation' tool built into the software. Here it is possible to choose a template for the part currently undergoing analysis (in this case, the bone), which will automatically assign colour values to the pixels within the image. The template makes use of an image thresholding algorithm, wherein the pixel values are categorised as belonging to a different body part, based on the grayscale values of the individual pixels stored in the system's memory of the original CT scan. The Segmentation toolset allows for editing of the CT image

layer by layer as well as the reconstructed 3D model, either manually through a brush tool or automatically through level tracing, which makes use of a watershed segmentation algorithm to distinguish regions whose pixel values are close to each other and fill them out as necessary. The toolset's 3D model view showed that the pixels were distributed unevenly, describing salt-and-pepper noise. This noise appears visually in the form of lulls and jagged edges on the 3D model. The close-up picture in Figure 3.7 shows one example of errors stemming from this noise through a close-up of the humeral head, which is not perfectly smooth and instead shows indentations and spikes, as does the nearby section of the glenoid fossa. To further alleviate the problem, Slicer also contains a smoothening functionality based on a Laplacian smoothing algorithm.

In the Laplacian algorithm, the different faces of an image show as surfaces and the points representing noise differentiate from the rest of the image features by way of a weighing factor (smoothening factor). Under the idea that noise appears where the image feature edges surround small surface areas that appear within a short distance of each other, an edge detection algorithm identifies and filters out the noise. The smoothening factor is used to calculate the Laplacian of the field that exists in the region where the image is defined, which mathematically models the change in pixel colour levels (in the case of a colour image, the grayscale levels are replaced by the image's RGB-scale levels) relative to the pixel's distance from the edge. The edges are subsequently distinguished by identifying areas where the pixel colour levels change by a large amount in a short period of time (Pinter, Lasso, & Fichtinger, 2019).

However, as the filter removes larger areas of the image manifesting noise, the image features will undergo the risk of disappearing, distorting the image. A trade-off is therefore required between image accuracy and noise filtering. The software applies automatically this process when dealing with the humeral head (Figure 3.6) and the processed image (Figure 3.7). For the purposes of this research, a scaling factor of 0.5 is chosen as a satisfactory compromise between the removal of noise and the preservation of the initial shape. The result appears in Figure 3.9.

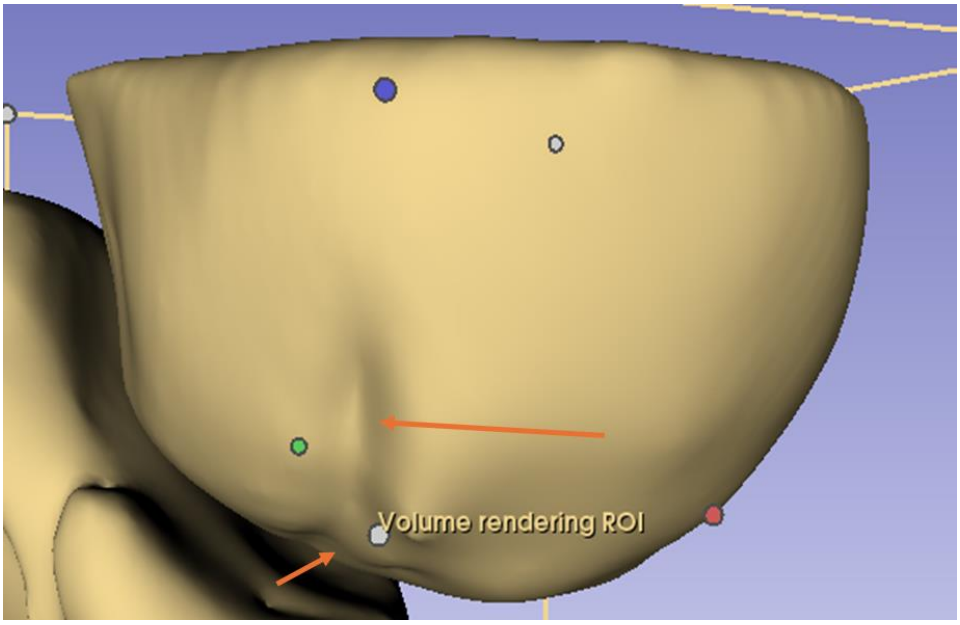


Figure 3.6. Close-up view of the physical view of noise on the humeral head and glenoid fossa.

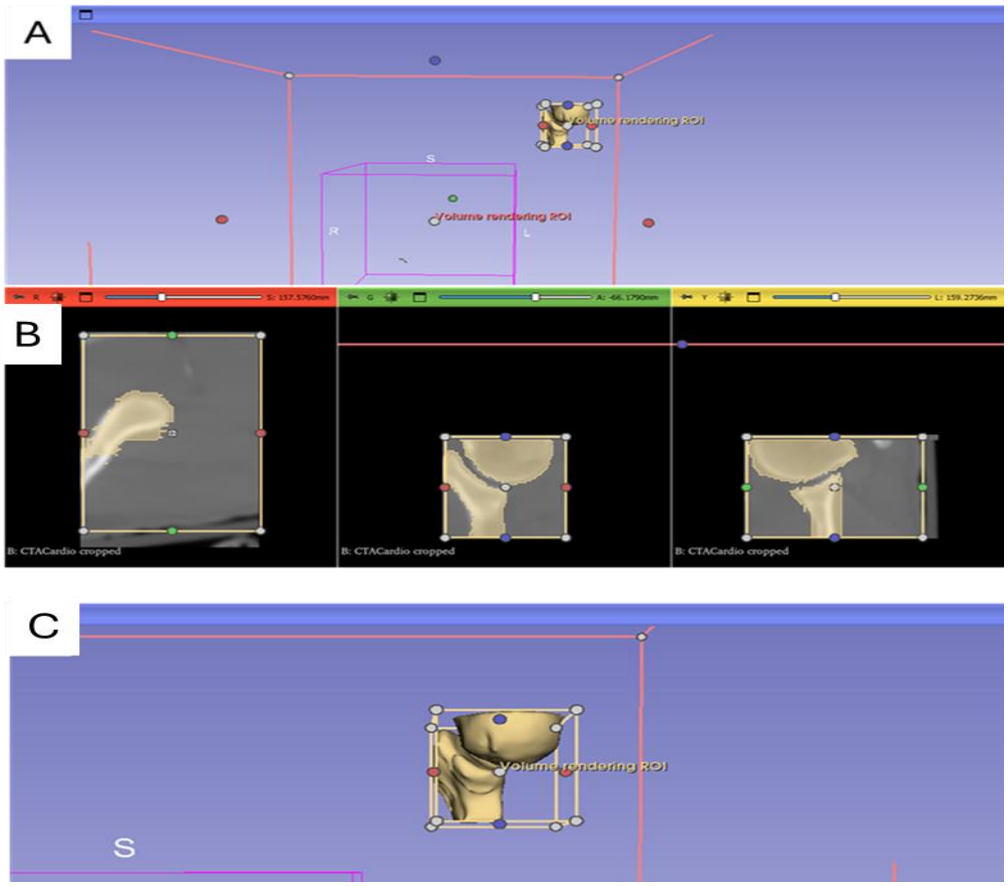


Figure 3.7. (A) Initial 3D image of the shoulder in the coronal plane after segmentation. (B) Segmented image directly on CT scan of sample data. (C) 3D shoulder joint after segmentation in the coronal plane chosen for 3D printing.

This model is exported as two .STL files, one for the glenoid and one for the humeral head. The process ensures that the two parts are free to move independently of each other during testing,

which simplifies the setup and makes it easier to obtain information about the motion of the humeral head with respect to the glenoid via the sensor array. The integrity of the files is verified by importing them into Autodesk Fusion360. The final model, shown in Figure 3.9, is made of ABS plastic.



Figure 3.8. (A) Axonometric view of the glenoid fossa model. (B) Axonometric view of the humeral head model.

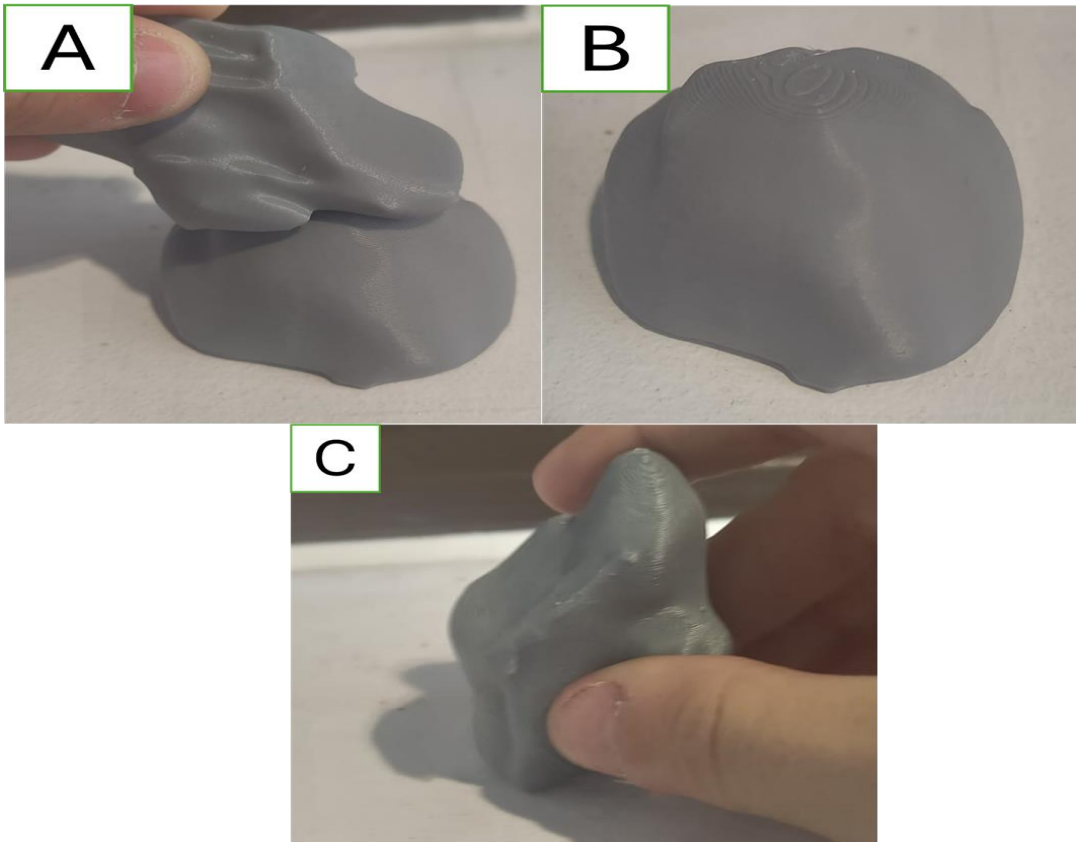


Figure 3.9. 3D printed shoulder joint. (A) Humeral head within glenoid fossa model. (B) Humeral head model. (C) Glenoid fossa model.

3.2 Sensor prototype testing

3.2.1 Testing setup

Tests used an LCX200 LCR meter by Rohde & Schwarz. A 100 nF capacitor with a 10% tolerance, distinct and independent from the sensor array, served as a test object to verify the accuracy of the testing equipment; it saw no further use in measurements pertaining to the sensor array.
To verify the accuracy of the equipment, the capacitance of the test object was calibrated independently on the LCX200 as well as a Hameg HM180. The latter returned a result centred on the 90 nF point, which was in line with the expected error margin as dictated by the capacitor's tolerance. The LCX200 returned values in a range between 67 and 86 nF, resulting in an error margin between 15 and 30%.
Further tests confirmed the repeatability of these measurements; the large error margin was attributed to the lack of calibration of the instrument when specifically measuring capacitance, as opposed to other components of energy loss, such as inductance or resistance. The system required external calibration, which was not scheduled until after project completion; however, collected results were repeatable and precise at a lower value than expected based on known value capacitors. Therefore, it was decided to continue with utilisation accounting for the reduction in accuracy, as no other equipment was available within the pF value readings at the frequency range needed for this experiment.

Two weight holders were prepared through 3D printing, both with a height of 50mm; the main difference between the two lay in the surface area. One had a surface of 14x14mm, sufficient to cover 3 rows and 3 columns on the array (thus polarising 9 sensing units at a time); the other had a surface of 18.5x18.5mm, covering 4 rows and 4 columns for a total of 16 sensing units. The system was tested in a laboratory area at a controlled temperature of 22°C (i.e.: room temperature) with a frequency of 500 kHz.

3.2.2 Testing methodology

During the tests, the sensor array rested on a Styrofoam base that would electrically insulate it from the work plane (shown in Figure 3.21). A shielding layer of Kapton tape, applied on top of both the driving and sensing lines, ensured that no external forces other than the pressure applied by the loads would affect the reading. The LCR meter probes were in contact with the electrical connections prepared through CST and manually held in place.

The main challenge in this setup lies in ensuring that the probes remain as steady as possible during testing, as misalignments would cause the capacitance to drift. This phenomenon is known as

baseline wander and is a type of amplitude noise. Preventing it simply requires that the probes are forced in place during the experiment (for example, taping the probe within a holding claw and steading it with Kapton tape). The full setup appears in Figure 3.21.

The control parameter of this experiment was the mass of a test object weight, made up of weighted beads filling the holder used to load the sensor. The resulting pressure would be calculated from the beads' mass as per equation (2-12). A consequence of the change in the variables of interest is that the sensitivity formula employed during the simulation, described within section 3.1.1, cannot be used. In this case, it is possible to use a basic rational formula instead.

$$S=\frac{\Delta C}{C} \qquad (3\text{-}3)$$

The weight holder was filled with 5 beads, each with a mass of 2g. When adding the weight of the holder itself, the total load was of 12g. During the final batch of tests, after it was ascertained that the sensor behaved in line with the expected models, the weights were replaced with the shoulder model described in section 3.1.3, 3D printed in ABS plastic based on shoulder data extracted through the open-source software 3D Slicer (3D Slicer, n.d.).



Figure 3.9. Sensor testing setup.

3.3 Conclusion

As explained previously, this project focuses on a qualitative analysis articulated in two phases: one dedicated to simulations and the other to real-life manufacturing. The methodological analysis

heretofore conducted outlined the limits of the simulation and experiments, confirmed the choice for a qualitative analysis and informed the decision to perform simulations through a top-down design approach. The simulations began with fundamental experiments, aimed at verifying the basic principles underlying the sensor development, such as the control variables or mathematical models that connect the mechanical and electronic aspects of this research. Conversely, after the key parameters had been established, the real-life tests followed a bottom-up design. Starting from a model based on the simulations performed during the first phase of development, a number of experiments were performed to understand the limits of the simulated design, for example during measurement or manufacturing.

The development of the readout circuit paused to allow time for the experiments during the transition from the first to the second phase of development. During this period, the readout circuit's final revision reached its conclusion. The simulations calculate the displacement of different sensing units and measure the corresponding capacitance change. The results will serve as a basis to produce a mathematical model, which will inform further developments of simulations and aid in setting up the conditions in which to conduct the real-life tests. The experiments received extensive assistance from various pieces of software, through which critical components for use in the test setup will be developed, ranging from the prototypes themselves to test objects with which to conduct measurements.

Chapter 4
Simulations of the array

This chapter details in chronological order the simulations conducted on a 3D model of the array and any changes this model was subject to during development, beginning with a flat array that was later divided into segments (hereafter referred to as a segmented array). These tests followed an iterative process for each model, with a new iteration beginning whenever significant changes to the model were made. Here the results obtained from different simulations, organised by model type (i.e.: flat, curved, or segmented), are registered.

Initial tests simulated pressure applied on single sensing units at a time; after the final design was completed, the simulation expanded to encompass larger test areas, with pressure applied on multiple sensing units at a time. To reduce computational time, these sensing units all share a single variable for the z-axis locations of their surfaces. Spherical and hemi-toroidal loads were successfully tested for by applying a uniform displacement to multiple sensing units, with the former employed as a base for manufacturing. The dielectric was a silicon sheet with size 30x30x0.5mm, later changed to 35x35x0.5mm to accommodate an additional row and column.

4.1 Flat array

This section aims to show the different forms that the flat array simulation took, and the data gathered from each of these according to the principles established in section 3.1.1. During these early simulations, both faces of the sensing electrodes operated independently for computational purposes, meaning that each change to the variable zElectrodeXY was accompanied by an equal change in the variable zLoadXY. This means that each simulation run would employ two parameters changed across five steps (from 0.5mm to 0.1mm), totalizing 25 calculations as per Equation (3-1). The tests, conducted on electrode (3; 4) were referred to in tables and graphs as zElectrode34. Unless stated otherwise, all testing took place centred around this electrode.

4.1.1 Array trial run

Iteration 1 used a silicone dielectric interspersed with air gaps. The electrodes laid over both the silicone and gaps without any separation, as shown in Figure 4.1. This iteration relied on a 7x7 array with each electrode having a dimension of 5x5x0.5mm; the dielectric had a thickness of 0.5mm. Both the bulk silicone and air sections of the dielectric had the same size as the respective electrodes, for a total size of 35x35x0.5mm. Initial simulations polarised a single electrode line at a time; the results from these tests are shown in Table 1. The tests were conducted across the range $R \in [1;\ 0.5[$ mm.

The lower extreme of this range is not included: without any separation, the charge is free to flow across the wire, which assumes a uniform potential (Ling, Moebs, & Sanny, 2016).

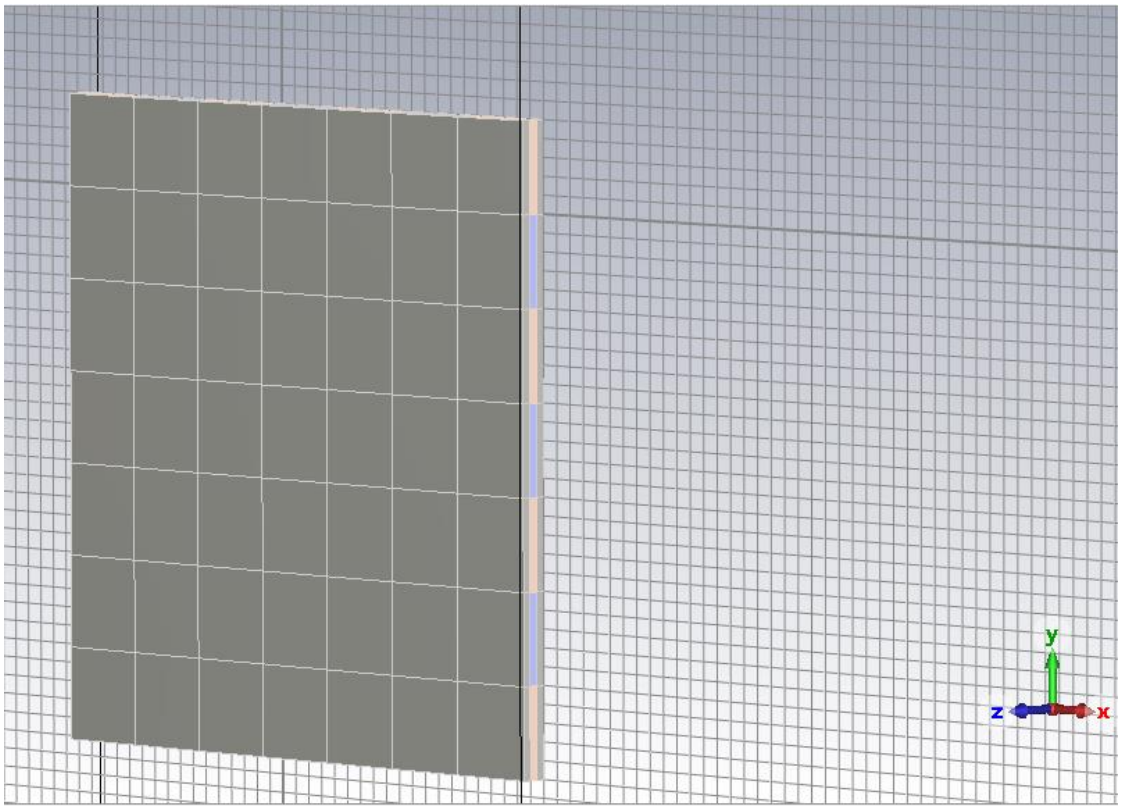


Figure 4.1. Iteration 1 of flat array. All electrodes (in grey in the image) are close to each other without any separation, and the dielectric layer (pink in the image) is filled with "holes" represented by air gaps (blue in the image).

Table 1. Capacitance change with respect to displacement in iteration 1.

zElectrode34 (mm)	Capacitance (F)
1	1.44E-10
0.9	1.44E-10
0.8	1.45E-10
0.7	1.47E-10
0.6	1.50E-10

The results of this test were used to produce a curve of the displacement in relation to the capacitance, shown in Figure 4.2. The same procedure took place for the sensitivity with respect to the displacement, which was calculated through equation (3-2); the resulting curve is shown in Figure 4.3. This initial simulation already shows the basic form of the model described in (Dahiya, Ozioko, & Kumaresan, 2021) and the principles laid out in sections 2.2.1, 2.2.2 and 2.2.3, showing pressure as a logarithmic function of sensitivity. In the present simulations, the relationship between displacement

and sensitivity from Figure 4.2 appears as the inverse function of the one between pressure and sensitivity, which manifests as an exponential function. Of this function, the third-order polynomial function showed in Figure 4.2 and 4.3 is a particular case.

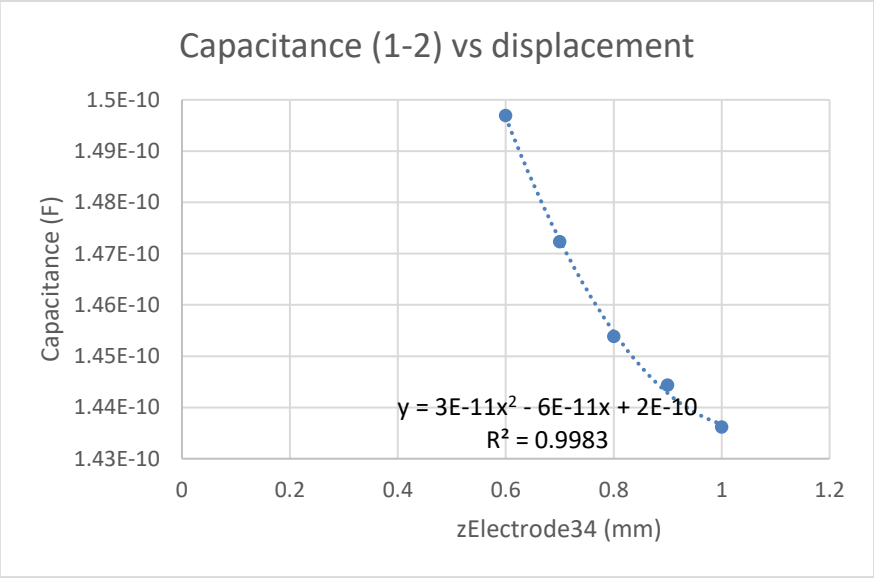


Figure 4.2. Curve of displacement in relation to capacitance.

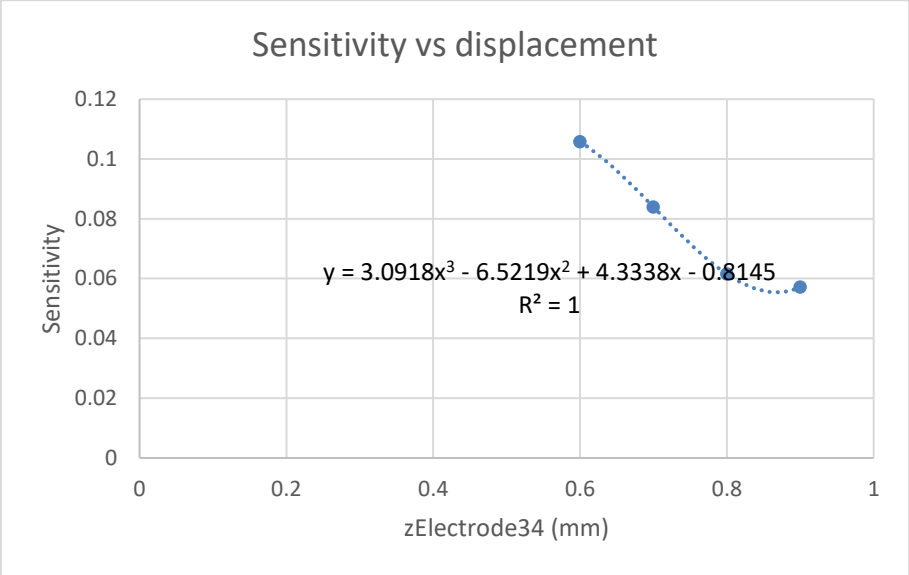


Figure 4.3. Curve of sensitivity in relation to displacement.

The displacement being a third-order polynomial function is a reasonable expectation, in line with the literature (Zhou, Dazhuan, Tu, & Shi, 2020). Previous experiences proved that the relationship between capacitance and frequency is a second-order differential equation of time, expressed as a second-order linear equation of frequency through a Laplace transform. This can be seen by expressing the voltage term in (2-3) as an exponential function of the angular frequency at which the signal is transmitted and the time of the same.

In such model, the charge in the time domain is equal to the charge stored across a summation of infinitesimally small periods, summed together via integration. Though precise measurements of the charge are beyond the scope of this project, it is known that the charge distribution can be expressed as a function of the frequency through the following integral:

$$C \propto \int_{t_0}^{t} Q^{*} e^{-j\omega t}\, dt \qquad (4\text{-}1)$$

where C is the capacitance, t_0 is the lower limit of the time when the phenomenon is observed, t is the upper limit of the same, Q is the charge, ω is the angular frequency of the signal and $e^{-j\omega t}$ is the energy absorbed by the dielectric over an infinitesimally small time dt. This formula is proportional to the Fourier transform integral, itself a variation on the Laplace transform integral. The diffusion of the charge across space, on the other hand, appears from equation (2-3) to be a first-order linear equation; no terms can be written as higher-order functions. The charge the electrodes store will increase the more that are located within a constant area, following what was described in section 2.2.3. This means the total charge will be therefore dependent on the charge stored at a certain point in time and the "spatial frequency" of the array – the concentration of charge in a point on its surface. The and-multiplication rule yields the product of a second-order equation of frequency with a first-order equation of the same, resulting in a third-order equation.

However, because only a single electrode line was polarised at any given time, the change in capacitance (which appears in figure 4.2) is particularly small. Table 1 shows that only the largest possible displacement of 0.4mm produces a sensitivity in line with the values found in the literature. This specific data point shows a capacitance change between 10 and 16% mm^{-1} (Sara Rachel Arussy Ruth, 2020) with respect to the initial value. A further reason for these results lies in the lack of separation between electrodes, which caused strong crosstalk: when a force acts on the sensor and displaces a single sensing unit, its proximity to others of its kind along the same row and column causes them to become polarised, as if the same force also acted on them. In conclusion, the data produced by this simulation, while successfully obeying the mathematical relationship expected to exist between capacitance, displacement and sensitivity, is not sufficient to validate it without further testing.

With an iterative top-down design established for the simulations, the initial solution was to reduce the number of sensing units. This led to excluding alternating sensing units from the simulations, leaving the bulk silicone section of the dielectric untouched as a medium for the electrical field to project across, similar to a chessboard. The new model appears in Figure 4.4. The readings listed in

Table 2 and the curves in Figure 4.5 and 4.6 follow the same model employed previously. The same curves for capacitance and sensitivity were plotted using this data.

The highest possible displacement this time produced a sensitivity of 0.37 mm^{-1} (a 37% increase in capacitance per tenth of a mm of displacement), which confirmed that the crosstalk between sensors was affecting sensitivity and that separating the electrodes was a solution to the problem; however, the fewer number of electrodes caused a marked drop in the capacitance, as seen by comparing the values in Table 1 to those in Table 2. By this point, the sensor model and testing methodology were definitively established, and as such a third simulation run was begun in search of a means to maintain the electrodes separated while keeping their number constant.

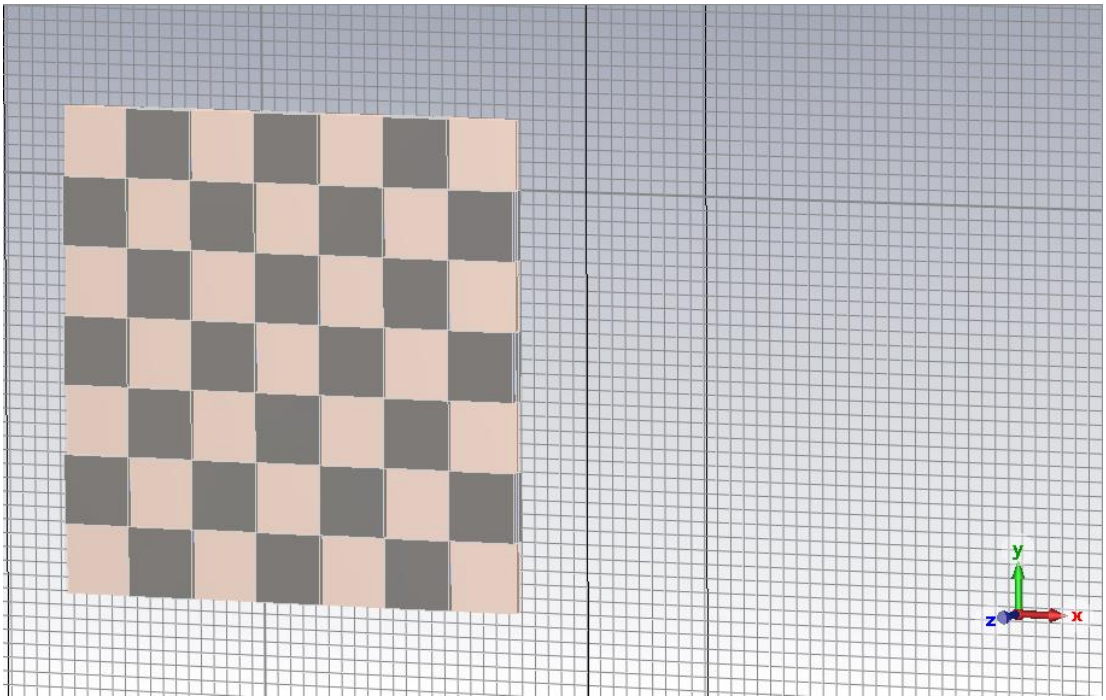


Figure 4.4. Iteration 2 model side view. Half the electrodes on both sides were excluded from simulation, leaving the "chessboard" pattern seen in the image.

Table 2. Iteration 2 capacitance readings in relation to displacement of electrode (3; 4).

zElectrode34 (mm)	Output capacitance (F)
1	3.04E-11
0.9	3.08E-11
0.8	3.15E-11
0.7	3.22E-11
0.6	3.49E-11

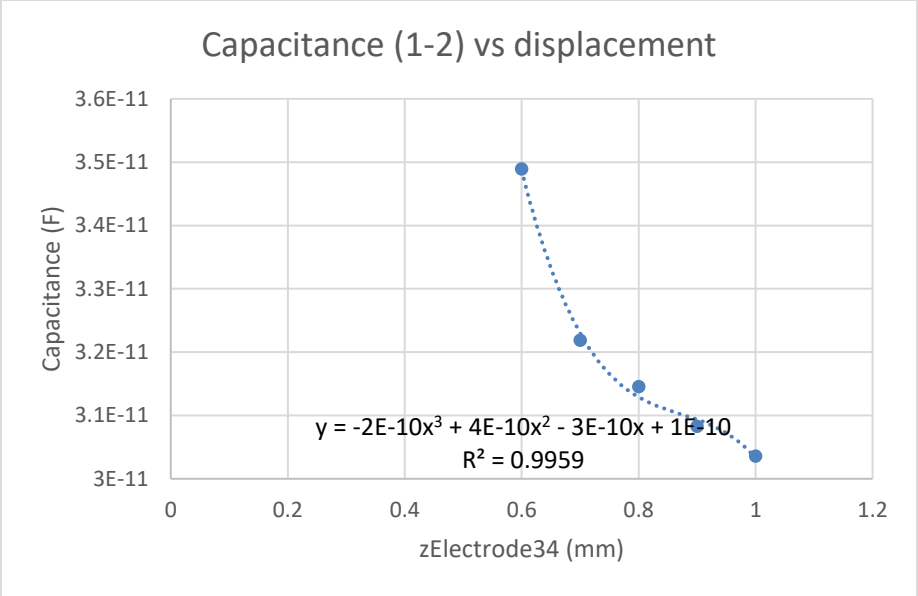


Figure 4.5. Curve of capacitance in relation to displacement.

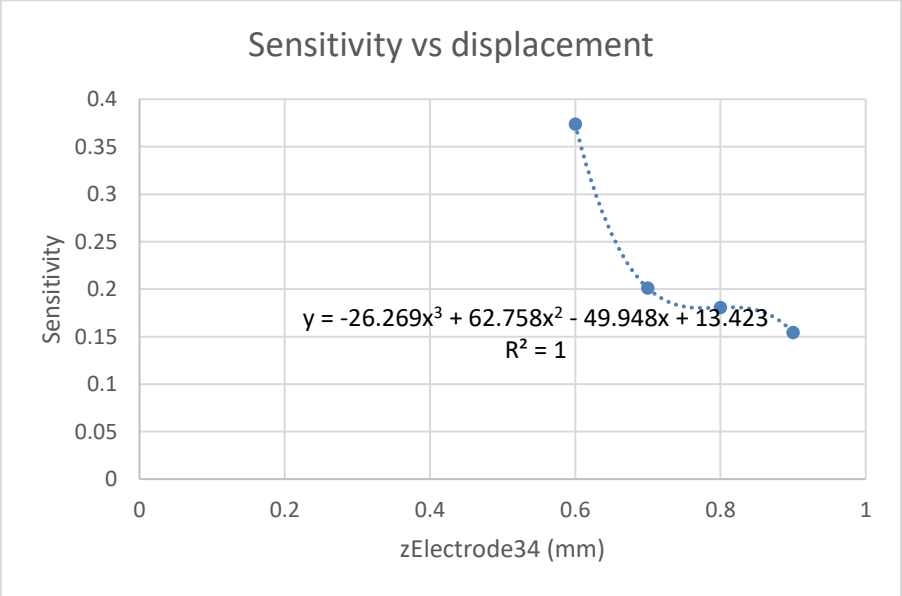


Figure 4.6. Curve of sensitivity in relation to displacement.

4.1.2 Complete flat array

Iteration 3 saw a marked change to the dielectric and electrode geometry. First, the dielectric material was changed to bulk silicone, instead of employing the “chessboard” pattern used in the first two simulations. Figure 4.7 shows the resulting 3D model. The readings were obtained using the same methodology as previous simulations. Tables 3 and 4 show the results. The same happened with the capacitance and sensitivity curves, shown in Figure 4.8 and 4.9 respectively.

Due to the lack of crosstalk, the sensitivity of the system became much larger, at the cost of a lower initial reading when compared to the previous simulations. This result was expected, as the intensity of the electrical field projected is proportional to the distance between the source and receiver via the inverse-square law:

$$E_T \propto \frac{E_1 E_2}{d^2} \qquad (4\text{-}2)$$

where E_T is the energy exchanged between two point sources of energy, E_1 and E_2 respectively, separated by a distance d (Gea-Banacloche, 2019). In this case, the point sources are two adjacent sensing units, and the energy exchanged between them is a consequence of the force acting on them.

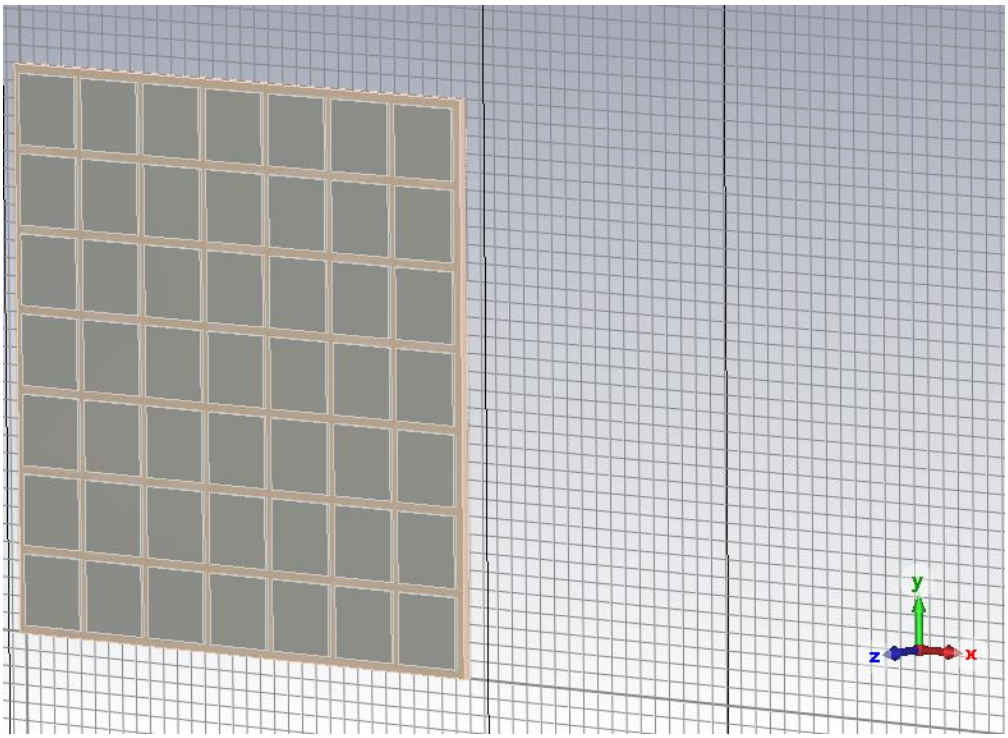


Figure 4.7. Iteration 3 model.

Table 3. Capacitance in relation to displacement (iteration 3).

zElectrode34 (mm)	Capacitance (F)
0.5	3.86E-12
0.4	4.86E-12
0.3	6.36E-12
0.2	9.39E-12
0.1	1.88E-11

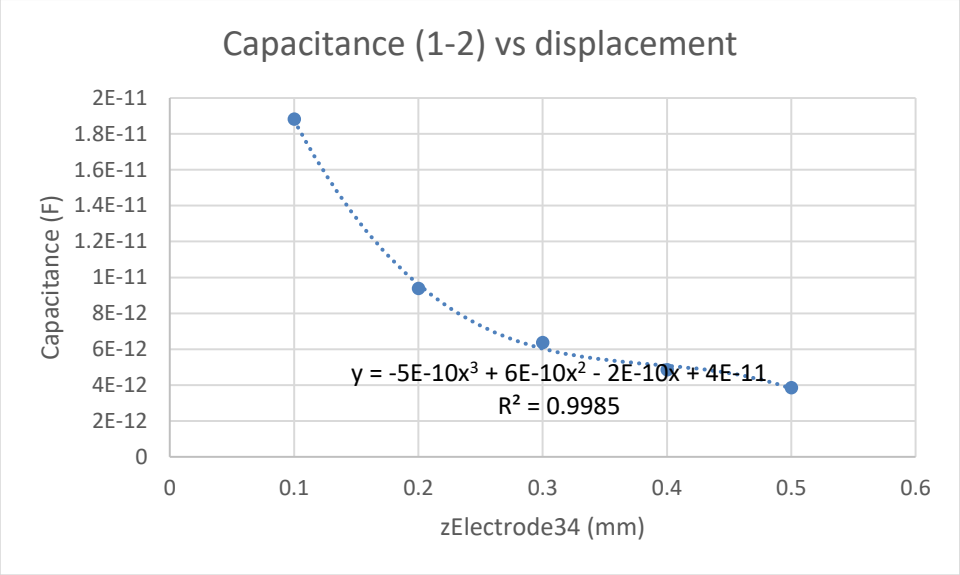


Figure 4.8. Curve of capacitance and displacement.

The greater distance, however, has the beneficial advantage of reducing the parasitic effects that exist between electrodes, which characterised the crosstalk responsible for the lower sensitivity of the previous two simulations. This simulation produced satisfactory results, and as such it was used as a base for subsequent simulations, as well as the manufacturing of prototypes. The relationship between capacitance and displacement is much more clearly visible as a third-order equation of displacement, and close to what is described in the literature.

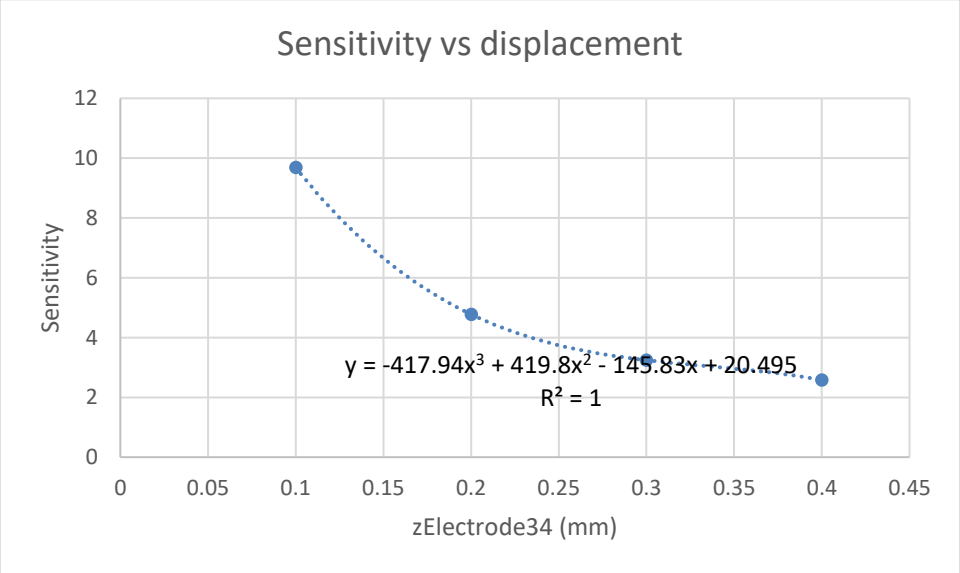


Figure 4.9. Curve of sensitivity and displacement.

One final simulation run based on the same flat array 3D model was conducted after completion of the curved array tests. This new test aimed to examine the differences between the different models, as well as reducing the computational time required by each simulation. The main point of

divergence was the inclusion of a separator to prevent further crosstalk. This separator filled the 0.5mm gap between electrodes and consisted of epoxy resin. A further change was the introduction of a silicone base on which the sensor would rest, itself located on top of the tissue phantom. The methodology discussed in section 3.1.2 allowed to measure the permittivity of the phantom base. Figure 4.10 shows the 3D model, while Table 4 displays the data retrieved from this iteration. Lastly, the curves for capacitance and sensitivity in relation to displacement are recorded in Figure 4.11 and 4.12.

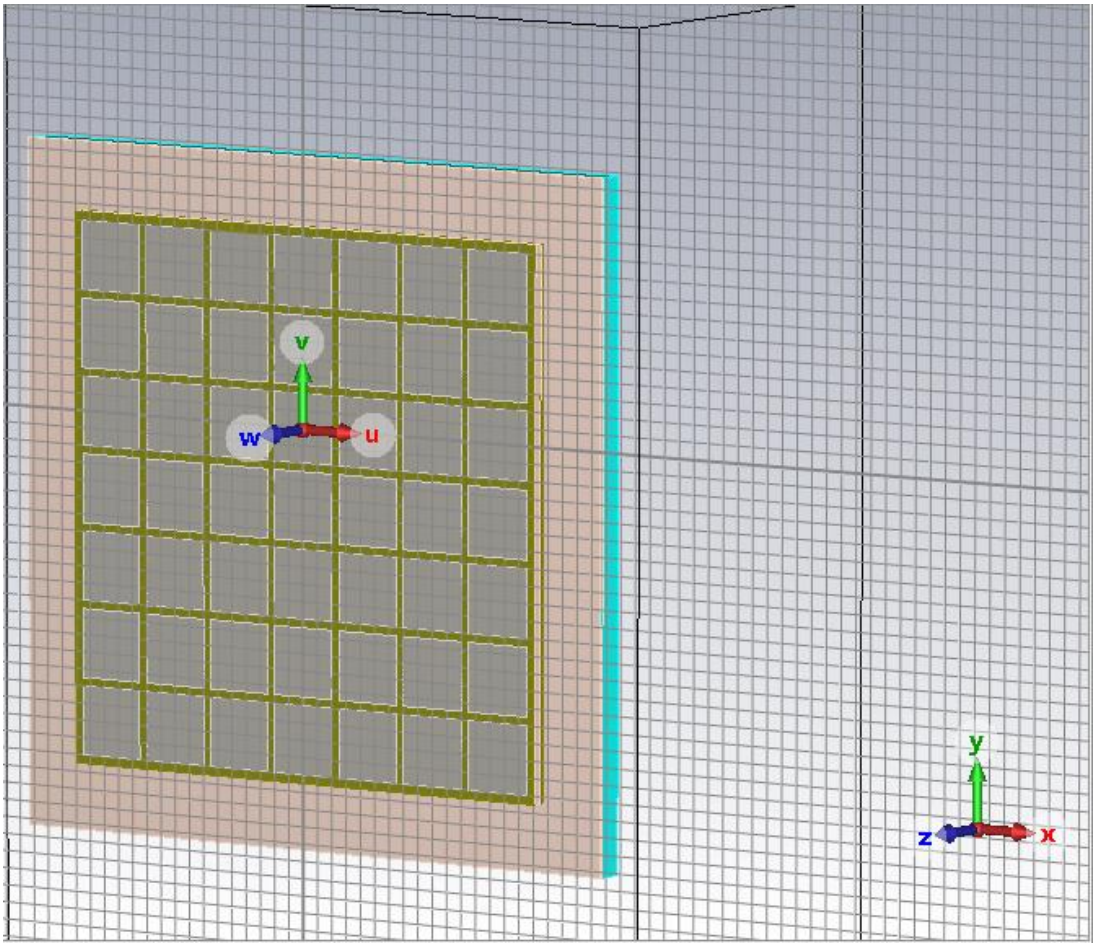


Figure 4.10. Iteration 4 simulation model. The separator is highlighted in yellow.

Table 4. Capacitance readings in response to the displacement.

zElectrode34 (mm)	Capacitance (F)
0.5	4.02E-12
0.45	4.34E-12
0.4	4.83E-12
0.35	5.60E-12
0.3	6.37E-12
0.25	7.88E-12

0.2	9.79E-12
0.15	1.27E-11
0.1	1.87E-11

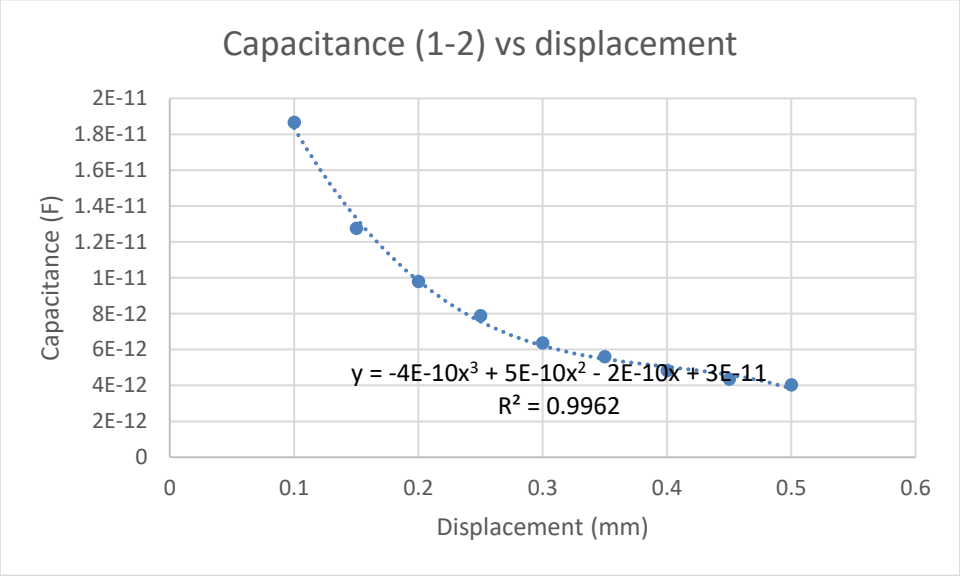


Figure 4.11. Curve of capacitance with respect to displacement.

The faster computational time, accomplished by constraining together the two faces of the test electrode, allowed for the retrieval of more data points. As a result, the curve became closer to the results expected from the literature. This also clearly appears when comparing the average capacitance changes between iterations 3 and 4, which show a small change between each other, approximately 0.05pF.

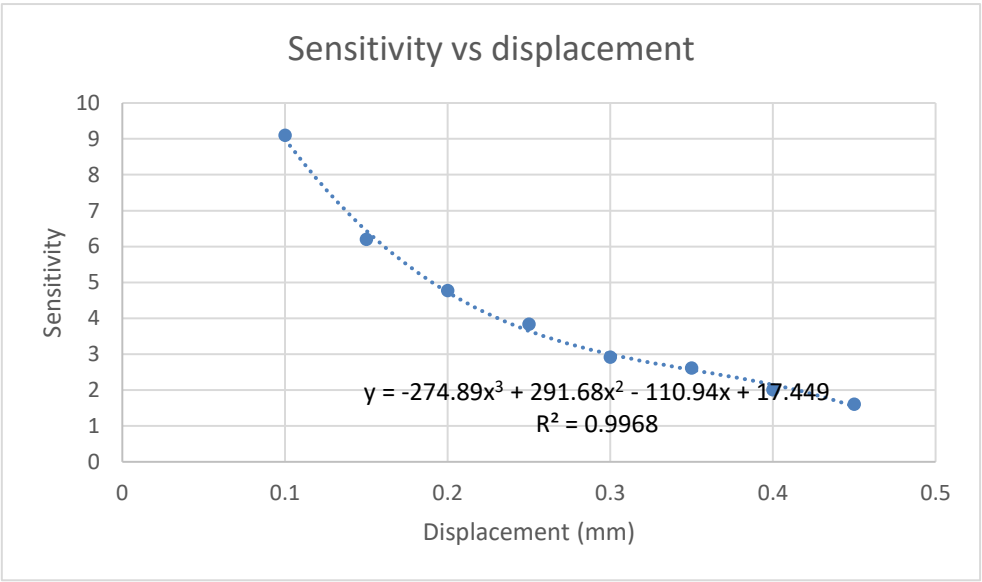


Figure 4.12. Curve of sensitivity with respect to displacement.

4.2 Curved array simulations

The first step in the production of the curved array model was to convert the flat array model into a circular one. This process was performed by applying a cylindrical constraint on the 3D model developed up to that point. The key parameter during this operation is the curvature radius, which was set to 10 mm. The electrode and dielectric dimensions and spacing remained the same they were so far. The curved array model was the one that was tested the most; multiple variations on the data were observed.

4.2.1 Array curving

As stated above, the base for the curved array was the flat array model previously simulated; this was curved employing a cylindrical constraint of radius 10mm. An alternate working coordinate system was set on electrode (3; 4), which was the one currently under test. The y-axis of the new working coordinate system became the pivot point for the cylinder, shown in Figure 4.13. The axes were labelled separately from the global coordinate system: u = x, v = y, w = z. A single sensing and driving line were polarised at a time, much like in previous flat array simulations. Other than the model, the methodology remained the same, as did the number of calculations to perform. Table 5 shows the data retrieved. From these values, the sensitivity was studied through Equation (3-2) and registered in Table 5 and Table 6. The results obtained for the sensitivity display in Figure 4.14.

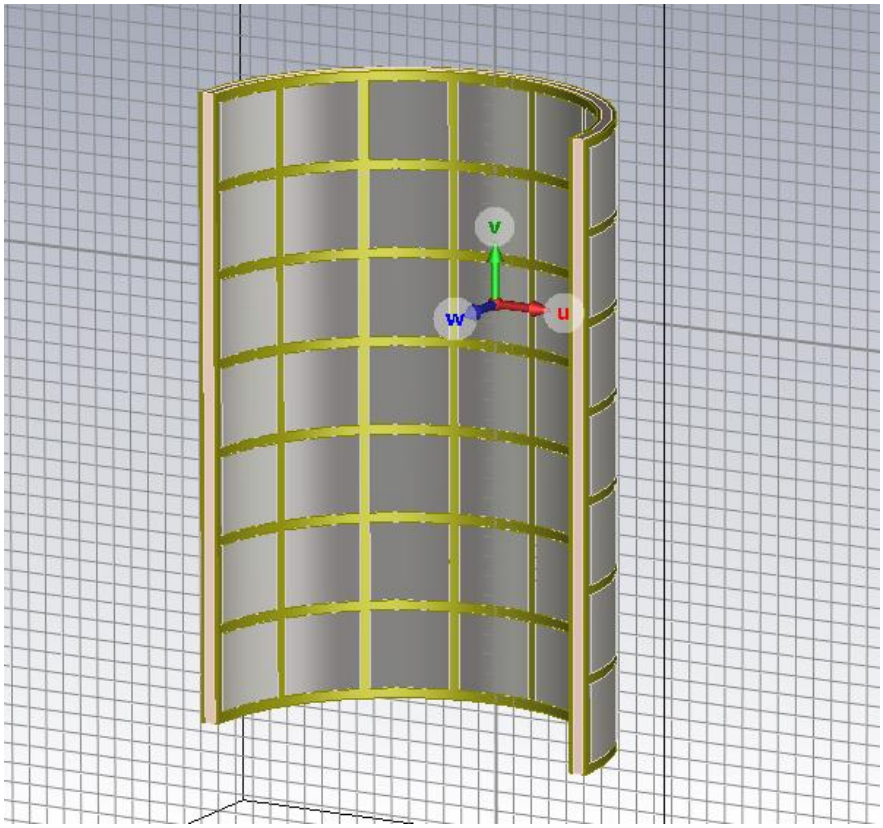


Figure 4.13. Curved array iteration 1 model. The working coordinate system is in the centre of the test object.

Table 5. Capacitance vs displacement in curved array iteration 1.

zElectrode34 (mm)	Capacitance (F)
0.5	4.05E-12
0.4	5.06E-12
0.3	6.64E-12
0.2	1.01E-11
0.1	1.85E-11

Table 6. Sensitivity per unit of displacement.

zElectrode34 (mm)	Sensitivity
0.4	2.518
0.3	3.201
0.2	4.956
0.1	8.958

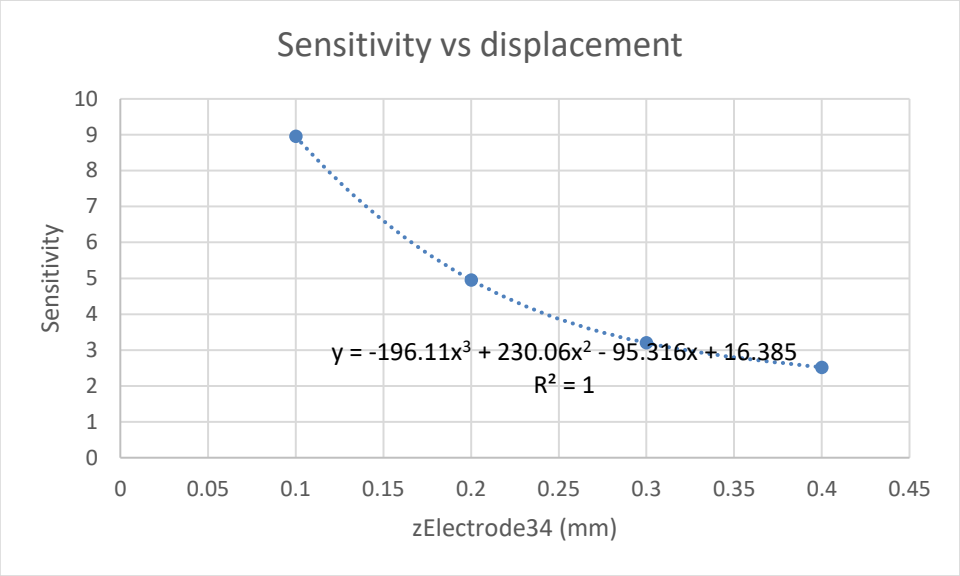


Figure 4.14. Sensitivity in response to displacement in curved array, iteration 1.

4.2.2 Final curved array trial

Tests conducted on the curved array made use of a single variable as control parameter, obtained by imposing zElectrodeXY to be dependent on zLoadXY. The variable zElectrodeXY, representing the bottom of the sensing unit, was declared to be equal to the total of the variable zLoadXY (the top of the sensing unit) and the electrode width, equal to 0.2mm. As a part of these tests, the step width was reduced from 0.1 mm to 0.05 mm.

The new simulations also introduced the silicone base, which rested on top of the body phantom. Their dimensions are described in section 3.1.1. The new components had only a limited effect on the results of the simulation and were maintained subsequently thereafter. Figure 4.15 shows the finished 3D model; testing on this model produced the capacitance and sensitivity presented in Table 11 and Table 12 respectively. The curves showing the relationships between capacitance and sensitivity with displacement appear in Figure 4.16 and Figure 4.17 respectively.

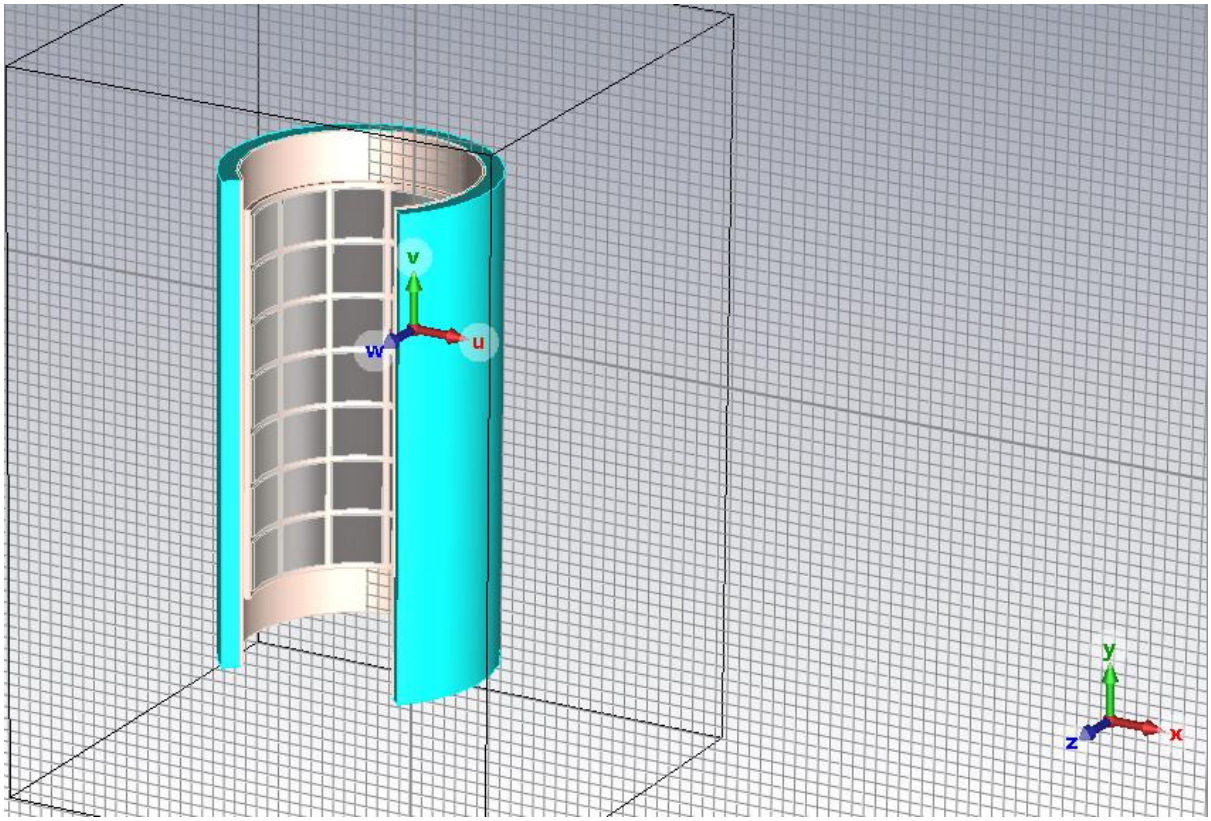


Figure 4.15. 3D model of curved array integrating all features, including the body phantom. Both the global and working coordinate systems are showed in this image.

Table 7. Relationship between capacitance and displacement in the curved array.

zElectrode34 (mm)	Capacitance (F)
0.5	4.08E-12
0.45	4.53E-12
0.4	5.18E-12
0.35	5.75E-12
0.3	6.65E-12
0.25	7.82E-12
0.2	8.58E-12
0.15	1.26E-11
0.1	1.81E-11

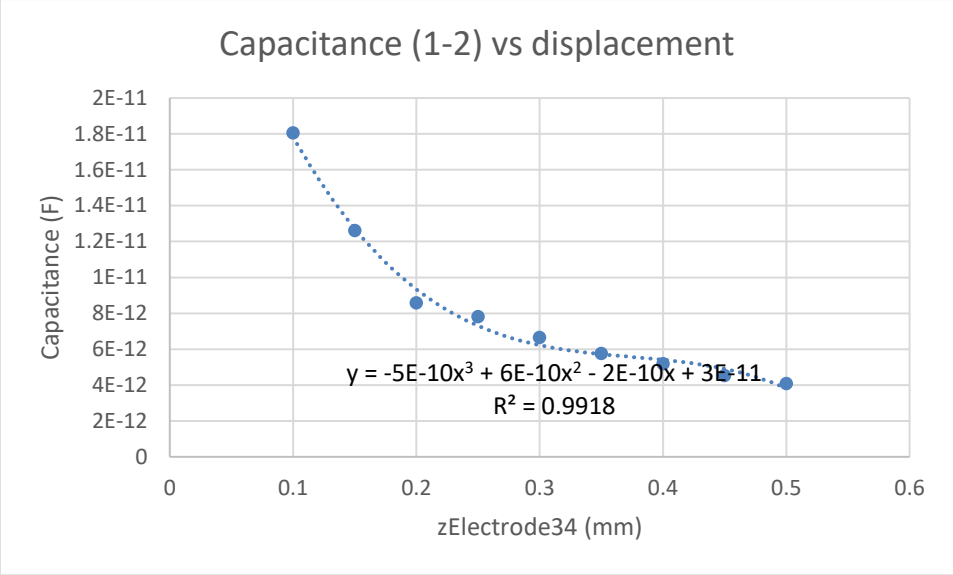


Figure 4.16. Capacitance-displacement curve in the corrected curved array.

Table 8. Sensitivity against displacement in the corrected curved array.

zElectrode34 (mm)	Sensitivity (norm)
0.5	0
0.45	2.182
0.4	2.696
0.35	2.727
0.3	3.146
0.25	3.663
0.2	3.670
0.15	5.973
0.1	8.556

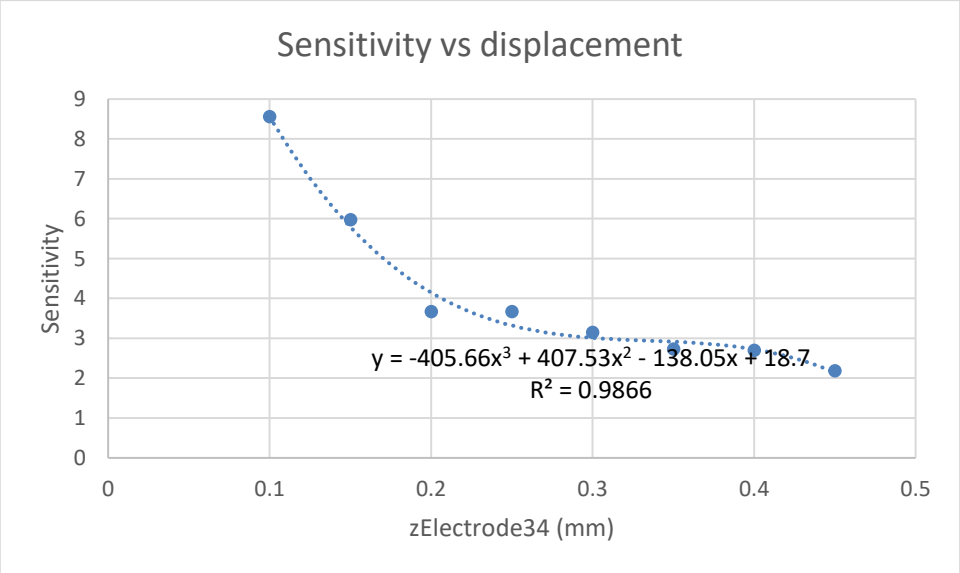


Figure 4.17. Sensitivity-displacement curve in the corrected curved array.

The 3D model produced during these tests returned satisfactory results; consequently, it was further built upon by reintroducing a physical separator between the electrodes. Figure 4.18 shows the changes to the model. The separator brought an increase in the accuracy of the values, which manifests as an increased R^2 value in the simulations conducted on the array that had it. The capacitance values (recorded in Table 13) remained mostly the same, but the sensitivity (shown in Table 14) increased slightly. The curves for the capacitance and sensitivity with respect to displacement show the increased accuracy margin much more clearly; these are present in Figures 4.19 and 4.20 respectively.

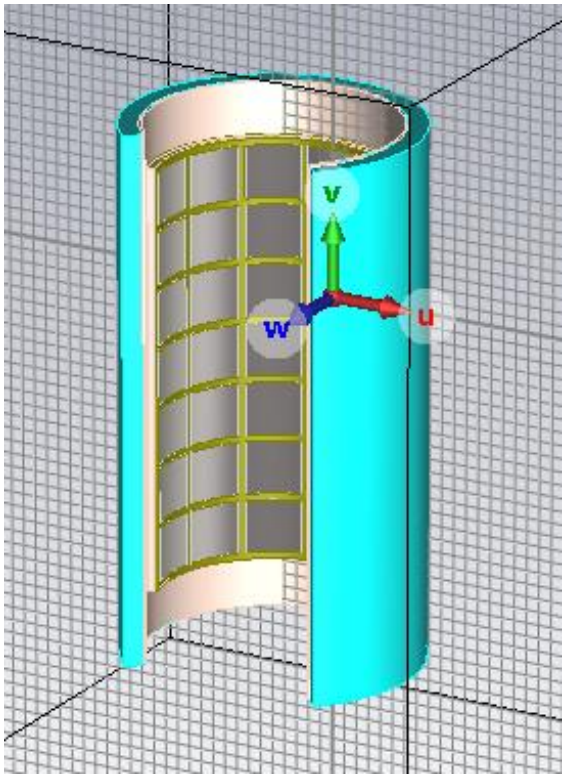


Figure 4.18. 3D model of the curved array with the separator (highlighted in yellow). Only the local coordinate system is shown.

Table 9. Capacitance compared against displacement in the curved array with the separator.

zElectrode34 (mm)	Capacitance (F)
0.5	4.08E-12
0.45	4.53E-12
0.4	5.00E-12
0.35	5.68E-12
0.3	6.59E-12
0.25	7.91E-12
0.2	9.72E-12
0.15	1.32E-11
0.1	1.83E-11

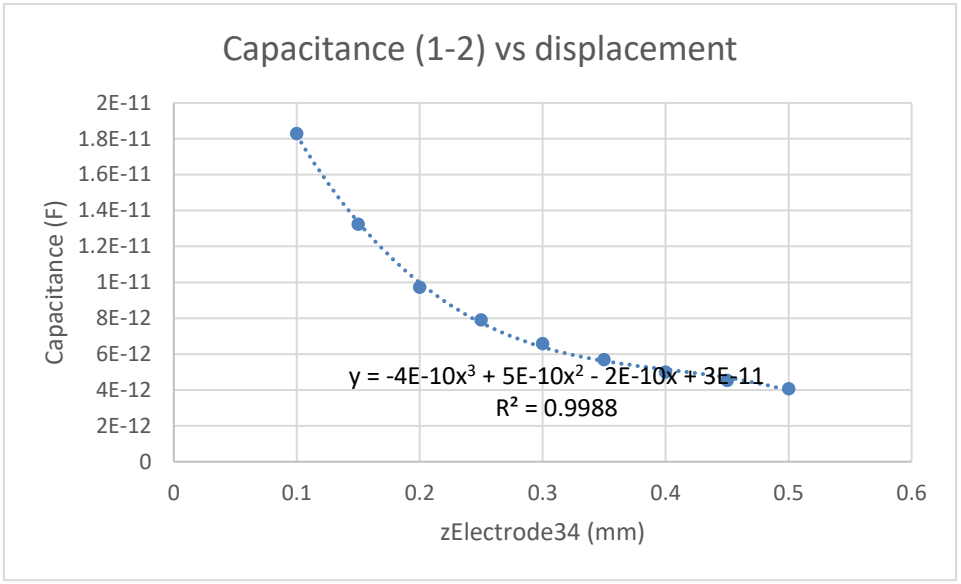


Figure 4.19. Capacitance-displacement curve in the curved array with the separator.

Table 10. Sensitivity values in the curved array with the separator.

zElectrode34 (mm)	Sensitivity
0.45	2.215
0.4	2.268
0.35	2.631
0.3	3.082
0.25	3.764
0.2	4.615
0.15	6.426
0.1	8.723

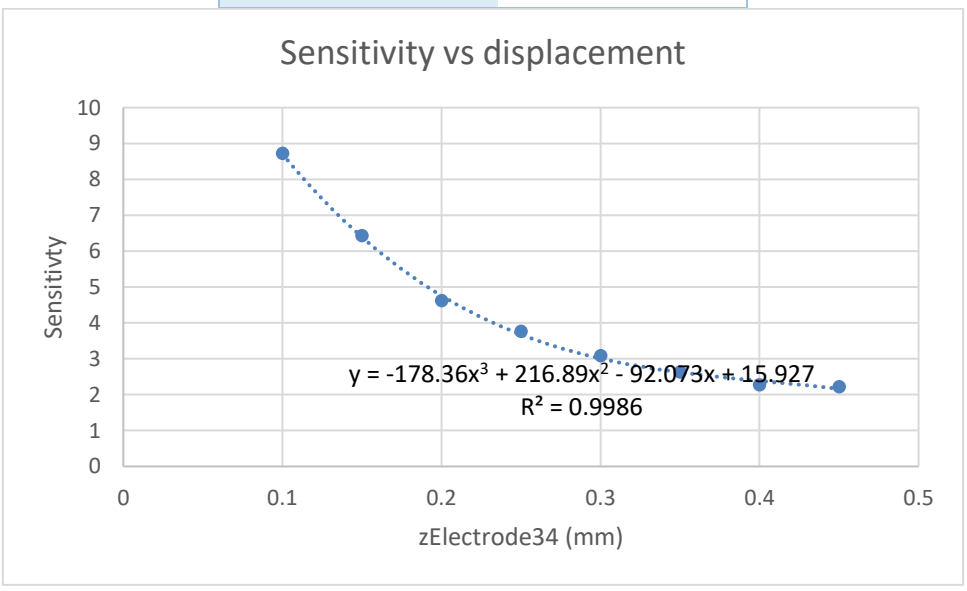


Figure 4.20. Curve of sensitivity compared against displacement in the curved array with the separator.

4.3 Segmented array simulations

4.3.1 New workflow

The results concerning the simulation workflow and sensor data served to prepare a new simulation run. In the new model, which returned to a flat array, the separator changed to only filling the central region of the array, dividing it into four quadrants, each containing a set of 16 electrodes. In this simulation run, an additional row and column of sensing units were added, bringing the array resolution to a total of 64 units. The new model is shown in Figure 4.21. The same coordinate system and convention used for the sensing units was used when naming the four quadrants. Quadrant 1 was close to the origin of the standard Cartesian axes, and all the others followed in an anticlockwise pattern. The working coordinate system for calculations was established at the centre of the quadrants, between electrodes (3; 4), (4; 4), (3; 3) and (4; 3).

Through this new workflow, it was possible to conduct new tests for displacements affecting multiple sensing units. The methodology was the same used in previous simulations, and the z-axis coordinates of sensing units close to each other were linked together to simulate the displacement of multiple objects at a time.

Three loading patterns were tested: spherical, conical, and toroidal (Cheng, 2023). Furthermore, the entire array was polarised. Due to the combination of a greater concentration of electrical charge on both layers of the sensor array and to the fact that multiple sensing units were displaced, capacitance was registered to be in the hundreds of pF range, as opposed to the single pF of previous iterations, where only single sensing units were moved at a time.

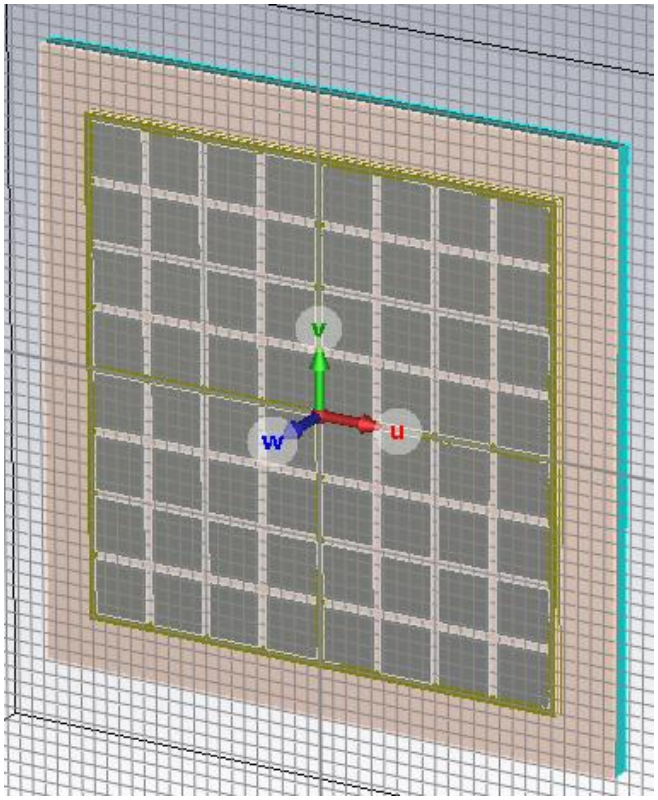


Figure 4.21. Axonometric view of the segmented array. The local working coordinate system, introduced during the curved array simulations, is at the centre of the separator.

4.3.2 Spherical load

Multiple tests were conducted across several electrodes. The most common one used during testing was the set centred around electrode (1; 6), which contained electrodes (1; 7), (2; 5), (1; 5), (2; 6), (2; 7), (0; 5), (0; 6) and (0; 7). Tables 15 and 16 show the capacitance changes and sensitivity respectively. Figures 4.22 and 4.23 show the resulting plots of capacitance with displacement and sensitivity with displacement respectively.

Table 11. Capacitance change in relation to electrode displacement for a uniformly distributed spherical load.

zElectrode16 (mm)	Capacitance (F)
0.5	2.51E-10
0.45	2.52E-10
0.4	2.53E-10
0.35	2.53E-10
0.3	2.54E-10
0.25	2.59E-10
0.2	2.65E-10
0.15	2.73E-10
0.1	2.86E-10

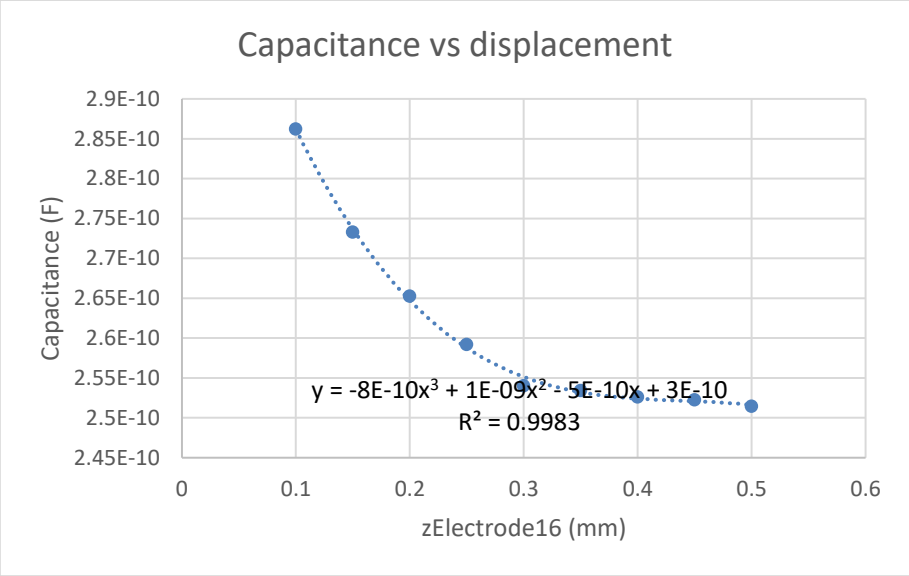


Figure 4.22. Capacitance-displacement curve in segmented array acted on by a uniformly distributed spherical load.

Table 12. Sensitivity in relation to displacement in array acted on by distributed spherical load.

zElectrode16	Sensitivity (normalised)
0.5	0
0.45	0.063
0.4	0.046
0.35	0.052
0.3	0.052
0.25	0.124
0.2	0.183
0.15	0.248
0.1	0.345

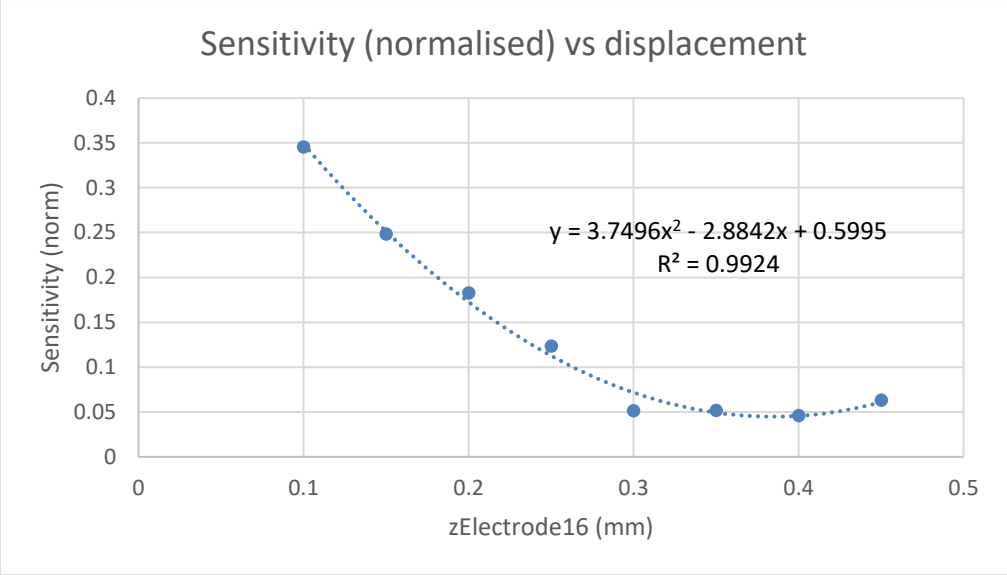


Figure 4.23. Sensitivity-displacement curve for spherical load on segmented array.

As can be seen in Table 11, the array sensitivity has significantly decreased and is now within a similar range to those found in the literature (Dahiya, Ozioko, & Kumaresan, 2021). As the sensitivity increases, the signal becomes much more susceptible to interference due to the frequency of the measurand signal being higher. The intensity of the capacitance is much higher than in previous iterations, with a base value of approximately 250 pF, two orders of magnitude greater than the 4 pF in of the flat array. This occurrence is a consequence of both the larger load and the voltage applied to the entire array; the only influence on the capacitance comes from the displacement. A subsequent simulation run that built upon these results reduced the thickness of the electrodes to 0.3 mm from the initial 0.5mm value. Table 17 and 18 show the new values for capacitance and sensitivity respectively; the new curves of capacitance with displacement and sensitivity with displacement are in Figure 4.24 and 4.25 respectively.

Table 13. Capacitance change with displacement in segmented array with thinned out dielectric and electrodes for a spherical load.

zElectrode16	Capacitance (F)
0.3	3.29E-10
0.25	3.31E-10
0.2	3.33E-10
0.15	3.36E-10
0.1	3.41E-10
0.05	3.70E-10

The capacitance changes curve shows that under these conditions the array is more prone to noise than previous iterations due to the smaller range of available displacements, increasing the upper

limit for the sensitivity value (from the previous 0.34 to 0.49). By contrast, the capacitance values are much larger (from 251 pF to 329 pF), which makes the signal easier to pick up in the intracorporeal environment. This sensor was deemed fit for manufacturing and was used as the basis for the variable capacitor footprint described in section 3.2.1, which would be used for the readout circuit.

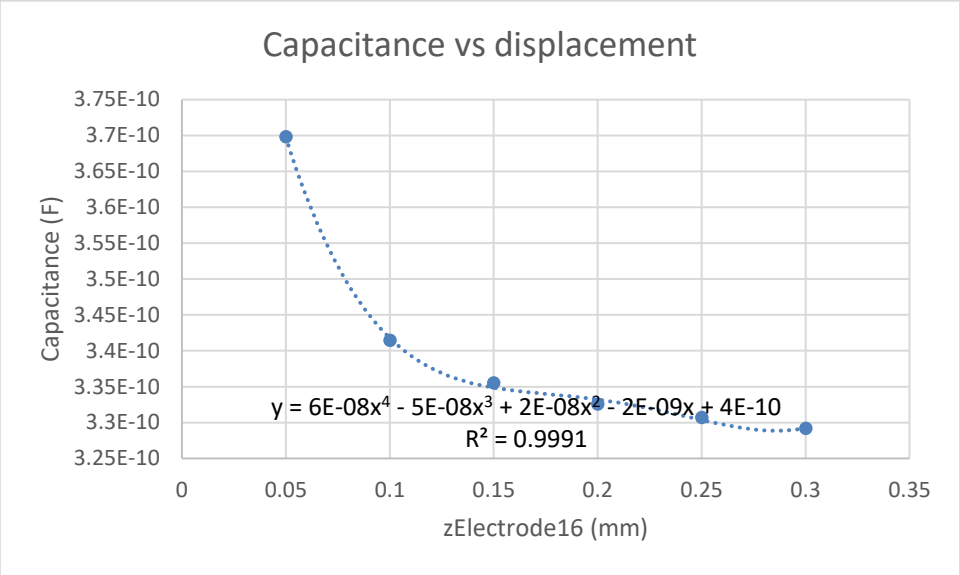


Figure 4.24. Curve of capacitance in relation to displacement for segmented array with thinned dielectric and electrodes.

Table 14. Sensitivity in relation to displacement in segmented array with thinned out dielectric and electrodes for a spherical load.

zElectrode16	Sensitivity (N.)
0.3	0
0.25	0.091
0.2	0.102
0.15	0.128
0.1	0.186
0.05	0.493

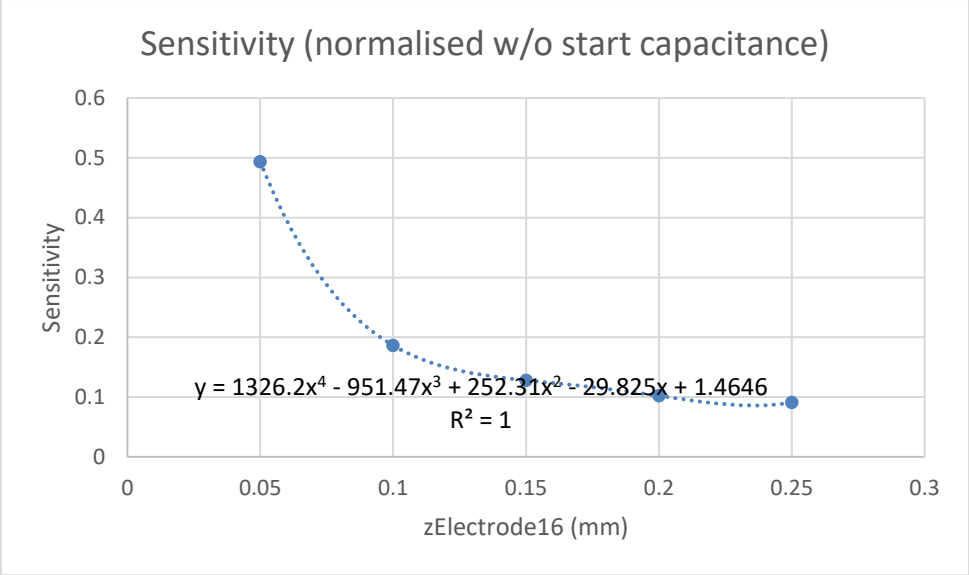


Figure 4.25. Curve of sensitivity in relation to displacement.

4.4 Conclusion

The simulations confirmed the relationship between capacitance and pressure proposed by the literature. The software CST's modelling suite also helped in deciding the array's geometrical features and mechanical design. From the simulations, it was established that the quantity of largest interest would be the sensor's sensitivity. The clearer establishment of the methodology also simplified the workflow, allowing to reduce the number of calculations. Different design characteristics were added until the results were deemed satisfactory – all in line with the top-down approach previously described during the methodological analysis discussed during Chapter 3.

With this knowledge, it was possible to test the simulation results in real life. Multiple sensor arrays based on the same fundamental design were tested by measuring the changes in capacitance of individual sensing units through an LCR meter. Later simulations also encompassed tests performed on different loading profiles, such as spherical, conical, or toroidal, each of which manifested different results. The data retrieved was sufficient to construct a model to use as a reference during real-life tests.

Chapter 5
Experiments

This section discusses and compares the results of the simulation and contrasts them with real-life test results. The observations made during these tests helped to produce mathematical models through comparisons of the empirical data to simulations and literature research. Several array prototypes were manufactured with a variety of materials and methods for the purpose of comparison.

Furthermore, preliminary studies into a readout circuit were conducted. A PCB was designed and components were selected, comprised of two multiplexers for signal encoding and a microcontroller to process and transmit the signal through an antenna.

5.1 Electrode design

A custom component footprint for Autodesk Fusion 360 was prepared, encompassing a single sensing unit of the dimensions described in section 3.1.1. The initial version used a simple square box with surface-mount pads on either side: one for the driving lines, located on the bottom of the circuit board (shown in blue in Figure 3.10), and one for the sensing lines, located on the top of the circuit board (shown in red in Figure 5.1). This footprint was revised twice (Figure 5.2), with the second revision (Figure 5.2C) being used as a reference for the final object. Both footprints were electronically modelled as variable capacitors. All the driving and sensing pads connected through the same method discussed in sections 2.2.3 and 3.1.1. The driving and sensing lines were fed into two Texas Instruments TMUX1208 8 in 1 out multiplexers. Custom footprints for the MUXs were also drawn in the circuit design.

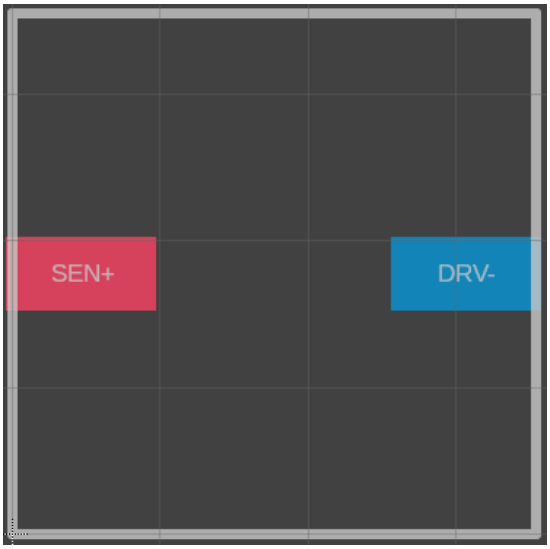


Figure 5.1. Initial form of the sensing unit footprint. The sensing pin, highlighted in red, is on the top layer of the circuit board; the driving pin, highlighted in blue, is on the bottom layer of the circuit board.

It is important to note that by its nature as a flexible circuit, the sensor array is incompatible with pad-through-hole designs, as these would suffer extensive bending and risk damage. No-leads and quad-flat IC surface-mount packages were used in the design process instead; this influenced the choice of MUX, microcontroller, and oscillator. The first manufacturing tests of the sensor prototype relied on models developed through EAGLE. These went through three revisions (Figure 5.2)

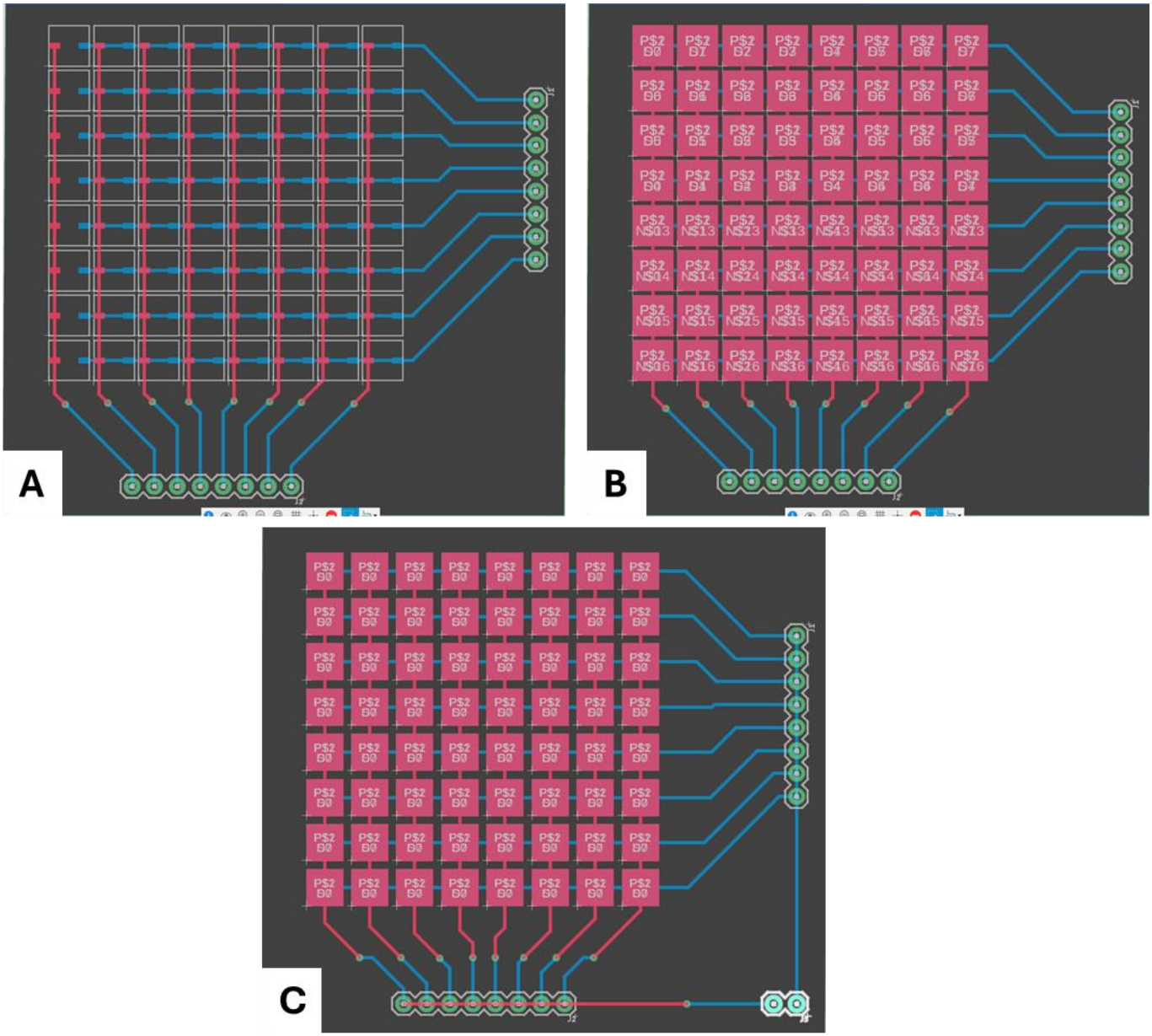


Figure 5.2. Various Revisions of Capacitive Sensor Array on EAGLE. (A) Revision 1 model. (B) Revision 2 model. (C) Revision 3 model. The top layer of the circuit is shown in red; the bottom layer is shown in blue.

However, this design was later modified to ensure that the output of individual sensing units could be measured independently, which, as discussed in section 2.2.3, is a crucial element of sensor arrays. The final design is shown in Figure 5.3.

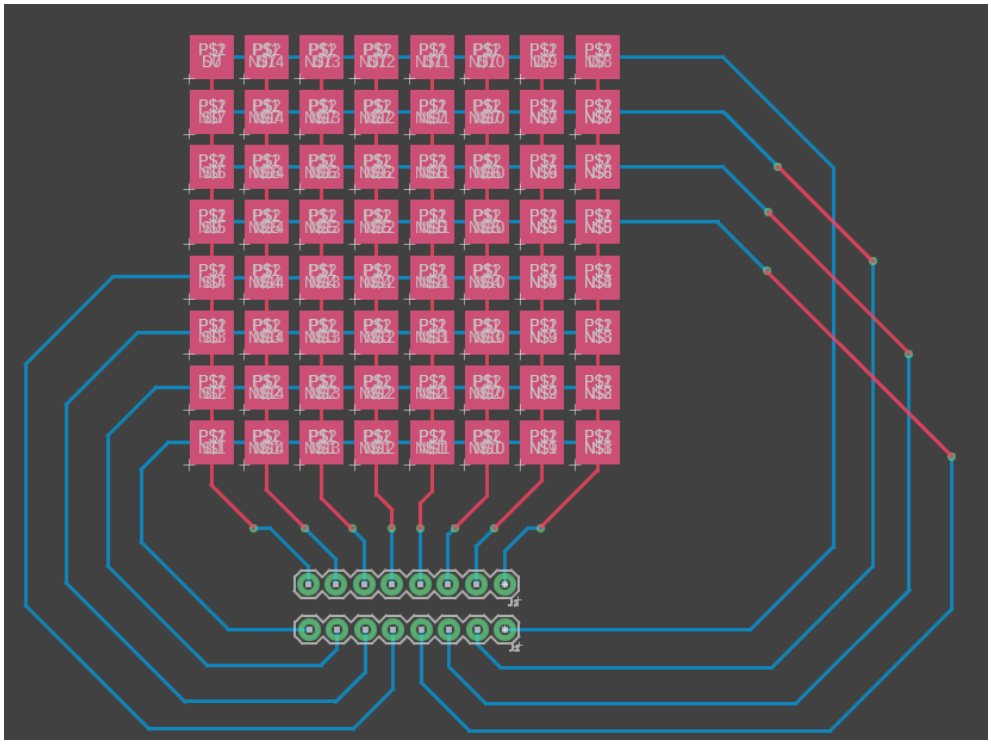


Figure 5.3. Final sensor array design in EAGLE. The top layer of the circuit is shown in red; the bottom layer is shown in blue.

5.2 Manufacturing tests

The prototypes were manufactured based on three Gerber (.GBR) files exported from CST Studio Suite. The files contained data that encoded the top layer electrodes, the dielectric, and the bottom layer electrodes. Autodesk Fusion 360, which provided the design of the circuit, does not accept external .GBR files as a source, meaning that the sensing units' footprint had to be recreated following the information from the CST simulations. The original .GBR files still served as a verification measure through the ViewMate software. The earliest runs (Figure 5.4), printed as tests to ensure the process was feasible for the current research, were manufactured through photolithography in a clean room, using the polyamide-based Mylar as a stand-in for the silicone dielectric employed in the simulations. Copper was used for the electrodes, as it is the material used by CST to model PECs for mechanical test purposes. Two sensor array test models were prepared. The first (shown in Figure 5.4A), based on the design in Figure 5.3B, accurately represented the connections between rows and columns. In the second (shown in Figure 5.4B), which followed the design shown in Figure 5.2C, all rows and all columns were connected as if they were a single unit instead. The output of the second array design fed into a 2x1 connector used as a testing point for

an LCR probe. This decision served to facilitate testing, as it would provide an average of the readings from each sensing unit, useful in the modelling of the sensors.

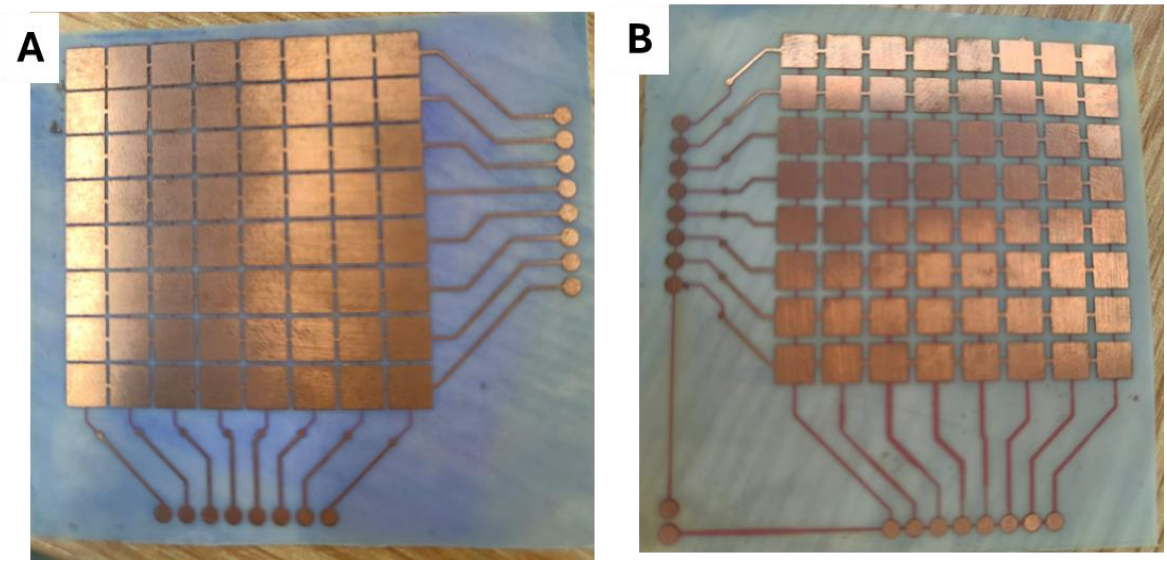


Figure 5.4. Manufactured electrodes for sensor validation. (A) Final test etched prototype. (B) Test prototype connected as a single unit (revision 1).

After testing the manufacturing prototype and modelling its properties, the final sensor was fabricated through photolithography on single-sided Mylar with copper foil on top. The electrodes in this run would be printed separately, their Gerber file extracted directly from CST instead of having to create a custom footprint in EAGLE to later be exported as a. GBR. This led to the advantage of making the electrodes closer to the dimensions they had during the simulations.

The main error source during the measurement stemmed from the interactions between the electrical fields projected across multiple units. These, in this iteration of the sensor, connected and fed into contacts to which the probe also connected. Because of this, the fields interact with each other. These interactions give way to crosstalk, which produces noise in the sensor. For this reason, a second circuit whose design was based on the schematic shown in Figure 5.2, was prepared. In the new circuit design, the electrical leads were close to each other to simplify measurement with the probe. The result is shown in Figure 5.5. Furthermore, to limit external sources of interference on the readings, a foil of Kapton tape shielded the electrodes (Wang, Zhong, Sun, & Li, 2014).

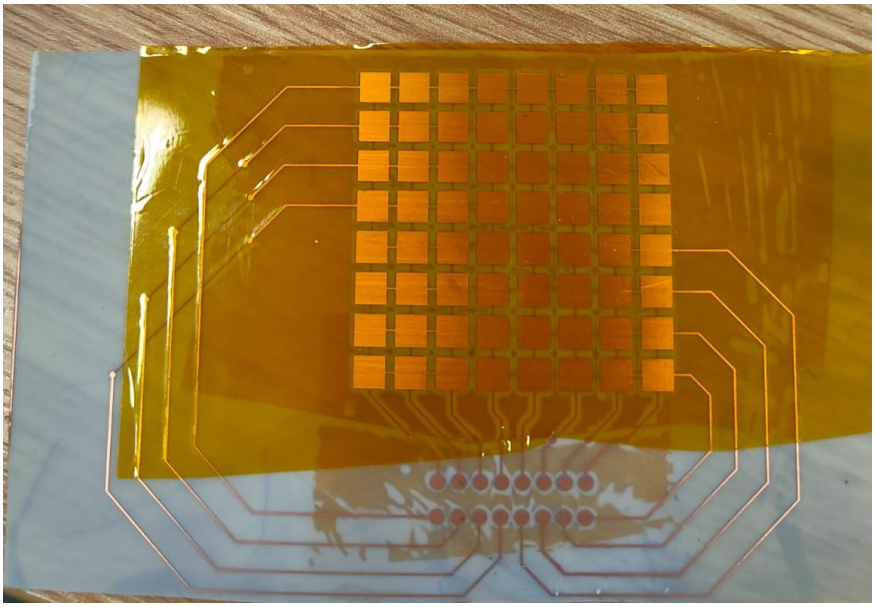


Figure 5.5. Copper etched version of the third sensor array circuit, integrating elements of the first two designs. The measurement points are independent for each sensing unit and aligned to simplify measurement.

5.2.1 Test object manufacturing

Two prototypes of the final sensor described in section 5.2 were built. The sensing units and tracks on both sides were made of single-sided Mylar with a 35 μm-thick layer of copper above it. Instead of replicating the component footprint through EAGLE, both the sensing (Figure 5.6A) and driving (Figure 5.6B) layers were taken out of the main CST simulation file and saved as their own models, each of which was exported as a .GBR file independently of the other. The tracks were drawn as 3D models connected directly to the respective driving or sensing line and added together using the software's Boolean Addition tool. The same procedure took place on the electrode rows and columns themselves.

A sheet of resin with dimensions 36.5 mm x 36.5 mm x 0.3 mm was 3D-printed for use as the dielectric layer used throughout all testing. The dielectric layer laid between the driving and sensing layers. Three versions of the sheet were printed with thicknesses varying between 0.3 and 0.5 mm, but only the 0.3 mm version operated during testing to ensure consistency with the simulations.

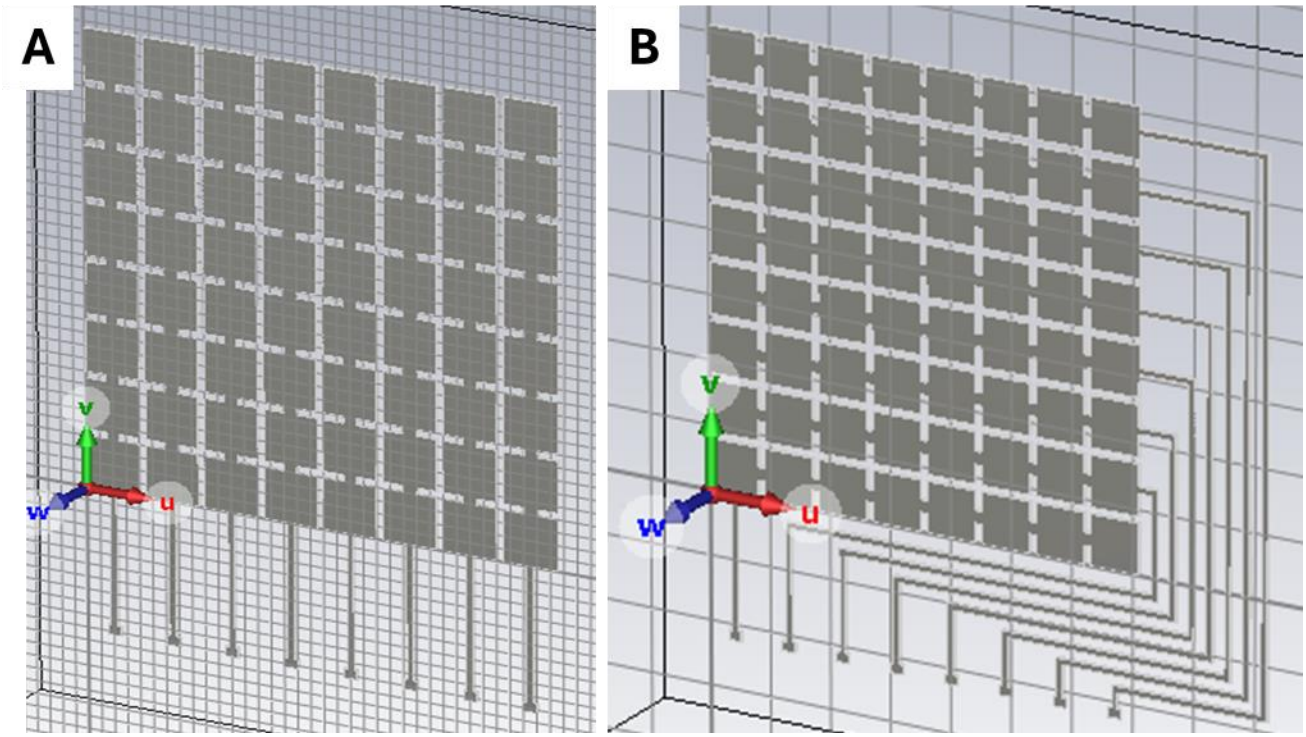


Figure 5.6. (A) Model of sensing electrodes to manufacture. (B) Model of driving electrodes to manufacture.

This variant of the prototype was manufactured by etching the copper tracks and electrodes onto the Mylar in a photolithography process, wherein UV light is shone through the objects to manufacture the PCB substrate, the electrodes and tracks. The process is stackable by adding more layers separated by photomasks. Manufacturing errors can occur, as the U.V. light behaves as a point source of light emanating from a pinhole and as such suffers scattering effects.

A further prototype was manufactured additively in a Voltera NOVA circuit printer. The electrodes used silver conductive ink instead of copper; the entire structure rested on a thermoplastic polyurethane (TPU) substrate. Additive manufacturing techniques are best suited to print small objects, as the primary constraint lies in the size of the ink nozzle instead of the object. However, error sources exist within additive manufacturing equipment as well: when the sensors controlling the pressure output by the ink dispenser are not calibrated properly or the dispenser nozzle is too small, the ink can exit the nozzle at a high enough velocity to produce turbulence, which is characterised as printing noise.

The machine used, the NOVA, has a print resolution in the μm range (2.5 x 7 x 1.25 μm) and the ink dispenser is automated, controlled by an image processor with a resolution of 1.7 μm/pixel (Voltera, s.d.), further simplifying the procedure. The control software issues commands to the printer and decodes geometries exported from other software in a variety of formats, including Gerber. During later stages of development, however, a series of mechanic and electronic failures of the machine

(unrelated to the current research) forced the use of an older printer model, the Voltera V-One (Voltera, 2024).

The NOVA printed a version of the system made of conductive silver ink on a thermoplastic polyurethane (TPU) substrate. Figure 5.6 shows the final photolithography copper prototype used during the core testing; Figure 5.7 also shows one of the inkjet printing prototypes undergoing manufacturing.

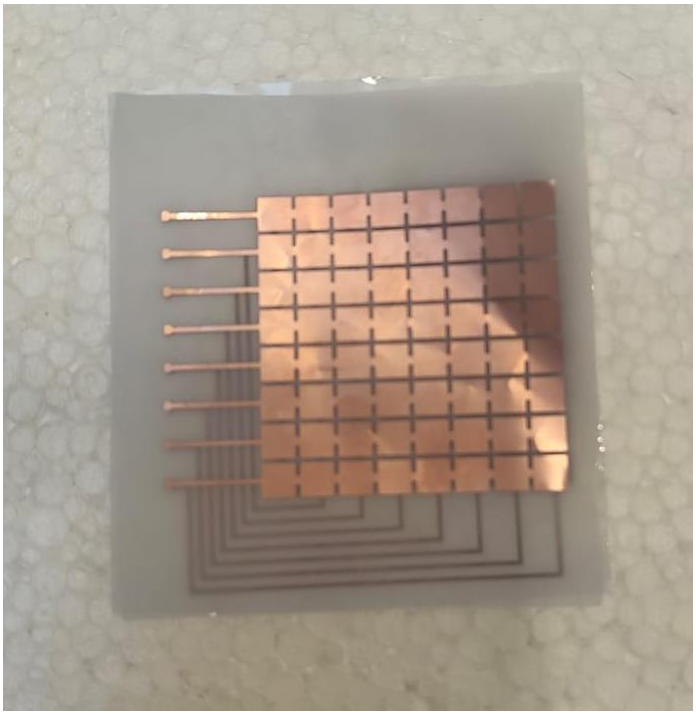


Figure 5.6. Sensor manufactured through photolithography.

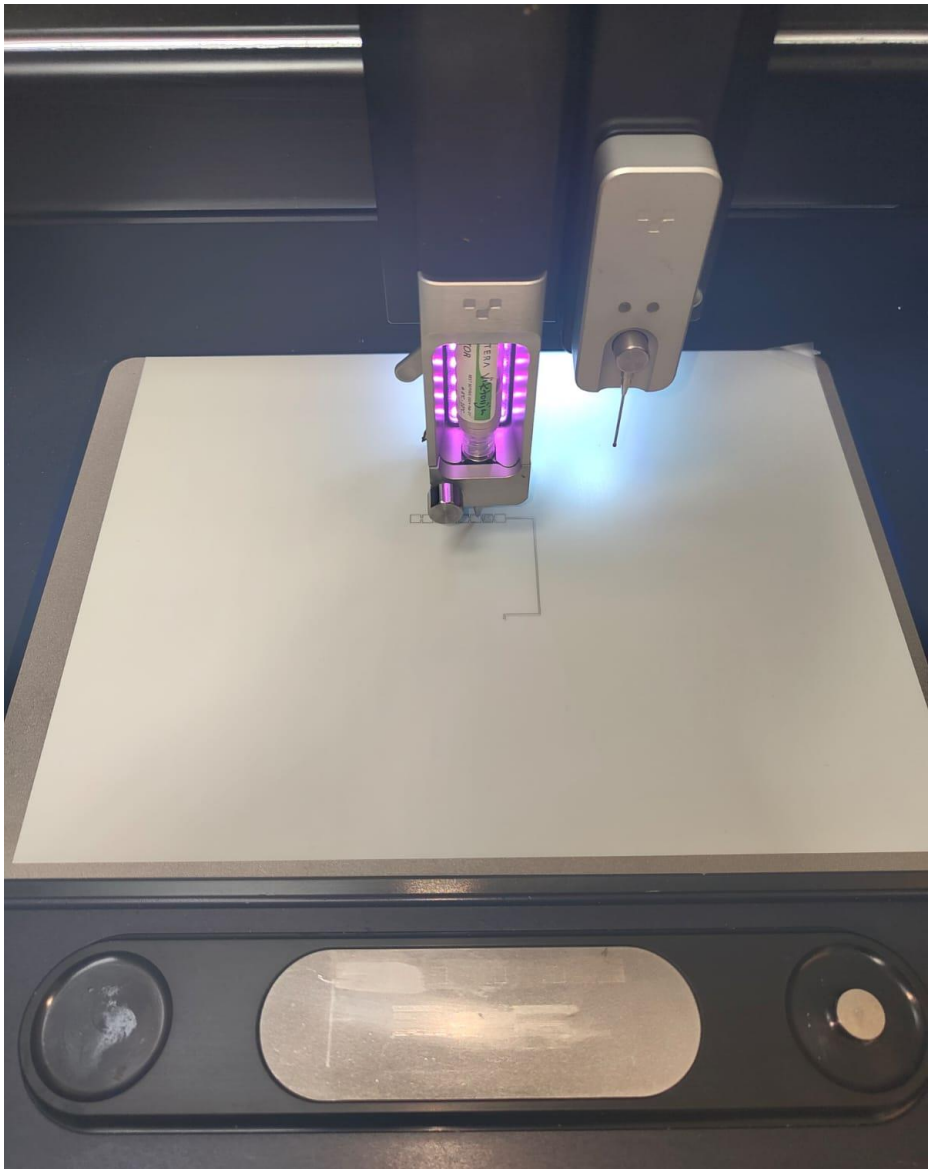


Figure 5.7. Second prototype of sensor undergoing manufacturing.

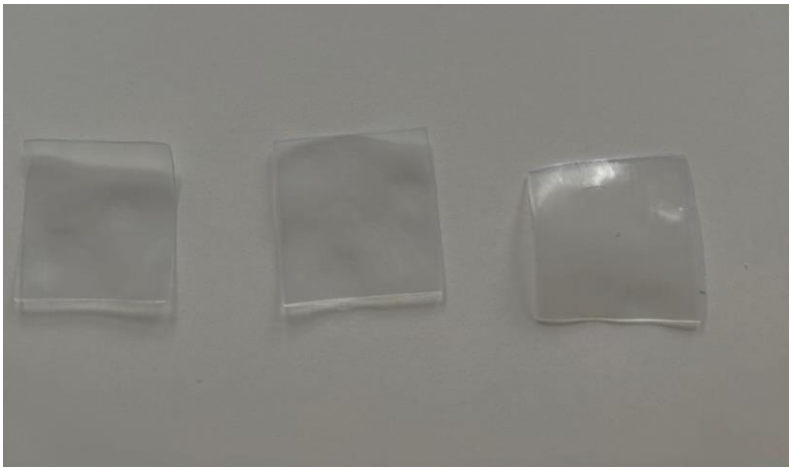


Figure 5.8. Dielectric 3D printed resin sheets.

5.3 Prototype testing

Early tests were conducted with a double-sided Mylar dielectric, the same used to produce the manufacturing test prototypes that were shown in section 3.2.2. These tests were considered not repeatable and manifested excessive noise, attributed to an improper selection of materials that was remedied during subsequent testing. Consequently, these tests did not produce reliable evidence of the sensor's operation and were excluded from further results, requiring a further batch of tests. A new prototype employed copper foil for electrodes on a thin single-sided Mylar substrate.

The driving and sensing electrodes were printed separately, after employing CST to reproduce the electrical contacts used in EAGLE as measuring points. The respective 3D models were exported as Gerber files directly from CST, and between the two lay the bespoke resin dielectric described in section 5.2. Otherwise, the setup remained the same as the previous measurements, described in section 5.2. Each weighted bead used in the experiment had a mass of approximately 2 g, as did the container. Six tests occurred, with the results shown in Table 25 and 26, as well as Figures 5.1 and 5.2.

Table 15. Capacitance change with respect to number of weights.

Weights	Capacitance (pF)
0	3
1	3.05
2	3.11
3	3.18
4	3.28
5	3.38
6	3.5

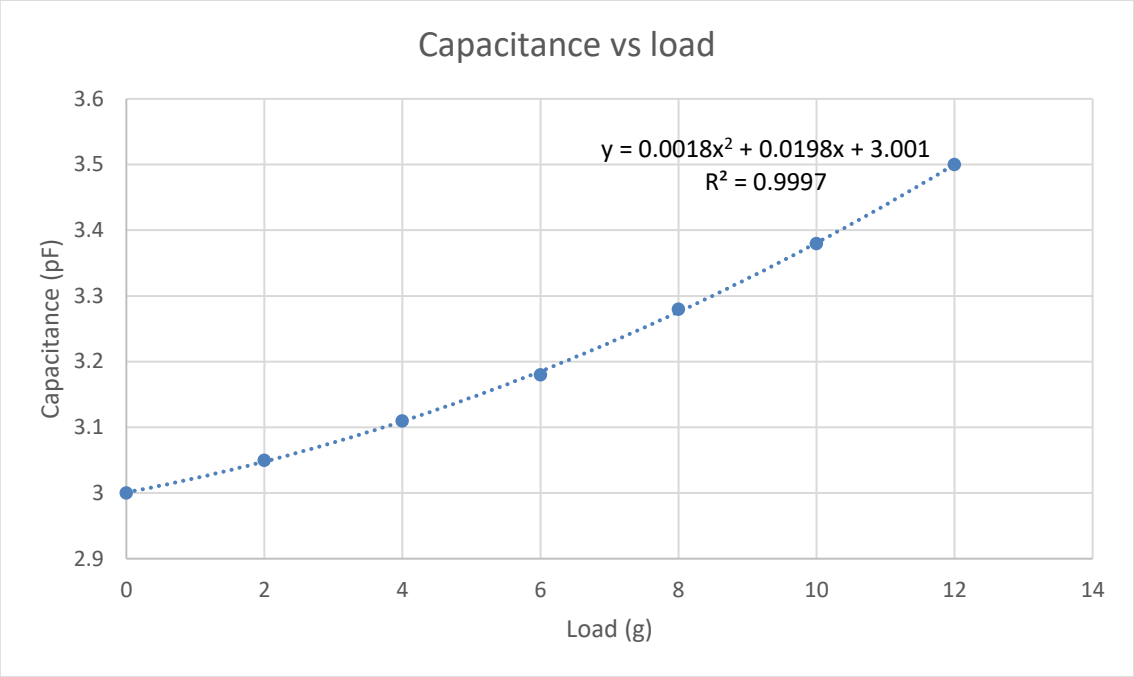


Figure 5.1. Curve of capacitance change in response to applied weight.

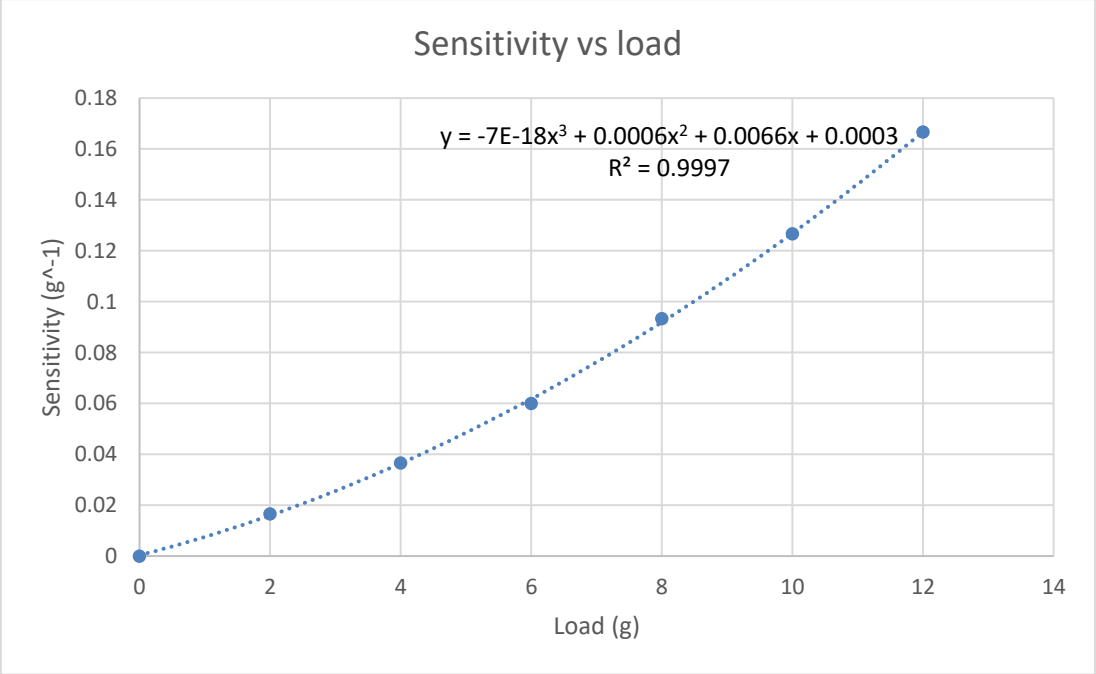


Figure 5.2. Sensitivity in relation to load.

The behaviour of the function governing capacitance and load mass obeys an exponential relationship. When viewed under the framework set in section 2.2.2 through Equation (2-12), this result provides evidence that the proposed sensor array obeys and replicates the mathematical model described in the literature. After this first test, a second test proved the repeatability of these measurements.

However, problems arise when attempting to link the experimental result to the simulations directly. To understand the reason behind this, it is necessary to return to the simulations and the way they were conducted. In the simulations, the displacements tested for changes in capacitance were in the order of magnitude of hundreds of μm, which, when put in Equation (2-12), produce the results seen in Figure 5.3.

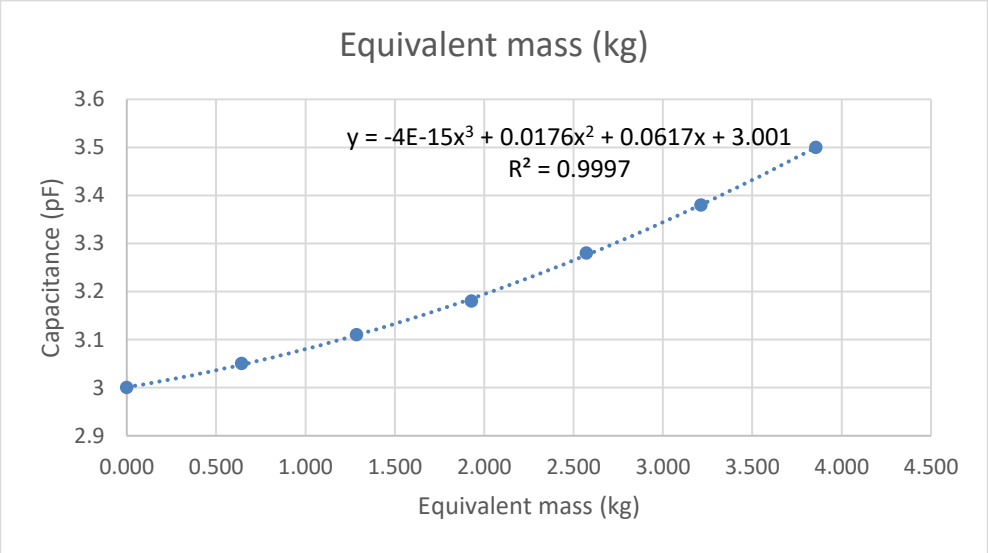


Figure 5.3. Curve of capacitance with respect to the equivalent mass required to produce the displacements tested during the simulations.

These mass values are infinitely large compared to those involved in the measuring setup used to test the sensor and show the limitations of the former: although mass relates to pressure, the only force acting on the object is the gravitational force, as equation (2-12) shows. When calculated as a function of mass, pressure is expressed as a ratio of the object's elasticity, a very large value (generally oscillating between MPa/m and GPa/m for commonly used materials; an example is the difference between the Mylar and silicone used in the real tests and the simulations respectively).

Further evidence of the results obtained and discussed insofar comes from the sensitivity calculations. Considering the observations made during this run of experiments, exemplified by the curve showed in Figure 5.3, the sensitivity was calculated using mass instead of displacement. The formulae used during the calculations remained the same as the ones described in sections 3.1.1 and 3.2.3 through equations (3-2) and (3-3). Table 26 shows the results, which are in line with the literature after accounting for this setup-specific characteristic.

Table 16. Table of sensitivity in relation to weight.

Weight (g)	Sensitivity	Sensitivity (%)
0	0	0

2	0.017	1.667
4	0.037	3.667
6	0.060	6.000
8	0.093	9.333
10	0.127	12.667
12	0.167	16.667

These data were used as a basis to calculate the mass equivalent to the simulated displacements (hereafter m_S, simulated mass) and respective pressure (hereafter P_S, simulated pressure) using equation (2-12). Table 17 shows the results, where it is clearly shown that the pressure required to produce the same results as the simulations is much greater than the one exerted by the weights used during these tests – a limitation of the experimental setup.

Table 17. Calculated mass and pressure equivalent to simulated displacements.

Simulated displacement (mm)	Equivalent mass (kg)	Equiv. pressure (MPa)
0	0	0
0.05	0.643	49.235
0.1	1.285	98.469
0.15	1.928	147.704
0.2	2.571	196.939
0.25	3.213	246.173
0.3	3.856	295.408

For this reason, mechanical sensors such as the one in (Dahiya, Ozioko, & Kumaresan, 2021) employ a different measuring setup based on cyclic loading, which makes use of specialised equipment unavailable during this project. This testing equipment makes use of load cells as mechanical actuators, capable of delivering forces within the kN range (VJ Tech, 2019) (Cosentino, Ferro, Restuccia, & Luciana, 2020). Additionally, these may control the number of cycles within which the force is applied: i.e. the signal frequency, which was established to be an important part of the transduction process through (2-3), (2-5) and (2-12). When accounting for the surface area covered by the electrodes tested for during the sensing (196 mm^2), using the 50 kN value as a reference (Cosentino, Ferro, Restuccia, & Luciana, 2020) produces a pressure of 255.1 MPa.

Any measurement conducted in such a setup would be inherently more repeatable at a qualitative and quantitative level, as it reduces the likelihood of human error and makes it possible to conduct measurements on an arbitrary pressure. During the present experiment, where such a setup was not available, measuring the pressure could not be possible. Instead, the measurements had to be performed on the mass, later converted to pressure by solving Equation (2-12).

Further proof of this can be seen in the displacements produced by the loads employed in the current testing setup, calculated from the capacitance readings with equation (2-12) and shown in Table 18.

Table 18. Calculated displacement produced by loads.

Load (g)	Displacement (m)
0	0
2	1.56E-07
4	3.11E-07
6	4.67E-07
8	6.22E-07
10	7.78E-07
12	9.34E-07

Here the displacement values are in the nm to μm range, well below the values tested for during the simulations.

These weight values are also well below the range of weight for the humerus, whose mass ranges between 110 and 120 g (Kabakci, Büyükmumcu, Cicekcibasi, & al., 2017). The possibility of using a cyclical loading machine for testing was investigated but found out to be unfeasible, as the necessary equipment was not available.

The prototype was validated again, this time using the shoulder joint model manufactured as explained in section 3.1.3. A new measuring setup was prepared such that a clamp would hold the LCR meter probes in place while the glenoid fossa laid on top of the driving layer. This way, the possibility and impact of baseline wander would be minimal, as described in section 3.2.3. Three separate measurements were conducted to verify the repeatability of the sensor readings. These produced a hysteresis between 0.001 and 0.005, for a standard deviation between 0.995 and 0.999 (approx. 1). Three readings were taken: one with an empty array (i.e.: complete loosening), one with a loose humeral head held in place and a last one with the humeral head pressed into the glenoid fossa. These results appear in Table 19.

Table 19. Capacitance readings for humeral head test.

Load (g)	Capacitance w/Humerus (pF)
26	2.77
40	3.2
1000	3.7

In the absence of a means of controlling the force acting on the sensing units, the larger loads were applied using a weight scale to determine the force with respect to the mass. As such, these values are approximations and do not provide an accurate reading of the capacitance change with respect to the loading, as was done in previous tests. As it can be seen, the addition of the humerus helps increase the system's sensitivity, producing a capacitance change of around 0.5 pF, which resulted in a change between 15 and 18%, calculated using equation (3-2) and displayed in Table 20 (where they are labelled as "Capacitance Ratio" to distinguish them from the sensitivity calculated during previous simulation runs). This is considered in line with the literature, while also proving the repeatability of the numerical model tested and validated up to this point.

Table 20. Sensitivity of tests with shoulder model.

Model state	Capacitance Ratio (hum.)
No pressure applied	0
Basic glenoid	0.155
Full pressure applied	0.181

Displacement tests were also performed by moving the glenoid across different electrodes, using the same methodology as the test described above. Electrode (3; 3) was used during the testing; the displacement brought the humeral head close to electrodes (4; 3) and (2; 3). The tests showed a consistent performance, although a 0.1 pF error appeared in electrode (2; 3). After observing the model, it became clear that this was the result of a measuring artefact produced by the irregular shape of the bone model.

Figure 5.4 shows that the humeral head is not perfectly round but instead presents grooves and spikes over its surface, as expected from human bone. One of these spikes is in proximity to where electrode (2; 3) was during the testing. In that location, a larger mass was concentrated, producing a larger displacement when compared to electrodes (3; 3) and (4; 3). Therefore, the tests returned a reading of 3.3 pF on electrode (2; 3) for a basic glenoid test as opposed to the 3.2 pF observed in the other test electrodes. This is a measuring artefact produced because of the model refinement process performed in Slicer, as the model used for reference was based on a true human CT scan.

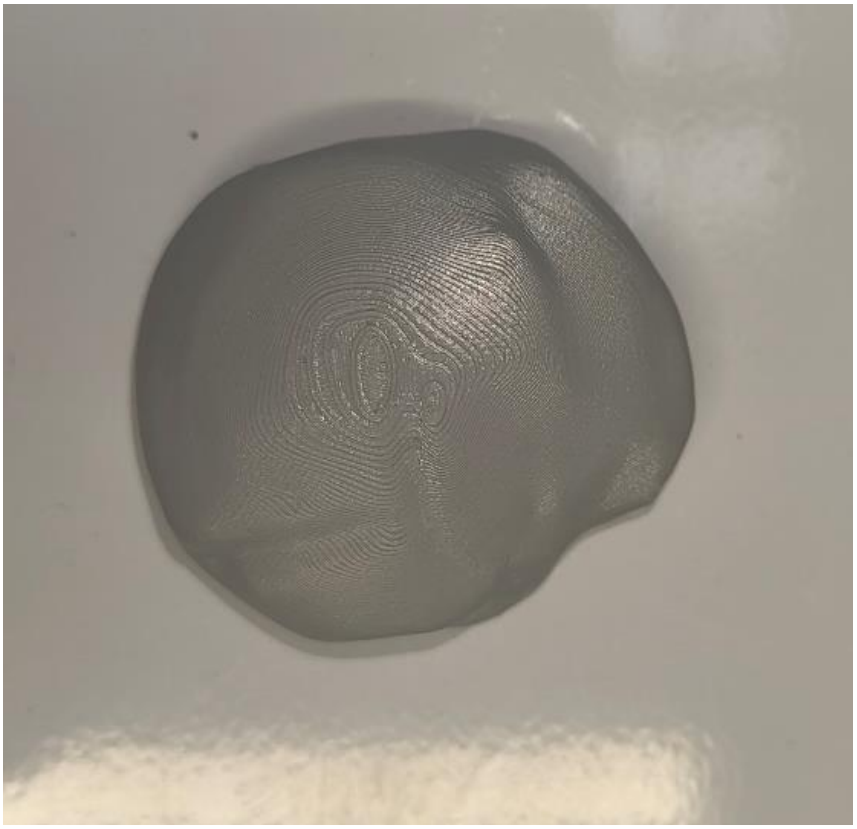


Figure 5.4. Humeral head top view showing the irregularities in the surface.

Testing of the additive conductive silver ink prototype used the same setup as the copper etched one. The alternate printer did not allow for conformal printing, and for this reason, both layers had to be printed separately, so the resin dielectric could not be used. The two layers were put one on top of the other instead. The TPU has a Young's modulus of 67 MPa (Ultimaker, 2022), much higher than the simulated silicone rubber. Such a change means that the dielectric deforms in a different way compared to the etched prototype, meaning that both the starting capacitance and the capacitance change were expected to be different, as exemplified by equation (2-5).

Two tests were performed, one via the weighted beads and one for the shoulder model. Both utilized a 1 kg load for comparison purposes. In addition to the weighted beads setup, a second test was performed with a load of approximately 0.5 kg. Table 21 shows the results; the capacitance ceiling (i.e.: the largest value measured) shown is much higher than the etched prototype, despite the instability of the sensor.

Table 21. Table of capacitance change and sensitivity in additive prototype.

Heavy weight (kg)	Capacitance (pF, silver)	Sensitivity (silver)

0.5	6	0
1	6.2	0.067

Nevertheless, due to the mechanical failure of the printer, care should be taken when discussing the properties of the silver-printed prototype. The measurements conducted on the silver-printed prototype were particularly noisy and not repeatable, meaning that any further developments would result in unreliable evidence. An analysis of the prototypes that had been discarded after these findings revealed that the printer used as a replacement for the NOVA was not suitable for the manufacturing of the present array, and any attempts to do so showed various defects responsible for the problems encountered during measurement.

5.1.1 Observations on printing

Although the etched prototype was successfully tested and proven to be repeatable, the Nova Voltera 3D printer produced the new copy of the sensor using the same basic design employed during the test. Because silicone resin - the material used for the dielectric during testing - is not suitable for inkjet printing, thermoplastic polyurethane (TPU) was used instead. Likewise copper, the material used for the electrodes, is rarely used in inkjet printing due to concerns over its oxidation under standard printing conditions, resulting in a change to conductive silver ink.

CST successfully exported the electrode blueprints a second time and sent them to a computer connected to the Voltera to control the printing. The printer control accepted the design, and the electrodes were successfully printed once. Later revisions, meant to ensure that the sensor could be tested under the same experimental setup used for previous sensors, were accepted into the printer control software all the same.

Due to unrelated mechanical failures in the 3D printer, an older printer model (V-One) was employed. However, it must be pointed out that Figure 5.7 in section 5.2.1 shows the design undergoing a manufacturing test, which conclusively proves the feasibility of the design.

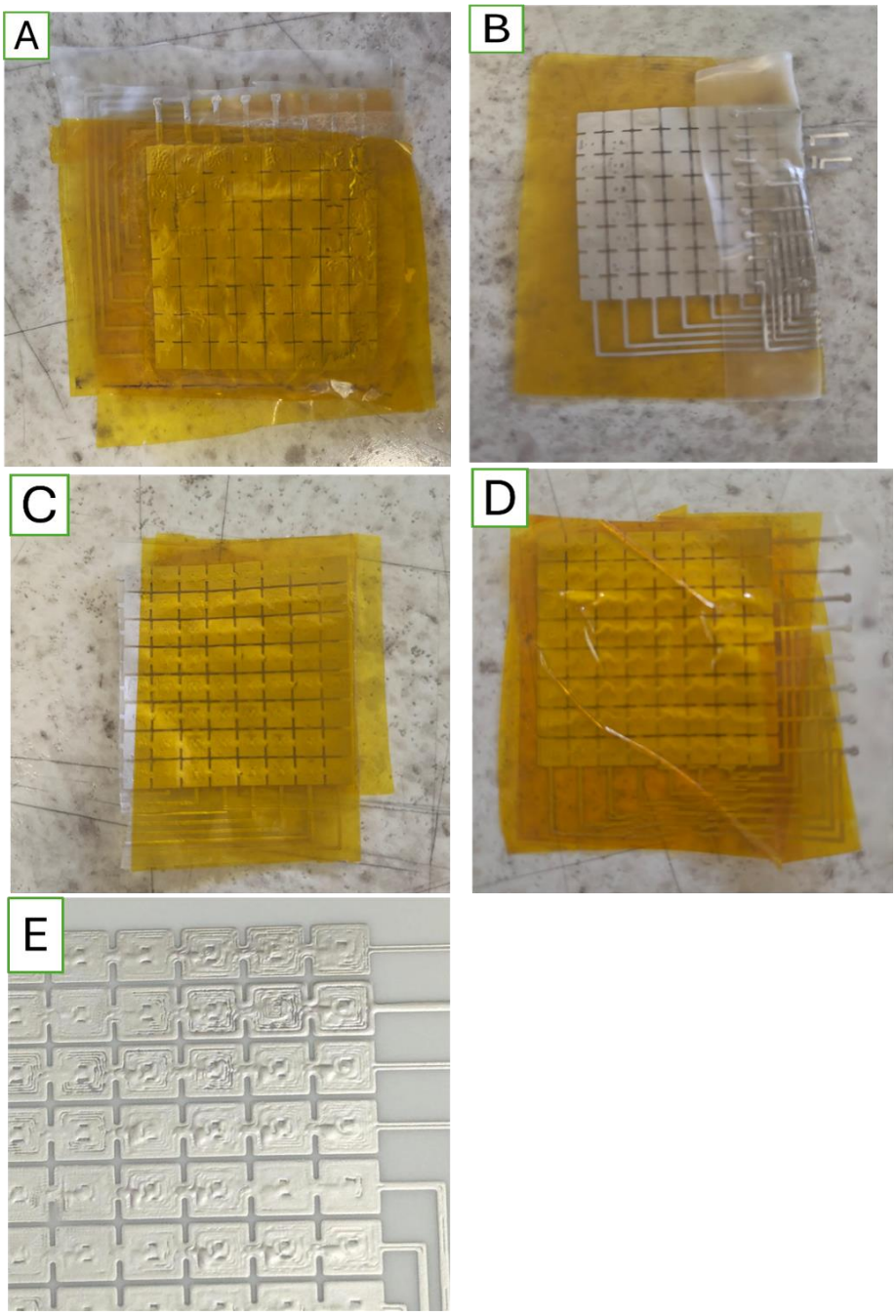


Figure 5.5. Conductive Ink printed sensors using the Voltera V-one. (A) Sensor array with TPU dielectric. (B) Sensor array with resin dielectric. (C) Sensor array with resin dielectric revised. (D) Sensor array with TPU dielectric revised. (E)Example of misprints when printing with conductive silver ink.

Various printing errors took place during the ink dispense process, with consequences on the sensor's performance. In different prints, some tracks connecting the electrodes on the same layer were not printed properly and either did not feed into each other, creating open circuits. Alternatively, different tracks that were meant to remain electrically separate came into contact due to ink drips and created short circuits.

All the misprints therefore caused a change to the track width and potentially the sensor surface area. Consequently, less charge moved across the medium, describing a loss of current in compliance with the law of flow continuity:

$$\Sigma_{n=1}^{\infty} Q_{\text{in}} = \Sigma_{n=1}^{\infty} Q_{out} \quad (5\text{-}1)$$

where Q_{in} is the input charge of a medium and Q_{out} is the output charge with respect to the same medium. Electrical charge, stored within the electrodes, is supposed to move across the conductive wires over time; considering these facts, it becomes clear that a change in electrical current or charge would have consequence on the capacitance readings. On these suspicions, measurement with a digital multimeter revealed that the current intensity was not constant across a layer, proving the presence of short circuits or open circuits.

5.2 Future applications in systems

During development, the integration of the proposed sensor into a readout circuit for practical applications was examined. Here is described the structure of the proposed readout circuit, transduction procedures, analog-digital conversion, and antenna communication. A block diagram (shown in Figure 5.6) was used to show how the sensor array may be integrated into a communication system.

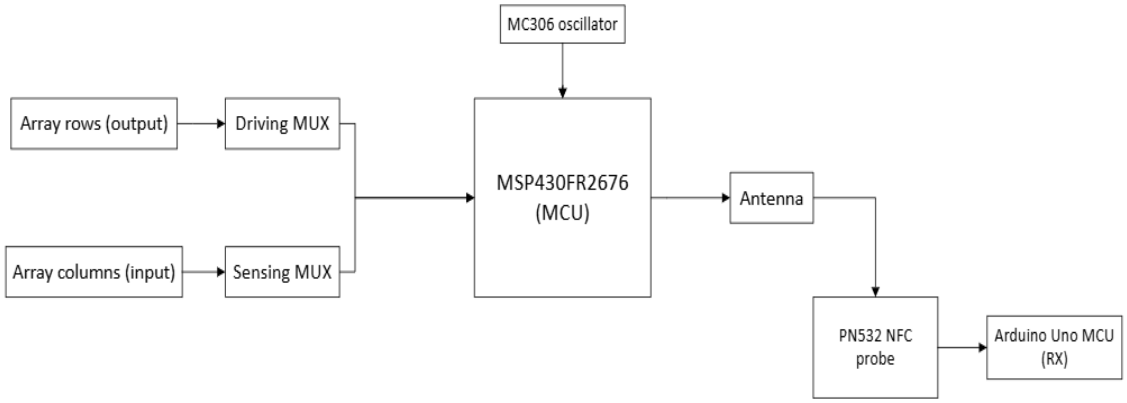


Figure 5.6. Readout circuit block diagram.

The rows and columns of the array feed through the MUXs, with each row and column processed separately. The MSP line of microcontrollers has pins for both positive and negative voltage references, which are used for sensing (array columns) and driving (array rows) respectively. An excitation voltage feeds through the driving electrodes periodically, while the sensing electrodes remain inert unless pressed on. As described in section 2.2, the output from each interpolates and is

what is stored in the microcontroller's memory. Each time a sensing unit is pressed, the voltage increases proportionally to the sensitivity; as such, the memory of the microcontroller should be chosen to accommodate the sensor's sensitivity. At a lower level, the block diagram develops into the PCB schematic showed in Figure 5.7.

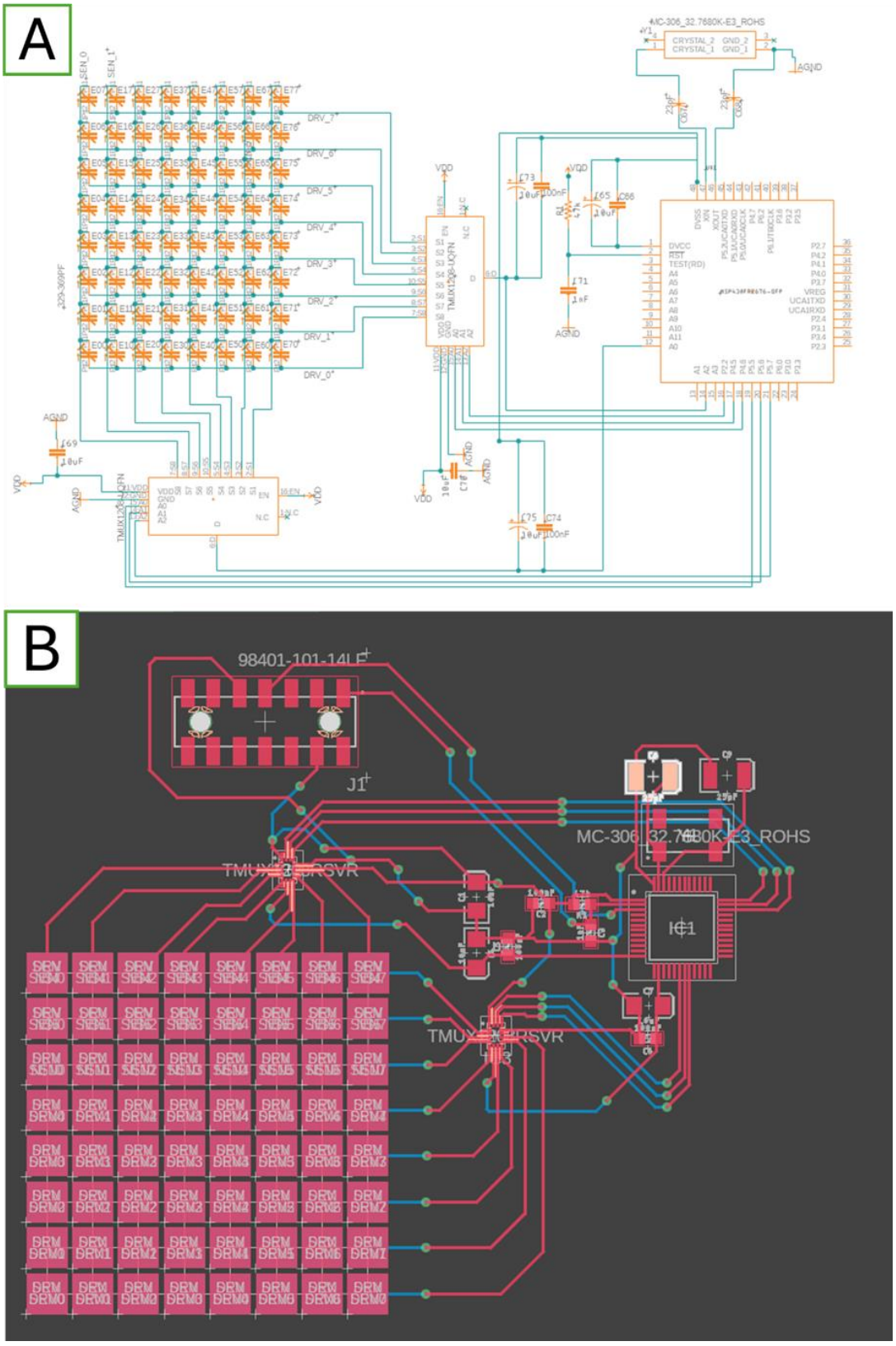


Figure 5.7. (A) Proposed readout circuit schematic. (B) Proposed readout circuit PCB layout.

5.3 Conclusion

The values obtained from the simulations do not fully match the sensor's performance in the real world; this holds true for any system tested in the same circumstances. A simulation occurs in an ideal environment, where multiple phenomena known to alter the readings of sensors never happen, thus necessitating real-life testing. Operations useful during simulations, such as a parameter sweep, require specialised testing setups that were not available during the experiments and required building workarounds into the present testing setup.

The first point of contention is in the very nature of the simulations conducted. These make use of 3D models, which the computer views as points in a coordinate system, whose values it assigns to a matrix. As such, it is perfectly possible for multiple points to share the same coordinate values on the x, y and z-axes, in which case they will appear as if they are "blending" together into one. This occurred in all tests because the method used during the simulations mimicked the act of pushing the sensing units together in response to external forces. Such a feature would not only never be possible in real life, but it can also be used in the simulation to produce extremely large displacements relative to the size of the object under test. These phenomena cannot verify in real life, a consequence of limitations imposed by the thickness and stiffness of the dielectric material, especially when considering the restrictions imposed by the present application. Consequently, the mathematical model employed for the simulation, while still useful, cannot be taken as it is and used to interpret the results.
This circumstance was worked around by exploiting the linear relationship between pressure and mass described in Section 2.2.2. Because the rate of change between these quantities is constant, it is plausible to say that they will have the same relationship with capacitance – a logarithmic relationship. This reasoning was considered plausible in light of the fact that the dielectric was a soft, plastic material, and as such would absorb exponentially any form of energy (in this, it shares the properties of a capacitor), mass being no exception.

Under this framework, despite difficulties inherent to the testing setup, the real-life tests successfully and repeatably validated the mathematical relationship between capacitance, displacement, mass and pressure observed during the simulation. Testing of multiple sensor array prototypes based on the design produced through simulations took place, encompassing a variety of dielectric materials and manufacturing arrangements. The printer control software accepted the design, which demonstrated that it was feasible for construction.

Chapter 6
General conclusions

This thesis presented a qualitative study about the development of a capacitive pressure array for use in intrabody physiological measurements, with an emphasis on shoulder joint loosening and implant integrity. The theoretical background of the project was researched and explained, with an emphasis on the interactions between the different fields involved. In fact, the research adopted an interdisciplinary approach, with particular care taken in the study and mathematical modelling of the interactions between the different fields and aspects of development.

This background provided a guideline to follow during the computer simulations conducted to investigate the function of the proposed sensor array, the subsequent real-life experiments and, later, the configuration of arrays and circuits. Aspects of mechanics of materials and electronics were examined in tandem to obtain a detailed understanding of the transduction of mechanical stress into electrical capacitance. This knowledge served to find a material that, when used as dielectric, translates the force exerted by a shoulder joint into a readable capacitive signal. It is possible to use these data as a basis to improve upon the existing design with the end goal of integrating it into a biomimetic wireless communication circuit for the monitoring of shoulder implant loosening.

The research questions and challenges mentioned in the introductory chapter of this thesis, concerning the electronic aspects of the problem, were compounded by complications within the present setup. A quantitative analysis was deemed unfeasible, restricting the scope of the research to a qualitative analysis. This analysis successfully answered the research questions by producing simulations that validated the existing models, connecting capacitance and pressure. These models were later used to build a setup in which to perform real-life tests. The experimental results could only be analysed in a preliminary capacity.

A consequence of limitations in the experiment setup was the prevention of further measurements that would allow a mixed-methods analysis of features such as repeatability and error. Mechanical failures in the manufacturing equipment aggrieved such difficulties, which prevented the analysis of a 3D printed prototype of the sensor – a key deliverable that would have further emphasised the novelty of the current research. However, enough evidence emerged to prove that additive manufacturing of the sensor array was possible, including the fact that the causes of the above-mentioned mechanical failures were unrelated to the current research project.

Lastly, this research deemed that the best way to carry out the analysis that validates existing models of capacitance change in relation to pressure is to perform measurements on a real-life prototype, due to challenges that quickly arose when conducting simulations. Although the simulations proved useful in validating the basic scientific principles underlying the research, studies concerned with more advanced aspects of development may be prone to errors, making them unreliable as evidence of the operation.

6.1 Future work

The focus on an interdisciplinary approach reveals that there are still different research avenues to pursue on this topic. Such further analysis would concern the electronic, clinical, and mechanical aspects of the design. This section is dedicated to describing the directions that further research building up on what was done during development can take, including applications and topics of consideration. The various aspects of development also interact with each other, and understanding the nature and causes of these interactions is essential to further developments, particularly as far as the readout circuit is concerned.

Because of the very nature of intrabody implant communication, tests conducted in the air must be complemented with experiments that make use of body phantoms to study the attenuation of human tissue and its influence on the signal, which would affect future considerations on the articulation of the front- and back-end of a readout circuit; in vivo tests should also be performed. Doing so requires the development of an ad-hoc solution to transmit power, culminating in the performance analysis of both the readout circuit and communication system.

It is established knowledge that characterising a link between the front- and back-end of an intrabody implant communication system is feasible; several applications, such as transcranial magnetic stimulation and wireless battery charging, have already been explored (Sharma & Kampianakis, 2016) (Tang, et al., 2006) within the field. Biosensing is an especially prominent area, with extensive literature that theorises the integration of biosensors within intrabody implant communication systems (Liu, Ogirala, Berger, & Mickle, 2011) (Lodato & Marrocco, 2015). The readout and communication circuit proposed for the sensor studied in the present thesis is no exception, though any further work in this regard requires building and testing a new batch of the readout circuit in air, to obtain a model to reference during phantom testing. Most importantly, successfully characterising a link between the intrabody environment and an external front-end would pave the way for the integration of the sensor array in existing body-area network designs, enabling real-time clinical monitoring.

In literature, biosensors testing often requires specialised cyclic loading test setups that assess the performance of the sensor under large loads. In these tests, the measurement repeatability is much easier to analyse than it was in the present experiment setup; additionally, the frequency may be used as a control parameter during these tests. In the case of the present sensor array, frequency response tests would yield information on the frequency ranges at which intrinsic measurement noise manifests. From this point, it would be possible to build a filter using these ranges as its stopband, enabling a clean readout of the sensor output. Frequency response also provides insight into the system's gain, allowing the construction of its transfer function, a key piece of information when studying the interactions between any two systems.

With the ability to read the sensor output, it is possible program the communication system front-end to display the results through a human interface device, making the space- and time-dependent features of the signal visible. Such a line of enquiry was pursued in the literature (Wang, Zhong, Sun, & Li, 2014) by encoding the output of different MUX channels to the grayscale values of pixels displayed on the screen of a PC connected to an FPGA-based readout circuit. Through this method, it is possible to create a "pressure map": a visual representation of different regions corresponding to the units in which external forces act upon the array.

In conclusion, the project successfully developed a flexible printed capacitive pressure-sensing array. The studies conducted through simulations and experiments offered insight into the principles and mathematical modelling of the transduction of mechanical energy into electrical signals, revealing the influence of the dielectric material on the sensor output. Through this knowledge it is possible to find materials that, when used as dielectric, translate the force exerted by a shoulder joint into a readable capacitive signal. It is possible to use this as a basis to improve upon the existing design with the end goal of integrating it into a biomimetic wireless communication circuit for the monitoring of shoulder implant loosening.

References

3D Slicer. (n.d.). *3D Slicer image computing platform*. (3D Slicer) Retrieved August 24, 2025, from https://www.slicer.org/

Barco, R., & Savvidou, O. J. (2017, March 13). Complications in reverse shoulder arthroplasty. *EFORT Open Reviews, 3*(1), 72-80. doi:https://doi.org/10.1302/2058-5241.1.160003

Becker, H. (1965, March). Elastic modulus of Mylar sheet. *Journal of Applied Polymer Science*, 911-916. doi:https://doi.org/10.1002/app.1965.070090309

Bevelacqua, P. J. (2021). *Antenna Theory - Frequency Bands*. Retrieved August 4, 2025, from Antenna Theory: https://www.antenna-theory.com/basics/freqBands.php

Bevelaqua, P. J. (2009). *Antenna Theory - Admittance Smith Chart*. Retrieved August 23, 2025, from Antenna Theory: https://www.antenna-theory.com/tutorial/smith/smithchart7.php

Bevelaqua, P. J. (2009). *Antenna Theory - Directivity*. Retrieved August 23, 2025, from Antenna Theory: https://www.antenna-theory.com/basics/directivity.php

Bevelaqua, P. J. (2009). *Antenna Theory - Smith Charts*. Retrieved August 23, 2025, from Antenna Theory: https://www.antenna-theory.com/tutorial/smith/smithchart3.php

Bevelaqua, P. J. (2009). *Antenna Theory - Smith Charts*. Retrieved August 23, 2025, from Antenna Theory: https://www.antenna-theory.com/tutorial/smith/smithchart3.php

Bishop, W. (2025). 4.1: Euclidean Geometry. In *Modern Geometry.* Los Angeles: California State University. Retrieved August 23, 2025, from https://math.libretexts.org/Bookshelves/Geometry/Modern_Geometry_(Bishop)/04%3A_Elementary_Euclidean_Geometry/4.01%3A_Euclidean_Geometry

Bocan, K. N., Mickle, M. H., & Sejdić, E. (2017, September 1). Multi-Disciplinary Challenges in Tissue Modeling for Wireless Electromagnetic Powering: A Review. *IEEE Sensors Journal, 17*(20), 6498-6509. doi:https://doi.org/10.1109/JSEN.2017.2748338

Boileau, P., & Watkinson, D. J. (2005, 21 February). Grammont reverse prosthesis: Design, rationale, and biomechanics. *Journal of Shoulder and Elbow Surgery, 14*(1), 147-161. doi:https://doi.org/10.1016/j.jse.2004.10.006

Bryn, L. (n.d.). *Dielectric Properties*. (IT'IS Foundation) Retrieved August 23, 2025, from https://itis.swiss/virtual-population/tissue-properties/database/dielectric-properties/

Chasnov, J. R. (n.d.). 5.3: Heaviside and Dirac Delta Functions . In *Differential Equations.* Hong Kong: Hong Kong University of Science and Technology. Retrieved August 23, 2025, from https://math.libretexts.org/Bookshelves/Differential_Equations/Differential_Equations_(Chasnov)/05%3A_The_Laplace_Transform/5.03%3A_Heaviside_and_Dirac_Delta_Functions

Chen, S., Wu, R., Li, P., Li, Q., Gao, Y., Qian, B., & Xuan, F. (2018, October 4). Acid-Interface Engineering of Carbon Nanotube/Elastomers with Enhanced Sensitivity for Stretchable Strain

Sensors. *ACS Applied Materials & Interfaces, 10*(43), 37760–37766. doi:https://doi.org/10.1021/acsami.8b16591

Cheng, A. J. (2023). Recent Advances of Capacitive Sensors: Materials, Microstructure Designs, Applications and Opportunities. *Advanced Materials Technologies, 8*(11), 4-5.

Cheung, P. (2024, November 26). Analogue-to-Digital Conversion. London: Imperial College London. Retrieved August 23, 2025

Chowdhury, S., Marashdeh, Q. M., & Teixeira, F. L. (2016). Velocity Profiling of Multiphase Flows Using Capacitive Sensor Sensitivity Gradient. *IEEE Sensors Journal, 16*(23), 8365-8373.

Coates, E. (2020, December 29). *Learn About Electronics - The Impedance Triangle*. Retrieved August 28, 2025, from https://www.learnabout-electronics.org/ac_theory/impedance71.php

Cohen, D. J., Mitra, D., Peterson, K., & Maharbiz, M. M. (2012, March 12). A Highly Elastic, Capacitive Strain Gauge Based on Percolating Nanotube Networks. *Nano Letters, 12*(4), 1821–1825. doi:https://doi.org/10.1021/nl204052z

Corey, K. (2023, October 19). *Capacitive Touchscreen Sensor Analysis*. (Dassault Systémes) Retrieved August 23, 2025, from https://blog.3ds.com/brands/simulia/capacitive-touchscreen-sensor-analysis/

Cosentino, I., Ferro, G. A., Restuccia, & Luciana. (2020, May 22). An experimental set-up for cyclic loading of concrete. *Procedia Structural Integrity, 25*, 413-419. doi:https://doi.org/10.1016/j.prostr.2020.04.046

Crile, G. W., Hosmer, H. R., & Rowland, A. P. (1921, November 14). The electrical conductivity of animal tissue under normal and pathological conditions. *American Journal of Physiology - Legacy Content, 60*(1), 59-106. doi:https://doi.org/10.1152/ajplegacy.1922.60.1.59

Dahiya, R., & Soni, M. (2019, February 7). Soft eSkin: distributed touch sensing with harmonized energy and computing. *Philosophical Transaction of the Royal Society A, 378*(2164). doi:https://doi.org/10.1098/rsta.2019.0156

Dahiya, R., Ozioko, O., & Kumaresan, Y. (2021, January 28). Multifunctional Electronic Skin With a Stack of Temperature and Pressure Sensor Arrays. *IEEE Sensors Journal, 21*(23), 26243-26251. doi:https://doi.org/10.1109/JSEN.2021.3055458

F, H. (2011). 1.13 - Noble Metal Nanoparticles: Synthesis and Optical Properties. In *Comprehensive Nanoscience and Technology* (Vol. 1). Academic Press. doi:https://doi.org/10.1016/B978-0-12-374396-1.00034-9

Fares, H., Seminara, L., & Pinna, L. e. (2018). Screen Printed Tactile Sensing Arrays for Prosthetic Applications. *IEEE International Symposium on Circuits and Systems (ISCAS)* (pp. 1-4). Florence: IEEE. doi:https://doi.org/10.1109/ISCAS.2018.8351892

Feldman, J., Rechnitzer, A., & Yeager, E. (2025). 1.1: Definition of the Integral. In *CLP-2 Integral Calculus.* University of British Columbia. Retrieved August 23, 2025, from

https://math.libretexts.org/Bookshelves/Calculus/CLP-2_Integral_Calculus_(Feldman_Rechnitzer_and_Yeager)/01%3A_Integration/1.01%3A_Definition_of_the_Integral

Feng, L., Li, S., & Feng, S. (2017, February). Preparation and characterization of silicone rubber with high modulus via tension spring-type crosslinking. *Royal Society of Chemistry Advances, 7*(22), 13130-13137. doi:http://dx.doi.org/10.1039/C7RA00293A

Fiore, J. M. (n.d.). 4.6: Maximum Power Transfer Theorem. In *Introduction to Circuit Analysis.* Mohawk Valley Community College. Retrieved from https://eng.libretexts.org/Workbench/Introduction_to_Circuit_Analysis/04%3A_Analysis_Theorems_and_Techniques/4.06%3A_Maximum_Power_Transfer_Theorem

Flowers, P., Theopold, K., Langley, R., & Robinson, W. R. (2019). 10.2 Properties of Liquids. In *Chemistry 2e* (2 ed.). OpenStax. Retrieved August 23, 2025, from https://openstax.org/books/chemistry-2e/pages/10-2-properties-of-liquids

Frank, J. K., Siegert, P., & Plachel, F. e. (2022, March 10). The Evolution of Reverse Total Shoulder Arthroplasty—From the First Steps to Novel Implant Designs and Surgical Techniques. *Journal of Clinical Medicine, 6*(11), 1512. doi:https://doi.org/10.3390/jcm11061512

Gabriel, C., Gabriel, S., & Corthout, E. (1996). The dielectric properties of biological tissues: I. Literature survey. *Physics in Medicine and Biology, 41*(11). doi:10.1088/0031-9155/41/11/001

Gabriel, S., Gabriel, C., & Lau, R. (1996, April 2). The dielectric properties of biological tissues: III. Parametric models for the dielectric spectrum of tissues. *Physics in Medicine & Biology, 41*(11), 2271. doi:10.1088/0031-9155/41/11/003

Gabriel, S., Gabriel, C., & Lau, R. W. (1996). The dielectric properties of biological tissues: II. Measurements in the frequency range 10 Hz to 20 GHz. *Physics in Medicine & Biology, 41*(11), 2251. doi:10.1088/0031-9155/41/11/002

Garewal, D. (2019, January 30). *Reverse Shoulder Replacement*. (Melbourne Arm Clinic) Retrieved August 22, 2025, from https://melbournearmclinic.com/reverse-shoulder-replacement/

Gea-Banacloche, J. (2019). 10.1: The Inverse-Square Law. In *University Physics I - Classical Mechanics.* University of Arkansas. Retrieved August 23, 2025, from https://phys.libretexts.org/Bookshelves/University_Physics/University_Physics_I_-_Classical_Mechanics_(Gea-Banacloche)/10:_Gravity/10.01:_The_Inverse-Square_Law

Geselowitz, D. B. (1989, June 30). On the theory of the electrocardiogram. *Proceedings of the IEEE, 77*(6), 857-876. doi:https://doi.org/10.1109/5.29327

Hamilton, M. A., Wright, T. W., Roche, C., & Flurin, P. H. (2015). Effect of reverse shoulder design philosophy on muscle moment arms. *Journal of Orthopaedic Research, 33*(4), 605-613.

Hartman, G. e. (n.d.). An Introduction to Vectors. In *Calculus 3e (Apex).* Virginia Military Institute. Retrieved from

https://math.libretexts.org/Bookshelves/Calculus/Calculus_3e_(Apex)/10%3A_Vectors/10.02%3A_An_Introduction_to_Vectors

Hinrichs, R., Urone, P. P., Dirks, K., & Sharma, M. e. (2022). 12.4: Viscosity and Laminar Flow; Poiseuille's Law . In *College Physics 1e.* OpenStax. Retrieved August 23, 2025, from https://phys.libretexts.org/Bookshelves/College_Physics/College_Physics_1e_(OpenStax)/12%3A_Fluid_Dynamics_and_Its_Biological_and_Medical_Applications/12.04%3A_Viscosity_and_Laminar_Flow_Poiseuilles_Law

Hosseini, E. S., & Chakraborty, M. e. (2022, May 15). Porous Elastomer Based Wide Range Flexible Pressure Sensor for Autonomous Underwater Vehicles. *IEEE Sensors Journal, 22*(10), 9914-9921. doi:https://doi.org/10.1109/JSEN.2022.3165560

Hwang, T.-H., Cui, W.-H., Yang, I.-S., & Kwon, O.-K. (2010, July 15). A highly area-efficient controller for capacitive touch screen panel systems. *IEEE Transactions on Consumer Electronics, 56*(2), 1115-1122. doi:https://doi.org/10.1109/TCE.2010.5506047

Intersection, A. S. (2018). *Skorkovska, Vera; Kolingerova, Ivana; Benes, Bedrich.* Retrieved August 23, 2025, from SciTePress: https://www.scitepress.org/papers/2018/65384/65384.pdf

Ivrii, V. (2022). Partial Differential Equations. *Lecture*. (D. o. Mathematics, Ed.) Toronto: University of Toronto. Retrieved August 23, 2025, from https://www.math.toronto.edu/ivrii/PDE-textbook/PDE-textbook.pdf

Jegadeesan, R., Agarwal, K., Guo, Y.-X., Yen, S.-C., & Thakor, N. V. (2016, October 21). Wireless Power Delivery to Flexible Subcutaneous Implants Using Capacitive Coupling. *IEEE Transactions on Microwave Theory and Techniques, 65*(1), 280-292. doi:https://doi.org/10.1109/TMTT.2016.2615623

Kabakci, A. D., Büyükmumcu, M., Cicekcibasi, A. E., & al., M. T. (2017, March). An Osteometric Study on Humerus. *International Journal of Morphology, 35*(1), 219-226. doi:http://dx.doi.org/10.4067/S0717-95022017000100036

Kapoor, A., McKnight, M., & Chatterjee, K. e. (2016). Soft, flexible 3D printed fibers for capacitive tactile sensing. *IEEE Sensors* (pp. 1-3). Orlando: IEEE. doi:https://doi.org/10.1109/ICSENS.2016.7808918

Liburdy, J. (n.d.). 9: Boundary Layer Flows . In *Intermediate Fluid Mechanics* (Vol. 1). Oregon State University. Retrieved August 23, 2025, from https://eng.libretexts.org/Bookshelves/Civil_Engineering/Intermediate_Fluid_Mechanics_(Liburdy)/09%3A_Boundary_Layer_Flows

Lindsey, D., McKee, E., Hull, M., & Howell, S. (1998, May). A new technique for transmission of signals from implantable transducers. *IEEE Transactions on Biomedical Engineering, 45*(5), 614-619. doi:https://doi.org/10.1109/10.668752

Ling, S. J., Moebs, W., & Sanny, J. e. (2016). 8.2: Capacitors and Capacitance. In *University Physics II - Thermodynamics, Electricity, and Magnetism.* OpenStax. Retrieved August 22, 2025, from

https://phys.libretexts.org/Bookshelves/University_Physics/University_Physics_(OpenStax)/University_Physics_II_-_Thermodynamics_Electricity_and_Magnetism_(OpenStax)/08%3A_Capacitance/8.02%3A_Capacitors_and_Capacitance

Liou, W., Yang, Y., & Sabesan, V. J. (2016, December 27). Effect of lateralized design on muscle and joint reaction forces for reverse shoulder arthroplasty. *Journal of Shoulder and Elbow Surgery, 26*(4), 564-572. doi:https://doi.org/10.1016/j.jse.2016.09.045

Liu, X., & Stachel, J. R. (2013). The UHF Gen 2 RFID System for transcutaenous operation for orthopedic implants. *IEEE International Instrumentation and Measurement Technology Conference (I2MTC)*, (pp. 1620-1623). Minneapolis. doi:https://doi.org/10.1109/I2MTC.2013.6555688

Liu, X., Ogirala, A., Berger, L., & Mickle, M. (2011). Design and implementation of a volume conduction based RFID system for smart implants. *Annual International Conference of the IEEE Engineering in Medicine and Biology Society*, (pp. 2893-2896). Boston. doi:https://doi.org/10.1109/IEMBS.2011.6090797

Lodato, R., & Marrocco, G. (2015, November 25). Close Integration of a UHF-RFID Transponder Into a Limb Prosthesis for Tracking and Sensing. *IEEE Sensors Journal, 16*(6), 1806 - 1813. doi:https://doi.org/10.1109/JSEN.2015.2503887

Margalit, D., & Rabinoff, J. (2019). Matrix Transformations. In *Interactive Linear Algebra* (pp. 114-115). Georgia Institute of Technology. Retrieved from https://textbooks.math.gatech.edu/ila/ila.pdf

Margalit, D., & Rabinoff, J. (2019). Row Reduction. In *Interactive Linear Algebra (Margalit and Rabinoff)* (pp. 11-12). Georgia Institute of Technology. Retrieved from https://textbooks.math.gatech.edu/ila/ila.pdf

Merli, F. (2011). *Implantable Antennas for Biomedical Applications.* EPFL, Laboratory of Electromagnetics and Antennas. Lausanne: EPFL. doi:https://doi.org/10.5075/epfl-thesis-5110

Moebs, W., & Ling, S. J. (2016). 12.4: Stress, Strain, and Elastic Modulus (Part 1). In *University Physics I - Mechanics, Sound, Oscillations, and Waves (OpenStax).* OpenStax. Retrieved August 22, 2025, from https://phys.libretexts.org/Bookshelves/University_Physics/University_Physics_(OpenStax)/Book%3A_University_Physics_I_-_Mechanics_Sound_Oscillations_and_Waves_(OpenStax)/12%3A_Static_Equilibrium_and_Elasticity/12.04%3A_Stress_Strain_and_Elastic_Modulus_(P

Moebs, W., & Ling, S. J. (2016). Torque. In *University Physics I - Mechanics, Sound, Oscillations, and Waves (OpenStax).* OpenStax. Retrieved from https://phys.libretexts.org/Bookshelves/University_Physics/University_Physics_(OpenStax)/Book%3A_University_Physics_I_-

_Mechanics_Sound_Oscillations_and_Waves_(OpenStax)/10%3A_Fixed-Axis_Rotation__Introduction/10.07%3A_Torque

Moebs, W., Ling, S. J., & Sanny, J. (2016). 10.6: RC Circuits. In *University Physics II - Thermodynamics, Electricity, and Magnetism.* OpenStax. Retrieved from https://phys.libretexts.org/Bookshelves/University_Physics/University_Physics_(OpenStax)/University_Physics_II_-_Thermodynamics_Electricity_and_Magnetism_(OpenStax)/10%3A_Direct-Current_Circuits/10.06%3A_RC_Circuits

Moebs, W., Ling, S. J., & Sanny, J. e. (2016). 12.6: Elasticity and Plasticity. In *University Physics I - Mechanics, Sound, Oscillations, and Waves (OpenStax).* OpenStax. Retrieved August 22, 2025, from https://phys.libretexts.org/Bookshelves/University_Physics/University_Physics_(OpenStax)/Book%3A_University_Physics_I_-_Mechanics_Sound_Oscillations_and_Waves_(OpenStax)/12%3A_Static_Equilibrium_and_Elasticity/12.06%3A_Elasticity_and_Plasticity

Moore, K., & Dalley, L. e. (2017, May 25). *Anatomy.co.uk*. Retrieved August 8, 2025, from https://anatomy.co.uk/ball-and-socket-joint

Mouser Electronics. (2025). *Featured Products by Amphenol FCI*. (Mouser Electronics) Retrieved August 24, 2025, from https://www.mouser.co.uk/manufacturer/fci/

Naira, N. M., Shakhtivel, D., & Dahiya, R. (2023). Transparent Flexible Capacitive Pressure Sensor Array. *IEEE Applied Sensing Conference (APSCON)* (pp. 1-3). Bengaluru: IEEE. doi:https://doi.org/10.1109/APSCON56343.2023.10101243

Nam, H., Seol, H.-K., Lee, J., Cho, H., & Jung, S. W. (2021, July 13). Review of Capacitive Touchscreen Technologies: Overview, Research Trends, and Machine Learning Approaches. *Sensors, 21*(14), 4776. doi:https://doi.org/10.3390/s21144776

Pandya, J. J., & Low, A. K. (2017, November 14). Shoulder replacement for osteoarthritis: A review of surgical management. (76, Ed.) *Maturitas, 108*, 71. doi:https://doi.org/10.1016/j.maturitas.2017.11.013

Park, J.-E., Lim, D.-H., & Jeong, D.-K. (2014, August 1). A Reconfigurable 40-to-67 dB SNR, 50-to-6400 Hz Frame-Rate, Column-Parallel Readout IC for Capacitive Touch-Screen Panels. *IEEE Journal of Solid-State Circuits, 49*(10), 2305-2318. doi:https://doi.org/10.1109/JSSC.2014.2336800

Pelgrom, M. J. (2022). *Analog-to-Digital Conversion.* Springer. Retrieved August 23, 2025, from https://link.springer.com/book/10.1007/978-3-030-90808-9

Peng, Q., Xianmin, Q., & Yulong, B. e. (2021). Design and Experimental Research on Flexible Capacitive Tactile Sensor Based on Micro-Electro-Mechanical-System. *International Conference on Intelligent Computing, Automation and Systems (ICICAS)* (pp. 80-83). Chongqing: IEEE. doi:https://doi.org/10.1109/ICICAS53977.2021.00023

Pinter, C., Lasso, A., & Fichtinger, G. (2019). Polymorph segmentation representation for medical image computing. *Computer Methods and Programs in Biomedicine, 171*, 19-26. doi:https://doi.org/10.1016/j.cmpb.2019.02.011

Ponce Capunzano, J. C. (n.d.). 1.3: Geometric Interpretation of the Arithmetic Operations. In *Complex Analysis - A Visual and Interactive Introduction.* University of Queensland. Retrieved August 23, 2025, from https://math.libretexts.org/Bookshelves/Analysis/Complex_Analysis_-_A_Visual_and_Interactive_Introduction_(Ponce_Campuzano)/01%3A_Chapter_1/1.03%3A_Geometric_Interpretation_of_the_Arithmetic_Operations

Ponce, B. A., Oladeji, L. O., Rogers, M. E., & Menendez, M. E. (2015, March). Comparative analysis of anatomic and reverse total shoulder arthroplasty: in-hospital outcomes and costs. *Journal of Shoulder and Elbow Surgery, 24*(3), 460-467. doi:https://doi.org/10.1016/j.jse.2014.08.016

Raja, M. M., & Barron, A. R. (n.d.). 2.9: Electrical Permittivity Characterization of Aqueous Solutions . In *Physical Methods in Chemistry and Nano Science.* OpenStax CNX. Retrieved August 23, 2025, from https://chem.libretexts.org/Bookshelves/Analytical_Chemistry/Physical_Methods_in_Chemistry_and_Nano_Science_(Barron)/02%3A_Physical_and_Thermal_Analysis/2.09%3A_Electrical_Permittivity_Characterization_of_Aqueous_Solutions

Raymond, D. J. (n.d.). 17.1: The Capacitor and Ampère's Law. In *Radically Modern Introductory Physics* (Vol. 2). New Mexico Tech Press. Retrieved from https://phys.libretexts.org/Bookshelves/University_Physics/Radically_Modern_Introductory_Physics_Text_II_(Raymond)/17%3A_Capacitors_Inductors_and_Resistors/17.01%3A_The_Capacitor_and_Amperes_Law

Roche, C. P. (2022, January 19). Reverse Shoulder Arthroplasty Biomechanics. *Journal of Functional Morphology and Kinesiology, 7*(1). doi:https://doi.org/10.3390/jfmk7010013

Roche, C., & Flurin, H.-P. e. (2009, February 27). An evaluation of the relationships between reverse shoulder design parameters and range of motion, impingement, and stability. *Journal of Shoulder and Elbow Surgery, 18*(5), 734-741. doi:https://doi.org/10.1016/j.jse.2008.12.008

Rohm, K., & Zloczower, I.-M. (2023). A micromechanical approach to TPU mechanical properties: Framework and experimental validation. *Mechanics of Materials, 180*.

Roylance, D. (1999). 4.1: Shear and Bending Moment Diagrams . In *Mechanics of Materials.* MIT OpenCourseWare. Retrieved August 23, 2025, from https://ocw.mit.edu/courses/3-11-mechanics-of-materials-fall-1999/pages/syllabus/

Sadeque, R. K., Pavuluri, S. K., Cummins, G., & Desmulliez, M. P. (2020, June 19). Wireless Power Transfer Techniques for Implantable Medical Devices: A Review. *Sensors, 20*(12), 3487. doi:https://doi.org/10.3390/s20123487

Saini, M. K. (2022, December 15). *Charging of a Capacitor – Formula, Graph, and Example*. Retrieved August 22, 2025, from TutorialsPoint: https://www.tutorialspoint.com/charging-of-a-capacitor-formula-graph-and-example

SamacSys. (2020). *Component Search Engine*. (SamacSys) Retrieved August 24, 2025, from https://componentsearchengine.com/

Sanchez-Sotelo, J. (2011, March 16). Total Shoulder Arthroplasty. *The Open Orthopedics Journal*(5), 106-114. doi:https://doi.org/10.2174/1874325001105010106

Sanchhaya Education Private Limited. (2024, July 24). *Analog to Digital Conversion*. (GeeksforGeeks) Retrieved August 23, 2025, from https://www.geeksforgeeks.org/digital-logic/analog-to-digital-conversion/

Sanchhaya Education Private Limited. (2025, July 23). *Multiplexers in Digital Logic*. (GeeksforGeeks) Retrieved August 23, 2025, from https://www.geeksforgeeks.org/digital-logic/multiplexers-in-digital-logic/

Sanny, J., Ling, S. J., & Moebs, W. e. (2016). 16.2: Maxwell's Equations and Electromagnetic Waves . In *University Physics* (Vol. 2). OpenStax. Retrieved August 23, 2025, from https://phys.libretexts.org/Bookshelves/University_Physics/University_Physics_(OpenStax)/University_Physics_II_-_Thermodynamics_Electricity_and_Magnetism_(OpenStax)/16%3A_Electromagnetic_Waves/16.02%3A_Maxwells_Equations_and_Electromagnetic_Waves

Sara Rachel Arussy Ruth, V. R.-g. (2020, October 17). Flexible Fringe Effect Capacitive Sensors with Simultaneous High-Performance Contact and Non-Contact Sensing Capabilities. *Small Structures, 2*(2). doi:https://doi.org/10.1002/sstr.202000079

Seiko Epson Corporation. (2025). *kHz RANGE CRYSTAL UNIT MC-306*. (Seiko Epson Corporation) Retrieved August 28, 2025, from https://download.epsondevice.com/td/pdf/brief/MC-306_en.pdf

Shadid, R., & Noghanian, R. (2018, April 12). A Literature Survey on Wireless Power Transfer for Biomedical Devices. (G. Monti, Ed.) *International Journal of Antennas and Propagation, 2018*(1), 2-8. doi:https://doi.org/10.1155/2018/4382841

Shah, S. S., & Gaal, B. T. (2020, September 7). The modern reverse shoulder arthroplasty and an updated systematic review for each complication: part I. *Journal of Shoulder and Elbow Surgery International, 4*(4), 929-943. doi:https://doi.org/10.1016/j.jseint.2020.07.017

Shah, S. S., & Gaal, B. T. (2021, January 28). The modern reverse shoulder arthroplasty and an updated systematic review for each complication: part II. *Journal of Shoulder and Elbow Surgery International, 5*(1), 121-137. doi:https://doi.org/10.1016/j.jseint.2020.07.018

Sharma, A., & Kampianakis, E. R. (2016). A Dual-Band HF and UHF Antenna System for Implanted Neural Recording and Stimulation Devices. *IEEE Antennas and Wireless Propagation Letters, 16*, 493-496.

Storey, N. (2017). 12.2.7. Sensitivity. In *Electronics: A Systems Approach* (6 ed., pp. 209-212). Pearson. Retrieved August 23, 2025

Street, A., & Sustich, R. e. (2014). Advanced Nanosensors for Environmental Monitoring. In O. A. Sadik, *Nanotechnology Applications for Clean Water* (pp. 21-45). doi:https://doi.org/10.1016/B978-1-4557-3116-9.00002-0

Sun, M. (1997, December 31). An efficient algorithm for computing multishell spherical volume conductor models in EEG dipole source localization. *IEEE Transactions on Biomedical Engineering , 44*(12), 1243-1252. doi:https://doi.org/10.1109/10.649996

Syed, W. U., & Elfadel, I. (. (2024). Review of Euler–Bernoulli Rectangular Beam Theory. In W. U. Syed, & I. (. Elfadel, *Tapered Beams in MEMS* (pp. 17-31). Springer. doi:https://doi.org/10.1007/978-3-031-66391-8_2

Tang, Z., Sclabassi, R. J., Sun, C., Hackworth, S. A., Zhao, J., & Cui, X. T. (2006). Transcutaneous Battery Recharging By Volume Conduction and its Circuit Modeling. *International Conference of the IEEE Engineering in Medicine and Biology Society.* New York.

Terman, C. (2017). Computation Structures. *Combinational Logic*. MIT OpenCourseWare. Retrieved August 23, 2025, from https://ocw.mit.edu/courses/6-004-computation-structures-spring-2017/pages/c4/c4s1/#5

Texas Instruments. (2018). *TMUX1208 5-V Bidirectional 8:1, 1-Channel Multiplexer TMUX1209 5-V Bidirectional 4:1, 2-Channel Multiplexer datasheet (Rev. C)*. (Texas Instruments) Retrieved August 28, 2025, from https://www.ti.com/lit/ds/symlink/tmux1208.pdf?ts=1756404701412

Texas Instruments. (2021). *MSP430FR267x Capacitive Touch Sensing Mixed-Signal Microcontrollers datasheet (Rev. D)*. (Texas Instruments) Retrieved August 28, 2025, from https://www.ti.com/lit/ds/symlink/msp430fr2676.pdf?ts=1756391932800&ref_url=https%253A%252F%252Fwww.ti.com%252Fproduct%252FMSP430FR2676%253Futm_source%253Dgoogle%2526utm_medium%253Dcpc%2526utm_campaign%253Depd-null-null-GPN_EN-cpc-pf-google-ww_en_cons%252

Texas Instruments. (2025). *MSP430FR267x Capacitive Touch Sensing Mixed-Signal Microcontrollers*. (Texas Instruments) Retrieved August 28, 2025, from https://www.ti.com/document-viewer/msp430fr2676/datasheet

Ultimaker. (2022). Ultimaker TPU 95A - Technical data sheet. Ultimaker.

Urone, P. P., Hinrichs, R., Adams, M., Christensen, E., & Ingram, D. e. (2022). 23.2: Reactance, Inductive and Capacitive. In P. P. Urone, R. Hinrichs, M. Adams, E. Christensen, & D. e. Ingram, *College Physics.* OpenStax. Retrieved August 23, 2025, from https://openstax.org/books/college-physics/pages/preface

VJ Tech. (2019, November 28). (VJ Tech) Retrieved August 23, 2025, from https://www.vjtech.co.uk/introduction-to-cyclic-dynamic-triaxial-testing/

Voltera. (2024). *Voltera V-One User Manual*. (Voltera) Retrieved September 2, 2025, from https://docs.voltera.io/docs/v-one/downloads/user-manuals

Voltera. (n.d.). *Technical Specification*. (Voltera) Retrieved August 23, 2025, from Voltera Website: https://www.voltera.io/technical-specifications

Walker M, B. J. (2011, April 12). How Reverse Shoulder Arthroplasty Works. *Clinical Orthopedics and Related Research*(469), 2440-2451. doi:https://doi.org/10.1007/s11999-011-1892-0

Wang, X., Zhong, Y., Sun, Y., & Li, X. (2014). A flexible capacitive tactile sensing array for pressure measurement. *IEEE International Conference on Robotics and Biomimetics (ROBIO 2014)* (pp. 2344-2349). Bali: IEEE. doi:https://doi.org/10.1109/ROBIO.2014.7090688

Wang, X., Zhong, Y., Sun, Y., & Li, X. (2014). A flexible capacitive tactile sensing array for pressure measurement. *IEEE International Conference on Robotics and Biomimetics (ROBIO 2014)*, (pp. 2344-2349). Bali. doi:https://doi.org/10.1109/ROBIO.2014.7090688

Wang, Y., Pang, Q., & Liu, Y. (2024, October 30). Comparative Study of Algorithms for the Conversion From Surface Mesh Models to Volume Mesh Models. *Advances in Civil Engineering*. doi:https://doi.org/10.1155/2024/4669855

Weaver, J. S., Omar, I. M., & Chadwick, N. S. (2023, April 18). Update on Shoulder Arthroplasties with Emphasis on Imaging. *Journal of Clinical Medicine, 8*(12), 2946. doi:https://doi.org/10.3390/jcm12082946

Willem, J. V. (2021). History of shoulder arthroplasty. *Journal of Arthroscopy and Joint Surgery, 8*(1), 2-6. doi:https://doi.org/10.1016/j.jajs.2020.12.001

Zhabinskaya, D. (n.d.). 5.10: Exponential Charge Flow. In *UCD: Physics 7B - General Physics.* UCD: Physics 7B - General Physics. Retrieved August 22, 2025, from https://phys.libretexts.org/Courses/University_of_California_Davis/UCD%3A_Physics_7B_-_General_Physics/5%3A_Flow_Transport_and_Exponential_-_working_copy/5.10%3A_Exponential_Charge_Flow

Zhang, P. (2010). CHAPTER 14 - Data transmission interfaces. In *Advanced Industrial Control Technology* (pp. 557-598). Elsevier. doi:https://doi.org/10.1016/C2009-0-20337-0

Zhao, S., & Ran, W. e. (2020, June 22). 3D Dielectric Layer Enabled Highly Sensitive Capacitive Pressure Sensors for Wearable Electronics. *ACS Applied Materials & Interfaces, 12*(28), 32023–32030. doi:https://doi.org/10.1021/acsami.0c09893

Zhou, Y., Dazhuan, X., Tu, W., & Shi, C. (2020, May 8). Spatial information and angular resolution of sensor array. *Signal Processing, 174*. doi:https://doi.org/10.1016/j.sigpro.2020.107635